MBE Growth and Characterization of Germanium Nanowires

Von der
Fakultät für Mathematik, Naturwissenschaften und Informatik
der Brandenburgischen Technischen Universität Cottbus

zur Erlangung des akademischen Grades

Doktor der Naturwissenschaften
(Dr. rer. nat.)

genehmigte Dissertation

vorgelegt von

Diplom-Physiker

Jan Schmidtbauer

geboren am 07. Oktober 1983 in Zittau

Gutachter: Prof. Dr. Jürgen Reif

Gutachter: Prof. Dr. Hans Lüth

Gutachter: Prof. Dr. Knut Deppert

Tag der mündlichen Prüfung:19. Juni 2013

Ph.D. Thesis

MBE Growth and Characterization of Germanium Nanowires

Jan Schmidtbauer

August 16, 2013

Brandenburg
University of Technology
Cottbus

Faculty of Mathematics, Natural Sciences
and Computer Science

Forschungsverbund
Berlin e.V.

Leibniz Institute
for
Crystal Growth
(IKZ)

Member of the
Leibniz Association

“I do not know what I may appear to the world, but to myself I seem to have been only like a boy playing on the seashore, and diverting myself in now and then finding a smoother pebble or a prettier shell than ordinary, whilst the great ocean of truth lay all undiscovered before me.”

Sir Isaac Newton

Abstract

Semiconductor nanowires, also called nanorods or nanowhiskers, are of particular interest for various applications in nanotechnology. Especially, germanium as a CMOS compatible material with its good electronic properties has gained renewed interest in recent years due to the availability of modern gate dielectrics.

The present work deals with the vapor-liquid-solid growth of germanium nanowires and their characterization. The Growth has been carried out by means of molecular beam epitaxy using differently oriented germanium and silicon substrates whereas gold has been used to create metal catalyst droplets with radii of typically 100 nm and below.

All stages from the substrate preparation to the final growth have been investigated in the frame of this work to find significant control parameters that influence the growth result. The droplet formation by means of gold evaporation onto the heated substrates has been investigated extensively on different substrates and for different surface preparations to identify parameters that are crucial for the resulting size distribution. Thereby sticking effects of the droplet circumference turned out to influence the radius distribution significantly.

Germanium nanowires have been observed to grow preferentially along the $\langle 011\rangle$ crystallographic directions on all utilized substrate orientations leading to defined possible inclinations of the wires with respect to the substrate normal. In contrast to the faceting known from silicon wires, the sidewalls mainly exhibit four flat $\{111\}$ facets whereas the tip is roof shaped consisting of another two $\{111\}$ facets. Different models which describe the inclined growth are presented and discussed. Furthermore, the material transport during the growth has been investigated. The nanowire length was found to be up to eight times larger than the nominal layer thickness according to the total amount of deposited germanium which is explained by surface diffusion towards the nanowires. The diffusion dominated growth regime was confirmed by length-radius-plot showing a decrease of the nanowire length at increasing radii. A temperature dependent diffusion model has been utilized to describe the observed nanowire length as a function of the substrate temperature.

Beside conventional nanowires, so-called in-plane nanowires which grow along the substrate surface have been studied. Like their vertically growing counterparts, they also tend to grow along $\langle 011\rangle$ in-plane directions which is particularly distinct on Ge(110) substrates. However, the fraction of nanowires which are aligned along $\langle 011\rangle$ is influenced

by substrate imperfections which was intentionally affected by means of wet-chemical substrate preparation.

In addition to the nanowire growth, techniques for selective catalyst removal as well as for nanowire embedding in an insulating, transparent matrix have been established which can be important prerequisites for further nanowire processing in terms of electric or optoelectronic applications.

Kurzfassung

Halbleitende Nanodrähte, auch Nanosäulen oder Nanowhisker genannt, sind wegen vielfältiger Anwendungsmöglichkeiten auf dem Gebiet der Nanotechnologie von hohem Interesse. Das gilt insbesondere für Germanium mit seinen guten elektronischen Eigenschaften, welches in den letzten Jahren eine Renaissance erlebt hat. Ein wesentlicher Grund hierfür ist seine Verwendbarkeit in der CMOS Technologie durch die Entwicklung moderner Gateisolationsschichten.

Die vorliegende Arbeit behandelt das Wachstum von Germanium Nanodrähten nach dem vapor-liquid-solid-Mechanismus (gasförmig-flüssig-fest) und deren Charakterisierung. Als metallisches Lösungsmittel zur Erzeugung von Tröpfchen mit Radien im Bereich von 100 nm und kleiner wurde Gold verwendet.

Von der Substratpreparation bis zum Wachstum wurden alle Phasen der Herstellung von Nanodrähten untersucht, um die wesentlichen Parameter zu finden, welche wichtige Kenngrößen wie die Wachstumsrate oder den Radius der Nanostrukturen beeinflussen.

Ein Schwerpunkt der Untersuchung ist die Bildung von Tröpfchen und deren Größenverteilung als Funktion der Temperatur auf verschiedenen Substraten sowie in Abhängigkeit von unterschiedlichen Oberflächenvorbehandlungen.

Das Wachstum der Nanosäulen erfolgt auf allen verwendeten Substratorientierungen bevorzugt in den $\langle 011 \rangle$-Richtungen, was zu bestimmten Neigungswinkeln der Nanodrähte bezüglich der Substratnormalen führt. Anders als es von Silizium-Nanodrähten bekannt ist, weisen in $\langle 011 \rangle$-Richtung gewachsene Germaniumdrähte vier $\{111\}$-Seitenfacetten auf und eine dachförmige Spitze, die aus zwei weiteren $\{111\}$-Facetten besteht. Das bevorzugte Wachstum in $\langle 011 \rangle$-Richtungen wird anhand verschiedener Modelle diskutiert. Darüber hinaus wurde die Wachstumsrate der Nanowhisker unter Berücksichtigung des Stofftransportes untersucht. Es zeigt sich, dass die Oberflächendiffusion der Germaniumatome den entscheidenden Einfluss auf die Wachstumsrate der Nanodrähte hat. In einem entsprechenden Längen-Radius-Diagram ist ein diffusionslimitiertes Wachstumsregime ersichtlich.

Die untersuchten Nanodrähte waren bis zu acht mal länger als die nominelle Schichtdicke, welche der Menge an deponiertem Germanium entspricht, was durch den diffusiven Stofftransport zum Wachstumsort an der Spitze der Nanodrähte erklärt werden kann.

Die Wachstumsrate als Funktion der Temperatur konnte mit Hilfe der Temperaturabhängigkeit der Diffusionslänge im Rahmen eines einfachen Diffusionsmodels berechnet werden.

Neben konventionellen Nanowhiskern wurden so genannte In-plane-Nanodrähte untersucht, welche innerhalb der Substratebene wachsen. Ähnlich wie vertikale Nanodrähte weisen diese bevorzugte, azimutale $\langle 011\rangle$-Richtungen, was auf Ge(011)-Substraten besonders ausgeprägt ist. Der Anteil an In-pane-Nanodrähten, welche entlang der bevorzugten Richtungen wachsen, ist abhängig von Defekten in der Substratoberfläche, wie zum Beispiel der Rauigkeit und konnte gezielt durch nasschemische Vorbehandlung beeinflusst werden. Diese Befunde können bei gerichtetem Wachstum von Nanodrähten entlang von Oberflächen von Bedeutung sein, was in der Literatur auch als Guided Growth bezeichnet wird.

Zusätzlich zu Wachstumsuntersuchungen wurden Methoden getestet, um Goldtröpfchen nasschemisch bei möglichst geringem Ätzangriff von Germanium-Nanostrukturen zu entfernen. Darüber hinaus wurden Nanostrukturen mittels Spin-Coating in eine elektrisch isolierende und transparente Matrix eingebettet. Für zukünftige Anwendungen können beide Arbeitsschritte eine wichtige Rolle spielen.

Contents

1 Introduction

1.1 Nanoscience and Nanotechnology

It is known for a long time that sufficient reduction of the number of atoms in a structure can change its properties dramatically. The enormous application potential coming along with down scaling has already been pointed out by Richard Feynman who is generally regarded as one of the pioneers of nanotechnology and who gave his famous presentation in 1959 with the well known title "There is plenty of room at the bottom" [1].

Feynman's visions of "How do we write small" have come true in the last decades and have even been exceeded. As such, writing the entire 24 volumes of the *Encyclopaedia Brittanica* on the head of a pin can be achieved easily today. It covers about 10^9 bits of information which can nowadays be stored on 1/100 of the surface area of the head of a pin [2].

Size reduction, especially of crystalline material, will ultimately lead to new material properties due to the increasing influence of physical effects important to surfaces and atoms which are negligible in bulk. Size effects become important when at least one dimension is reduced to several tens of nanometers - the typical length scale of nano-sized material. This has instigated the rapidly growing field of nanotechnology and nanoscience regarding synthesis, manipulation, characterization and application of matter on the nanometer scale. Commonly, nanotechnology refers to structural dimension between 1 nm and 100 nm. The lower limit is generally given by the atomic diameter of a material whereas the upper limit is rather arbitrary according to dimensions at which size effects become apparent.

The unique properties of nanostructures can be roughly divided into two groups - quantum confinement effects and surface related effects. The latter arise due to the fact that atoms at surfaces experience different chemical environment than their counterparts in the bulk. In bulk material the fraction of surface atoms is negligible such that processes taking place at the surface do generally not influence the characteristic of the material as a whole. Typically, the surface-to-volume ratio of nanoscale structures is considerably higher, such that surface effects can not be ignored. Atoms at surfaces have a higher state of energy than in the bulk. Eventually, this can change atomic ordering at surfaces or even lead to different morphologies of crystalline material to accommodate the high fraction of surface atoms.

Quantum confinement effects arise if at least one dimension of the material is of the order of the wavelength of an electron in the solid. At such small dimensions the motion of electron is limited which leads to discretization of possible energy levels. The density of states of electrons is determined by the number of dimensions in which the electron is confined [3].

1.2 Nanowires

Filamentary growth of material is known for a long time but has generally been dismissed as parasitic growth which occurs at the walls of deposition chambers. Whisker growth, which was a common term for a long time, has this year its 55th anniversary as the first systematic growth study of whiskers, to the best of our knowledge, was presented in 1957 by Treuting and Arnold [4]. First silicon “whiskers” have been grown by Wagner and Ellis in 1964 which is at the same time the first report on filamentary growth of semiconductors. [5]. Over the years, other terms like “nanocolumn” or “nanorod” have been coined next to “nanowire” which eventually became the most common name in the course of the 1990s until today.

The enormous potential of one-dimensional nanostructures which exhibit quantum confinement in two dimensions has been pointed out by Sakaki at the beginning of the 1980s in his theoretical work concerning the suppression of scattering in semiconductor nanowires which leads to high mobility of electrons [6]. However, nanowires created from bulk material by top-down lithography and etching processes rather show the opposite behaviour caused by scattering at rough sidewalls which lowers mobility. Therefore, high predicted mobilities could not be achieved up to now.

It became clear that free standing, naturally grown nanowires would be able to overcome this obstacle as they typically exhibit smoother sidewalls which may reduce scattering and thus maintain the high mobility [7]. A bottom-up approach by growing nanowires on top of a substrate can therefore be advantageous. In order to gain highly anisotropic growth, typically small metal particles or droplets serve as catalyst which enables preferential growth of nanowires instead of layers. However, the growth of very thin nanowires which exhibit quantum confinement is a big challenge for material scientists.

For this reason, the application of alternative semiconductors, e.g. germanium or com-

properties	Si	Ge	GaAs	InP
band gap [eV]	1.12	0.66	1.42	1.34
intrinsic carrier concentration [cm^{-3}]	1.0×10^{10}	2.0×10^{13}	2.1×10^{6}	1.3×10^{7}
intrinsic resistivity [$\Omega\,\mathrm{cm}$]	3.2×10^{5}	46	3.3×10^{8}	8.6×10^{7}
electron mobility [$\mathrm{cm}^2\,\mathrm{V}^{-1}\,\mathrm{s}^{-1}$]	≤ 1400	≤ 3900	≤ 8500	≤ 5400
hole mobility [$\mathrm{cm}^2\,\mathrm{V}^{-1}\,\mathrm{s}^{-1}$]	≤ 450	≤ 1900	≤ 400	≤ 200

Table 1.1: Electronic properties of Si, Ge, GaAs and InP. Values taken from [8]

pound semiconductors, for nanowire growth is therefore of big interest as most of them exhibit larger Bohr exciton radii (silicon ca. 5 nm) and quantum confinement can therefore be achieved at larger wire diameters. Especially, germanium is an appropriate candidate with lower effective mass of charge carriers and shows therefore quantum confinement already below a dimension of 18 nm (Bohr exciton radius of germanium).

The research on nanowires can generally be categorized by either the used material system or by the respective growth technique. In terms of growth techniques, a variety of methods is available, for example chemical vapor deposition (CVD), laser ablation or even solution growth. Molecular beam epitaxy (MBE), which is within the context of this thesis, offers the advatage of using individual elemental sources in an ultrahigh vacuum (UHV) avoiding contaminations with species from precursors or the ambient.

1.3 Potential Applications

Due to the fact that germanium is rarely available and does not form a sufficiently stable oxide it has not been used for semiconductor volume production. Although, germanium has gained renewed interest in recent years due to its high charge carrier concentration and mobility compared to silicon (see table 1.1) and due to advances in nanotechnology which can reduce material consumption significantly.

Next to their great importance in terms of electronic properties of one-dimensional systems, nanowires may be suitable for various potential applications. However, it is not quite likely that nanowires play a noteworthy role in the over-all down-scaling of CMOS technology. The current planar production technology is well established while obviously the end of downsizing of the smallest structures has not yet been driven to the very limits as 28 nm system-on-a-chip production is commonly implemented by many manufacturers while Intel started 22 nm volume production of processors at the end of 2011 [9]. Meanwhile, the next step in size reduction towards 14 nm channel length are already planned.

Nanowires will probably make use of their potential in different fields in which their large surface-to-volume ratio is significant for improvement of device performance like in sensor applications. As such, germanium nanowires are appropriate candidates for optoelectronic devices such as photo detectors due to good absorption of near infrared wavelength. In fact, the band gap of germanium matches well the wavelength of telecommunication infrastructure at 1.55 µm which is widely used because of very low optical attenuation in optical fibers. A first prove of principle showing improved response time has already been given by Yan et al. [10].

Furthermore, nanowires are promising structures for future thermoelectric devices. The thermoelectric performance of a material or device is described by the figure of merit ZT which is given by

$$ZT = \frac{\sigma S^2}{\kappa} T \tag{1.1}$$

where σ is the electrical conductivity, κ is the thermal conductivity, S is the Seebeck coefficient and T the temperature. ZT has typical values around 1 for available thermoelectric devices and can obviously be increased by increasing σ. An the other hand, according to the Wiedemann-Franz law, $\sigma T/\kappa$ is approximately constant which generally makes it complicated to increase ZT. It has been shown that Si/Ge/Si superlattices can overcome this limitation [11]. Very thin germanium tunneling barriers serve as scatterers for phonons while electrons are able to pass these interlayers. Thus, electronic conductivity and thermal conductivity caused by phonons can be decoupled. A similar effect can be observed in nanowires where phonons are scattered at the sidewalls while good conducting properties of the wire can be maintained to a large extend [12].

A rather new field of application for silicon or germanium nanowires is their use for high performance anode materials in lithium ion batteries. Currently, anodes are typically made of graphite which merely provides a theoretical specific capacity of $372\,\mathrm{mA\,h\,g^{-1}}$. In contrast, silicon and germanium can have a specific capacity of $4200\,\mathrm{mA\,h\,g^{-1}}$ and $1600\,\mathrm{mA\,h\,g^{-1}}$ respectively. However, a drawback of bulk anodes is disintegration of the material upon charging and discharging due to a huge volume change of up to 400%. Nanowires are appropriate structures to overcome this obstacle. They can be thin enough to accommodate lithium and undergo a volume change without being destroyed but rather being elastically distorted. Thereby, the material becomes amorphous while the nanowire structure remains intact. Cycling of nanowire anodes has been demonstrated by Chan et al. [13]. In addition to an increase of the specific anode capacity, germanium provides a 400-fold higher diffusivity of lithium at room temperature than silicon which is particularly important for high charge and discharge rates [14, 15].

2 Theoretical Background

In this chapter a brief introduction to the theoretical fundamentals is given which comprises basic thermodynamics and phase diagrams of the growing species. In addition, nucleation theory is presented to understand general nucleation mechanisms that are of importance both for the droplet formation as well as for the nucleation of germanium at the liquid-solid interface. Furthermore, the material transport of the growing species is modeled in terms of surface diffusion which governs the growth rate and the maximum length of nanowires.

2.1 Vapor-liquid-solid (VLS) mechanism

The term VLS mechanism was first introduced by Wagner and Ellis in 1964 to explain the growth of silicon whiskers from the gas phase in the presence of liquid gold droplets on silicon substrates [5]. In their work $SiCl_4$ precursor gas decomposes catalytically at gold droplets in which the silicon atoms are dissolved. Finally, so-called microwhiskers grow with the droplet at the tip. Thereby, the term whisker is commonly used for thicker wires in the micrometer range while the term nanowire refers to wires with significantly smaller diameters in the range of 100 nm and below.

From that time on, many approaches have been undertaken in order to understand and describe the growth of crystalline wires by VLS growth. Different techniques like metal organic vapour phase epitaxy (MOVPE) and molecular beam epitaxy (MBE) have been applied for the growth of whiskers and nanowires from various materials such as silicon [16], gallium nitride [17] or indium arsenide [18] to name only a few. Within the scope of this thesis VLS growth of germanium nanowires was conducted by means of MBE using gold for the droplet formation and both silicon and germanium were applied as substrates.

In general the VLS mechanism can be divided into two phases (see fig. 2.1). In the first step gold is evaporated to form droplets on the substrate serving as metal solvent. As the substrate is heated to a temperature higher than the eutectic temperature of gold and the substrate material (for eutectic temperature see 2.3.2) the droplets remain liquid.

In the second step germanium is evaporated and dissolves inside the droplets. Thus, the latter become supersaturated and germanium starts to crystallize by heterogeneous nucleation at the interface between droplet and substrate. Finally, a crystalline nanowire is grown with the gold droplet sitting on the tip of the nanowire.

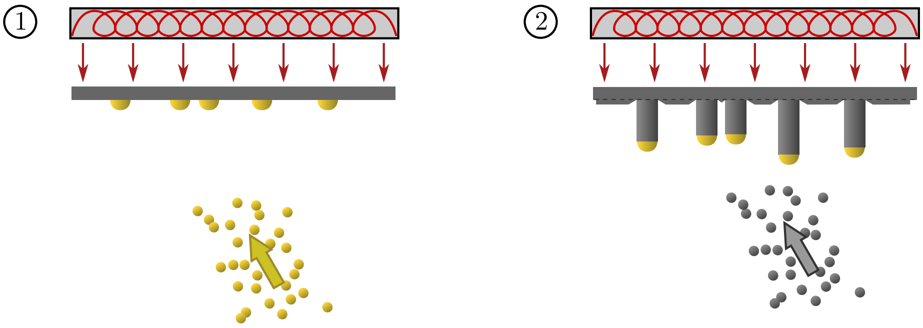

Figure 2.1: Illustration of the VLS growth of germanium nanowires. In step ① evaporated gold forms droplets at the substrate surface. In step ② the evaporated germanium supersaturated the droplets and crystallizes to form a nanowire.

2.2 Beyond Au assisted VLS growth

Since the VLS growth mechanism was published for the first time by Wagner and Ellis in 1964 [5] many different metals have been applied to form droplets in order to initiate nanowire growth. Especially for silicon, nanowire growth has been reported using aluminum [19], gold-aluminum alloy [20], copper [21] or silver [22] to name a few.

Next to the application of different metals for the formation of catalyst droplets, different growth regimes have been found, especially the vapor-solid-solid growth (VSS) has been identified for the growth of silicon and germanium nanowires at temperatures below the eutectic temperatures [23]. The solubility in the solid catalyst is significantly lower while diffusion coefficients of the growing species in the solid droplet are about four orders of magnitude lower compared to the liquid counterpart. Thus, the growth rate in VSS was found to be a factor of ten lower than in the VLS regime. On the other hand, the low solubility enables very abrupt axial compositional transitions between silicon and germanium as demonstrated by Wen et al. [20] which is not possible in VLS growth due to the reservoir effect when switching from one material to the other [24]. Material that is already dissolved in the droplet needs to be incorporated into the nanowire after switching to the new component which leads to a graded junction. The gradient of the junction is obviously a function of solubility of the first component in the catalyst.

Furthermore, various growth modes exist not only depending on whether the catalyst is liquid or solid but also so-called self-catalytic or even non-catalytic growth. Self-catalyzed nanowire growth occurs when compound semiconductors, especially III-V semiconductors like GaAs, InAs or InP are applied. The III-compound, if present in excess, can form droplets as well as it can be incorporated into the nanowire [25–27]. Recently, non-catalytic growth has been found in a regime where the V-component (arsenic, phosphorous, etc.) is in excess so that no metal droplet could be formed. Indeed, under those conditions nanowire growth was observed without any catalyst at the nanowire tip [28, 29]. This growth process is also called vapor-solid growth as the gaseous species are supposed be directly incorporated into the nanowire without the presence of a liquid phase. The microscopic nature of such anisotropic growth is still under investigation.

2.3 Thermodynamic fundamentals

Phase transitions are the basic processes in crystal growth as well as in nanowire growth since the growing species are transferred into a phase of higher chemical potential, e.g. gaseous phase, to crystallize them eventually in the solid state. Phase transitions as they occur during the nanowire growth are typically first-order phase transitions that involve a latent heat [30].

In this section a brief introduction into the thermodynamic basics is given in order to understand the underlying processes of the phase transitions that occur in VLS growth. Basically phase transitions as well as transport processes can be described by variations of chemical potential of the constituents in the different phases. It is defined as the change of Gibbs free energy with the number particles

$$\mu_i = \left(\frac{\partial G}{\partial N_i}\right)_{T,p,N_j=\mathrm{const}} \tag{2.1}$$

Here i denotes the ith component of the system. As a rule the chemical potential of the initial state has to be higher than in the final state as the system tends to be in the state of lowest energy. Thus, the driving force for a phase transition is the supersaturation, given as the difference of the chemical potential of a particle before and after the transition, e.g. the condensation of a vapor

$$\Delta\mu = \mu_g - \mu_{l,s} \tag{2.2}$$

In the case of condensing vapor the supersaturation can be expressed as follows in terms of the ratio between the actual pressure of the vapor p and the equilibrium pressure $p_e(T)$ when vapor and condensed phase are in equilibrium: $\Delta\mu = k_B T \ln\left(p/p_e(T)\right)$. Applying this formula for the case of a condensing molecular beam on a substrate, it goes over to

$$\Delta\mu = k_B T \ln\left(\frac{I}{I_e(T)}\right) \tag{2.3}$$

where $I_e(T) = p_e(T)/(2\pi m_0 k_B T)$ is the equilibrium impingement rate of molecules at the pressure $p_e(T)$ and I is the impingement rate of the deposited particles [31]. In analogy to the condensing vapor the supersaturation of dissolved material in a solvent (the solute), as it is the case in the VLS process where germanium is dissolved in a gold droplet, can be expressed in terms of the concentrations of the ideal solution

$$\Delta\mu = k_B T \ln\left(\frac{x}{x_e(T)}\right) \tag{2.4}$$

where x is the mole fraction of the dissolved material and x_e corresponds to the saturation concentration.

2.3.1 Chemical potential of molecular beams

The chemical potential of a molecular beam emerging from standard effusion cells can not be described as an ideal gas at source temperature since motion of the particles is not randomly distributed but along a given direction towards the sample. From the thermodynamic point of view this given direction corresponds to a higher degree of ordering which leads to a lower entropy of the molecular beam compared with an ideal gas of the same temperature.

To find an appropriate description a statistical approach is needed. The source of a molecular beam is material which is evaporated in the effusion cell forming a vapor directly above the source material. This vapor can be described as an ideal gas with a partition function $Z_{3\mathrm{D}}$ in a finite volume near the phase boundary. The molecular beam itself can be considered as an ideal gas of molecules moving in one dimension only on the one hand but consists of molecules which have the internal partition function of the three-dimensional ideal gas, since they originated from the latter, on the other hand. Partition functions can be understood as the sum of possible energy states of N particles (ensemble). Accordingly, a system which is described by a combination of different ensembles has a total amount of possible energy states which results from the combination of each energy state of the first ensemble with each energy state of the second one. Thus, the total partition function Z is given as the product of Z_{3D} with a one-dimensional gas moving along a given direction Z_{1D}.

In the following, the system is treated as a canonical ensemble in which particle number N, volume per particle V and temperature T are constant. This is true because in a finite volume the number of particles is constant at a constant flux while the temperature is given by the source temperature. Thereby, the N particles are of the same kind such that no index is used, e.g. for the $i-th$ constituent. The canonical partition functions of an ideal gas in one and three dimensions are given by [32]

$$Z_{\mathrm{3D}} = \frac{V^N}{\lambda_{th}^{3N} N!} \tag{2.5}$$

$$Z_{\mathrm{1D}} = \frac{l^N}{\lambda_{th}^{N} N!} \tag{2.6}$$

where $\lambda_{th} = h/\sqrt{2\pi m k_B T}$ is the so-called thermal wavelength. Here V is the volume per atom in 3D and l the mean distance between atoms in 1D along the axis of the beam. The Helmholtz free energy of the system is given by

$$\begin{aligned} F &= -k_B T \ln(Z) = -k_B T \left[\ln(Z_{\mathrm{1D}}) + \ln(Z_{\mathrm{3D}})\right] \\ &= -k_B T N \left[\ln\left(\frac{V}{\lambda_{th}^3 N}\right) + \ln\left(\frac{l}{\lambda_{th} N}\right) + 2\right] \end{aligned} \tag{2.7}$$

In equation (2.7) Stirling's approximation formula $\ln(N!) \approx N\ln(N) - N$ was applied. The chemical potential is given as the derivative of Helmholtz free energy with respect to N at constant temperature and volume V or length l respectively (constant particle number of other constituents is omitted here since all particles are of the same kind, w.l.o.g.).

$$\begin{aligned} \mu &= \left(\frac{\partial F}{\partial N}\right)_{V,l,T} \\ &= -k_B T \left[\ln\left(\frac{V}{\lambda_{th}^3 N}\right) + \ln\left(\frac{l}{\lambda_{th} N}\right)\right] \end{aligned} \tag{2.8}$$

The first summand in equation (2.8) can be identified with the chemical potential of an ideal gas whereas the second summand accounts for the chemical potential of a gas where motion occurs only in one dimension along a given direction. Thus, V can be rewritten by the equation of state $p_0 V = N k_B T$ with p_0 as the vapor pressure corresponding to the temperature T of the material inside the effusion cell (for details see sec 3.1.1).

The mean distance of the atoms in a molecular beam is basically determined by the flux density $W = \Phi/A = \bar{v}N/V$ where N/V is the particle density in the molecular beam, A is the cross section and $\bar{v}$ is the mean velocity of the particles. By rewriting V as Al we find $\Phi = \bar{v}N/l$. Substituting V and l in equation (2.8) leads the form

$$\mu = -k_B T \left[\ln\left(\frac{k_B T}{p_0 \lambda_{th}^3}\right) + \ln\left(\frac{\bar{v}}{\Phi \lambda_{th}}\right) \right] \tag{2.9}$$

In order to determine the mean speed of the particles one can assume a one-dimensional Maxwell-Boltzmann distribution which is given as follows [32, chap. 2]

$$f(v) = \left(\frac{m}{2\pi k_B T}\right)^{1/2} e^{-\frac{mv^2}{2k_B T}} \tag{2.10}$$

To find the mean velocity along a given direction, i.e. only positive velocities, one has so calculate

$$\bar{v} = \frac{\int_0^\infty v f(v)\, dv}{\int_0^\infty f(v)\, dv} = \left(\frac{k_B T}{2\pi m}\right)^{1/2} \tag{2.11}$$

With this relation between flux and mean velocity the chemical potential can be written in the following form

$$\mu = -k_B T \left[\ln\left(\frac{k_B T}{p_0 \lambda_{th}^3}\right) + \ln\left(\frac{k_B T}{\Phi \sqrt{h}}\right) \right] \tag{2.12}$$

Finally, the flux Φ can be expressed in terms of the pressure which corresponds to the collision rate at the substrate surface multiplied with the area of impingement $\Phi = p_0 A/\sqrt{2\pi m k_B T}$ [30, sec. 21.2]. The resulting term of the chemical potential is thus given by

$$\mu = -k_B T \left[\ln\left(\frac{k_B T}{p_0 \lambda_{th}^3}\right) + \ln\left(\frac{k_B T}{p_0 A \lambda_{th}}\right) \right] \tag{2.13}$$

Obviously, the resulting chemical potential of the molecular beam is higher than that of an ideal gas. This coincides with the expectation that the lower entropy in the beam leads to a high Gibbs free energy and thus to a higher chemical potential. In the frame of this model it is assumed that an ideal vapor forms above the molten material inside the effusion cell. This holds not true completely because the vapor is not in equilibrium since it is directly in contact with the vacuum. This controversy can be overcome by the use of Knudsen cells consisting of an almost closed volume with a small hole. In this way the vapor inside the volume can be described sufficiently as an ideal gas.

2.3.2 Au-Ge phase diagram

A phase diagram shows conditions, e.g. pressure and temperature, at which different phases are in stable equilibrium which means that atoms or molecules of each constituent have the same chemical potential. In other words no energy is gained by moving a particle from one phase to the other and thus two or more phases can coexist.

When more than one component is present the concentration becomes an important parameter. Especially in the case of binary alloys the temperature-concentration diagram gives important information about the existence of stable phases at certain compositions and temperatures. The conditions for phase equilibrium are marked by liquidus and solidus lines as the margins of liquid and solid phases respectively. The gold germanium phase diagram is a simple eutectic diagram with one eutectic at 361 °C with $Au_{0.72}Ge_{0.28}$ composition (see figure 2.2). The liquidus line connects the eutectic with the gold melting point on the left and with the germanium melting point on the right. In between, the eutectic line separates regions where solid and liquid phases are present (but not mixed - miscibility gaps: Au + AuGe(l), Ge + AuGe(l)) from regions where two solid phases are present (Au(s), Ge(s)). Thus, strictly speaking the eutectic line is no solidus line as it is often indicated in literature. Furthermore, the gold rich, solid Phase on the left and the solid germanium phase on the right are delimited by so called solvus lines at temperatures below the eutectic temperature.

2.3.3 Corrections for nanoscales

Common phase diagrams as they are described in the section above are bulk phase diagrams. This means no contribution of the surface to the total Gibbs free energy is considered. On the other hand, for small dimensions in the nanometer scale as we find them in the nanowire growth with droplet diameter below 100 nm surface effects may influence the phase diagram significantly. In this section, different thermodynamic effects are elucidated that are commonly under discussion in terms of corrections in the phase diagrams for nanometer scales.

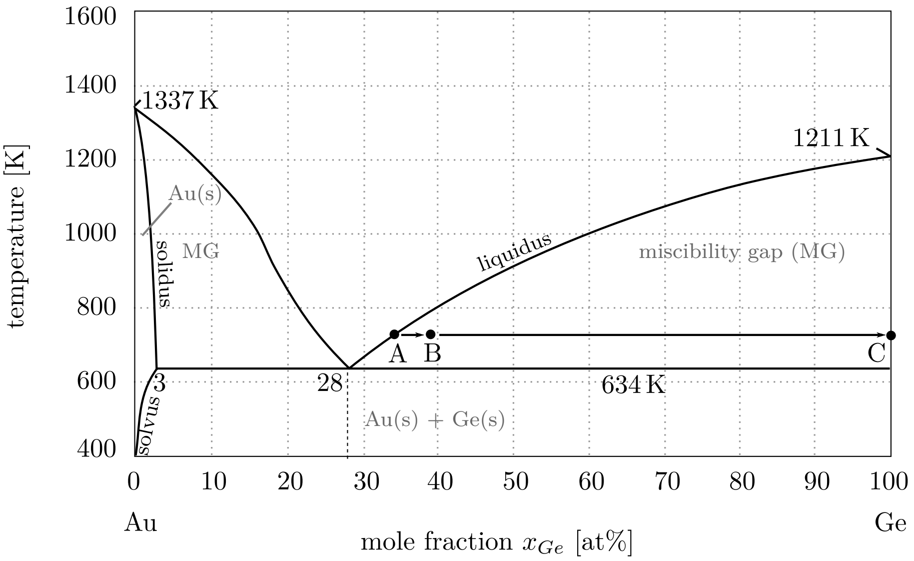

Figure 2.2: Binary Au-Ge phase diagram. The eutectic composition is reached at 28% Ge while the eutectic temperature amounts 634 K (361 °C). The growth process is indicated by the arrows from A to C. A: Au-Ge droplet saturated with Ge from the substrate. B: supersaturated Au-Ge droplet. The supersaturation is maintained by a continuous supply of Ge from the vapor phase. C: crystalized Ge in the nanowire.

For small spherical droplets surrounded by vapor the curvature or the droplet surface leads to an additional internal pressure p_{in} according to the Laplace equation

$$p_{in} = p_{ex} + \frac{2\sigma_l}{r} \tag{2.14}$$

where σ_l is the surface energy and r is the curvature radius of the droplet surface and p_{ex} is the ambient pressure. This leads to an increase of the vapor pressure p of the liquid according to $p = p_0 e^{\Delta p \Omega_l / k_B T}$ where p_0 is the vapor pressure in the case of a flat surface and $\Delta p = p_{in} - p_{ex} = 2\sigma_l / r$ or in terms of the chemical potential

$$\mu = \mu_0 + \frac{2\sigma_l \Omega_l}{r} \tag{2.15}$$

where Ω_l is volume per atom or molecule in the liquid. This is also known as Kelvin equation. The effect is of importance when studying the nucleation and formation of small droplets from the vapor as it is often the case in nanowire growth (see sec. 2.4.1)

The same treatment can be done in the case of spherical solid particles in a melt similar to Kelvin equation. This leads to an additional surface term in the Gibbs free energy $G_s = G_s^\circ + 2\sigma_{ls}\Omega_s / r$ where G_s° is the bulk energy per atom in the solid. With this, the standard enthalpy of melting is given by $\Delta_m H^\circ = T \Delta_m S^\circ + 2\sigma_{ls}\Omega_s / r$ where $\Delta_m S^\circ$ is standard entropy of melting per atom. On the other hand the standard bulk entropy of melting is given by $\Delta_m S^\circ = \Delta_m H^\circ / T_m^\circ$ [30, sec. 3.3]. Thus, substituting $\Delta_m H^\circ$ leads to the well known Gibbs-Thomson equation and describes the equilibrium melting point of spherical solid particles of radius r surrounded by their melt

$$T_m = T_m^\circ - \frac{2\sigma_{ls}\Omega_s}{r\,\Delta_m S^\circ} \tag{2.16}$$

Similar to the depression of the melting temperature of pure substances the position of liquidus lines and eutectic temperatures in binary phase diagrams can be shifted to lower temperatures. The calculation of those nanoscale phase diagrams is complex and subject to current research. Eichhammer et al. presented theoretical studies resulting in phase diagrams of the Au-Ge system for spherical alloy particles as well as particles in contact with the Ge nanowire [33]. They found the eutectic temperature of a 20 nm diameter alloy particle to be as low as 566 K at a composition of 25.5 at.% Ge. In comparison, their calculations yield an eutectic temperature of 520 K for a 20 nm alloy droplet in contact with the nanowire at a Ge content of 24 at.%. The calculated liquidus lines are depicted in figure 2.3.

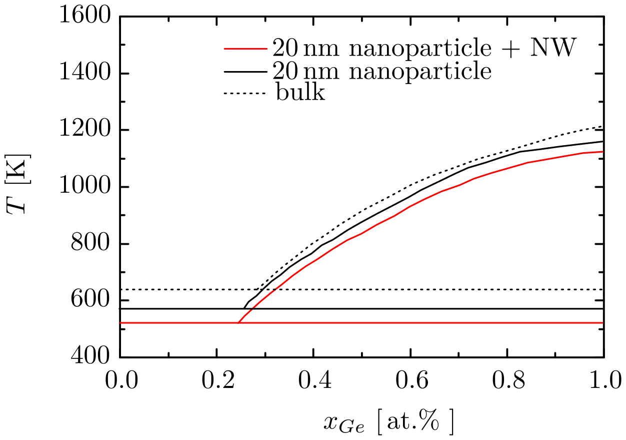

Figure 2.3: Binary Au-Ge phase diagram for nanoscales. Melting temperatures of pure germanium is lowered according to Gibbs-Thomson equation (2.16) and eutectic temperatures are lowered to 566 K (black solid curve) or 520 K (red curve). Dotted curve shows bulk liquidus line for comparison. Plot adopted from ref. [33]

As can be seen from above, surface effects have an important influence on the position of liquidus lines and thus on the resulting growth conditions. However, since droplet diameters in the frame of this thesis are considerably larger (typically 100 nm or more) these effects have not to be taken into account.

The validity of the Gibbs-Thomson equation has to be brought into question in the case of non-curved crystal facets as they occur in nanowire growth. This contradiction becomes even more obvious in the case of very thin films for which a decrease of the melting point with decreasing film thickness is observed although no curvature is present at the surface or interface [34]. Generalized theories have been developed to describe this phenomenon [35, 36].

Furthermore, size effects of surface tension itself are not considered in most cases. However, it is known since Gibbs [37] that the surface tension of droplets in a vapor phase decreases when their size decreases. Recent studies show, that this trend can be understood as a general rule [38]. Thus, the size dependence caused by Gibbs-Thomson effect may be compensated by the size dependence of surface tension.

2.4 Nucleation

When a system becomes supersaturated a so-called metastable equilibrium is reached, i.e. the total energy of the system can be lowered by phase transition but does not happen due to some energy barrier which has to be overcome. Instead of changing the mass density of the total system it is energetically preferable to initiate the phase transition locally in order to overcome the energy barrier. This process is triggered by density fluctuations leading to a local clustering of only a few molecules. Thus, nucleation is the first process that initiates a first-order phase transition.

On the one hand, the phase transition leads to a change of the chemical potential of atoms in the formed nucleus and therefore to a drop of the total energy. On the other hand, energy is needed for the formation of a phase boundary. The change in Gibbs free energy can be expressed as

$$\Delta G = -N\,\Delta\mu + E_A \tag{2.17}$$

where $\Delta\mu$ is the supersaturation, N is the number of atoms (molecules) in the cluster and E_A is the surface energy. This leads to the fact that the Gibbs free energy rises with increasing number of atoms in the cluster for very small clusters until a critical number atoms N^* is reached where ΔG exhibits a maximum. Hence, clusters containing $N < N^*$ atoms are unstable and can dissolve easily. Only clusters with more atoms than N^* are stable and can grow further.

There are two different types of nucleation, namely homogenous and heterogeneous nucleation. While homogenous nucleation occurs spontaneously where emerging clusters are only in contact with the old phase heterogenous nucleation occurs in the presence of surfaces of others than the old phase and is much more widespread in nature and tech-

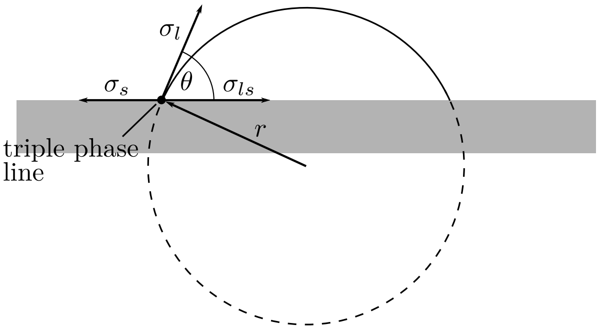

Figure 2.4: Section of a droplet on a substrate surface. r is the curvature radius and $r\sin(\theta)$ the radius of the contact area (interface) where θ is the wetting angle. σ denotes the surface energies of the different boundaries of the droplet. The corresponding arrows illustrate the resulting tangential components of the capillary forces acting at the triple phase line.

nology. In NW growth condensation of liquid droplets from the vapor on the substrate surfaces and crystallization of the growing species at the liquid-solid interface take place by heterogenous nucleation.

2.4.1 Nucleation of droplets

Gold droplets are created by evaporating gold from an effusion cell. The molecular beam can be understood as highly supersaturated vapor above the substrate which leads to heterogenous nucleation and eventually to the formation of droplets with diameters of several ten nanometers.

The considered geometry of cap-shaped clusters for the droplet formation is depicted in figure 2.4. Therefore the surface term in equation (2.17) can be written as

$$E_A = \sigma_l\, A_l + (\sigma_{ls} - \sigma_s)A_{ls} \tag{2.18}$$

where σ_l, σ_s and σ_{ls} are the specific surface energies of droplet and substrate as well as the specific interface energy between cluster and substrate. $A_l = 2\pi r^2\,(1-\cos(\theta))$ is the liquid surface area and $A_{ls} = 2\pi r^2 \sin^2(\theta)$ is the contact area between liquid and solid phase.

The surface energies are connected via the wetting angle according to Young's equation

$$\cos(\theta) = \frac{\sigma_s - \sigma_{ls}}{\sigma_l} \tag{2.19}$$

Substituting equation (2.19) into the surface term (2.18) the change in Gibbs free energy can be rewritten in terms of the cluster radius

$$\Delta G = -\frac{V}{\Omega_l}\,\Delta\mu + 2\pi r^2 \sigma_l \left(1 - \cos(\theta) - \frac{1}{2}\sin^2(\theta)\cos(\theta)\right) \tag{2.20}$$

where $V = \frac{4}{3}\pi r^3\ \frac{1}{4}\left(1-\cos(\theta)\right)^2\left(2+\cos(\theta)\right)$ is the volume of the cluster. Some calculations lead to a corresponding expression in terms of the total number of atoms in the cluster [39, sec. 3.2]

$$\Delta G = -N\,\Delta\mu + \left(36\pi\Psi N^2\Omega_l^2\right)^{1/3}\sigma_l \tag{2.21}$$

where $\Psi = \frac{1}{4}\left(1-\cos(\theta)\right)^2\left(2+\cos(\theta)\right)$ is the so-called wetting function and describes the wetting behavior of a liquid cluster on the substrate [40]. In equation (2.21) only the surface term, i.e. the second summand, depends on the wetting angle according to the idea that the surface energies determine the energy barrier which has to be overcome in order to form stable clusters or nuclei of the new phase. For the calculation of the energy barrier the maximum of ΔG has to be determined by solving $\partial(\Delta G)/\partial N = 0$ for N. The so-called critical number of atoms and the corresponding change in Gibbs free energy are given by

$$N^* = \frac{32}{3}\pi\Omega_l^2\Psi\frac{\sigma_l^3}{\Delta\mu^3} \tag{2.22}$$

$$\Delta G^* = \frac{16}{3}\pi\Omega_l^2\Psi\frac{\sigma_l^3}{\Delta\mu^2} \tag{2.23}$$

The number of atoms in such a drop-shaped cluster is connected with curvature radius via $N = \frac{4}{3}\,\pi r^3\,\frac{\Psi}{\Omega_l}$ which leads to the following critical radius

$$r^* = \frac{2\sigma_l\Omega_l}{\Delta\mu} \tag{2.24}$$

which, in fact is the Kelvin equation already known from equation (2.15). This means that nuclei of the critical radius are in equilibrium with the parent phase. However, since r^* refers to a maximum in ΔG the equilibrium is unstable (also called metastable equilibrium), i.e. if more atoms attach to the critical nucleus it will grow further or it can easily decay in the opposite case (see fig. 2.5).

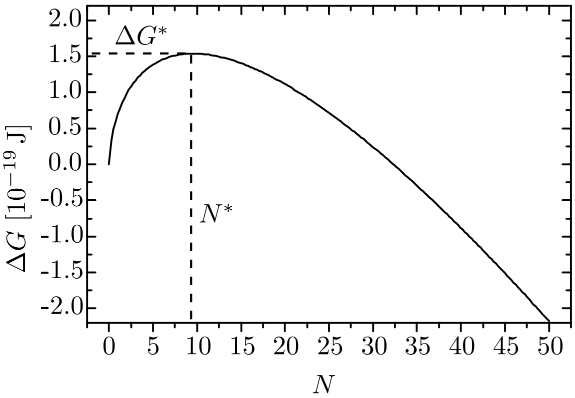

Figure 2.5: Plot of the Gibbs free energy per atom as a function the number of atoms. The maximum corresponds to the critical number of atoms or critical radius of the nuclei respectively.

2.4.2 2D nucleation

If the formation of more than one monolayer consumes more energy than expanding an already existing 2D cluster the so-called 2D nucleation is possible. This mode of nucleation mainly occurs in epitaxial growth on crystalline substrates as it is the case in NW growth at the liquid-solid interface. If the difference between interface energy σ_i and surface energy σ of a cluster and the surface energy σ_s of the substrate is zero or negative ($\Delta\sigma = \sigma + \sigma_i - \sigma_s \leq 0$) 3D nucleation is prohibited an only 2D nuclei can form in a supersaturated system. In the opposite case different nucleation modes can occur simultaneously. However, it can be shown that 3D nucleation is again prohibited above a critical supersaturation [40, sec. 2.1.5]. In particular, $\Delta\sigma = 0$ represents the situation of heterogenous nucleation on the so-called own or native substrate as it is the case in homoepitaxy.

The 2D cluster formation can be treated in the same way as the droplet formation in the section before. The change in Gibbs free energy of a round shaped disk is given by

$$\Delta G = -N\Delta\mu + \pi r^2(\sigma_i - \sigma_s + \sigma) + 2\pi r\kappa \tag{2.25}$$

where κ is the energy per unit length of the atoms at the circumference of the cluster. Similar to surface energy κ is approximately given by the energy of unsaturated bonds at the edge of the cluster. Equation (2.25) can be expressed in terms of the the total number of atoms in the cluster N as follows

$$\Delta G = -N\Delta\mu + a_0\,\Delta\sigma N + 2\kappa\,(\pi a_0 N)^{1/2} \tag{2.26}$$

where $a_0 = \Omega/h$ is the area per atom in a monolayer of height h. Determining the maximum of ΔG yields the following for the critical number of atoms in the cluster and the corresponding change in Gibbs free energy.

$$N^* = \frac{\kappa^2 a_0 \pi}{(\Delta\mu - a_0 \Delta\sigma)^2} \tag{2.27}$$

$$\Delta G^* = \frac{\kappa^2 a_0 \pi}{\Delta\mu - a_0 \Delta\sigma} \tag{2.28}$$

With the relation between number of atoms and cluster radius $N = \pi r^2/a_0$ the critical radius is found to be

$$r^* = \frac{\kappa a_0}{\Delta\mu - a_0 \Delta\sigma} \tag{2.29}$$

As can be seen, 2D nucleation can occur even at undersaturation in the case of complete wetting ($\Delta\sigma < 0$). The attracting adhesion forces between the substrate and the cluster atoms as they are present at complete wetting lead to the formation of stable nuclei in the non-saturated phase.

2.4.3 Droplet formation and Ostwald ripening

After droplets have nucleated further attachment and detachment of atoms may take place while atoms coming from the molecular beam still diffuse along the substrate surface. Thereby, the growth of droplets depends on the diffusion of adatoms which is a temperature dependent process as it is described in section 2.6.1. Higher temperature lead to larger diffusion length of adatoms such that it is more likely to be captured by an already existing droplet instead of taking part in a new nucleation event. In this sense, the so-called capture cross section of existing droplets increases with temperature. As a consequence, many small droplets can be expected in the final stage at lower temperatures compared to less but bigger droplets at higher temperatures.

However, in general the size distribution of an ensemble of droplets changes with time such that the average radius increases with time. This process is called Ostwald ripening named after Wilhelm Ostwald who described this phenomenon first in 1900 [41]. During this process larger droplets grow at the expense of smaller droplets which have a higher vapour pressure according to the Kelvin equation (2.15). The time evolution of Ostwald ripening has been described first by Lifshitz and Slyozov in 1961 and has been derived for the case that diffusion is the slowest process and as such dominates the ripening [42].

2.5 Film growth modes

The growth mode of epitaxial films is based on interactions between substrate and deposited film. Three different cases can be distinguished [43, sec. 14.1] by the resulting morphology of the films (see fig. 2.6).

Volmer-Weber growth occurs if cohesion forces between deposited atoms are stronger than adhesion between the film and the substrate. This situation corresponds to the case $\Delta\sigma > 0$ (see section 2.4.2) and results in the formation of well separated islands.

Frank-van der Merwe growth is observed if the adhesion forces between substrate and deposited atoms are stronger than the cohesion forces which corresponds to $\Delta\sigma \leq 0$ and results in layer by layer growth, e.g. in homoepitaxial growth.

Stranski-Krastanov growth describes the situation when the deposited material has a different lattice constant than the substrate producing strain in the film as well as in the substrate. In the first stage, a strained wetting layer forms (pseudomorphic growth) accommodating strain with the associated energy ε. With increasing thickness the strain energy also rises rapidly. To minimize the total energy which is determined by $\sigma_{tot} = \Delta\sigma + \varepsilon$ strain can be relieved by island formation in a dislocated [44] or coherent (dislocation-free) fashion [45]. The thickness of the wetting layer at which island formation sets in is called the critical thickness.

This classification is based on thermodynamic considerations. Nevertheless, kinetic effects like diffusion in the presence of defects like steps (different diffusion length along or perpendicular to a step) can lead to different morphologies than expected from the thermodynamic point of view. Thus, island formation can occur also in homoepitaxy due to diffusion barriers (Ehrlich-Schwoebel barrier, see sec. 2.6.2).

2.6 Material transport

In general there are two main principles for material transport in crystal growth, namely diffusion and convection. While natural convection plays an important role for the growth of large crystals, it is the diffusion governing the material transport on nanometer scales. In this section diffusive material transport as an important process during MBE growth is described. While surface energies, strain and supersaturation determine the growth mode from the thermodynamic point of view, diffusion is referred to as a kinetic process considering the motion of particles rather than the energy state.

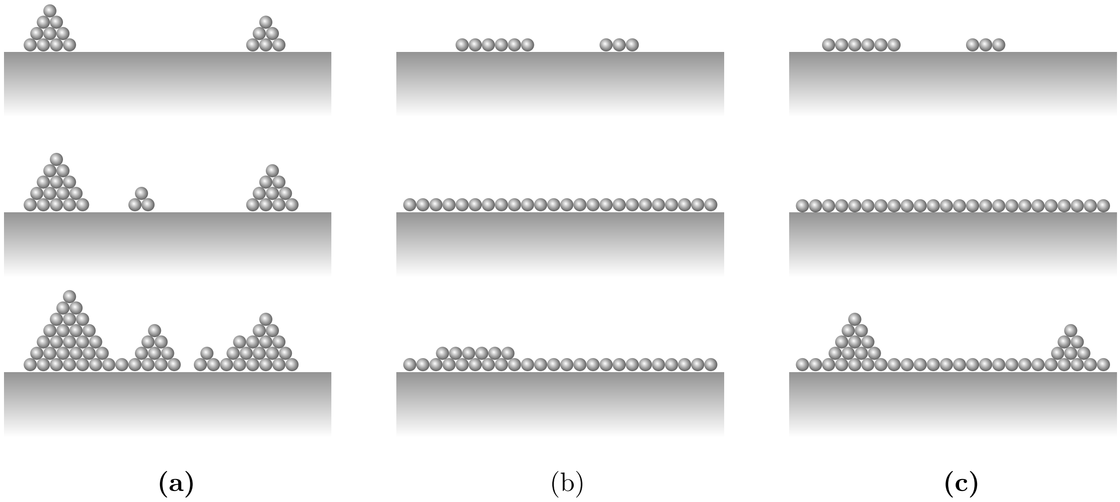

(a) (b) **(c)**

Figure 2.6: Evolution during film growth in different growth modes as described in the text. (a) Volmer-Weber growth exhibiting island growth from the beginning. (b) Frank-van der Merwe growth in a layer-by-layer fashion. (c) Stranski-Krastanov growth. After pseudomorphic growth of a strained wetting layer strain is relieved by the formation of islands.

2.6.1 Diffusion

Diffusion describes the random motion of particles from regions with higher concentration of particles to regions with lower concentration. The net particles flux J is given by Fick's first law and follows the negative gradient of the particle concentration n and is proportional to the diffusion coefficient D [43].

$$J = -D\,\nabla n \tag{2.30}$$

The time evolution of the particle concentration which is caused by diffusion follows by considering the mass conservation $\frac{\partial n}{\partial t} + \nabla J = 0$. This leads to Fick's second law

$$\frac{\partial n}{\partial t} = \nabla(D\,\nabla n) \tag{2.31}$$

Assuming the diffusion coefficient to be constant with respect to space coordinates gives Fick's second law in the diffusion equation in the well known form

$$\frac{\partial n}{\partial t} = D\,\nabla^2 n \tag{2.32}$$

While Fick's laws are applicable to diffusion phenomena in general, the diffusion coefficient is determined by the microscopic mechanisms that leads to motion of the diffusing particles. As such, surface diffusion can be considered as a process resulting from adatoms jumping from one adsorption site to another on a 2D lattice. Jumping or hopping is the most basic mechanism for diffusion of adatoms [43]. Thus, motion occurs by successful jumps from one adsorption site to another. The diffusion coefficient (also called intrinsic diffusion coefficient) is mainly determined by the number of jumps per time interval and can be given following an Arrhenius law

$$D = \frac{a^2}{z} \nu e^{\frac{-E_{dif}}{k_B T}} \tag{2.33}$$

where a is the lattice constant of the 2D lattice of absorption sites, z gives the number of different directions (4 on square lattice, 6 on the hexagonal lattice, etc.). The vibrational frequency ν of the adatoms multiplied with a Boltzmann factor depending on the diffusion energy barrier E_{dif} and temperature T gives the number of successful jumps per time interval.

In the case of diffusion along real surfaces which contain defects like steps, kinks, vacancies or other adatoms the mobile species can be trapped or generated at these defect sites. If the separation of the defects is smaller than the average distance over which the diffusion proceeds (diffusion length λ) the diffusion coefficient is influenced by the areal density of the defects and one speaks of mass transfer diffusion [43, sec. 13.2]. The resulting mass transfer diffusion coefficient is related to the number of the mobile species which depends on the formation energy of adatoms on the surface ΔE_a leading to

$$D_m = \frac{\nu a^2}{z} e^{-\frac{\Delta E_a + E_{dif}}{k_B T}} \tag{2.34}$$

2.6.2 Ehrlich-Schwoebel barrier

A special case of diffusion in the presence of defects is diffusion across a step edge where the diffusion is hindered due to an additional energy barrier E_{ES} which is depicted in figure 2.7. This has been found first experimentally by Ehrlich and Hudda [46] and interpreted theoretically by Schwoebel [47]. The Ehrlich-Schwoebel barrier is defined as the difference between the diffusion energy of the the substrate and the energy of the step edge $E_{ES} = E_{stp} - E_{dif}$. Under certain conditions when $E_{dif} < k_B T < E_{stp}$ is fulfilled on a terraced surface diffusion takes place only on the terraces which results in three dimensional growth although layer growth is preferred from thermodynamic considerations. Consequently, Schwoebel treated filamentary growth (whisker growth) as a special case where E_{ES} evokes one-dimensional growth of the top-facet of an island [48].

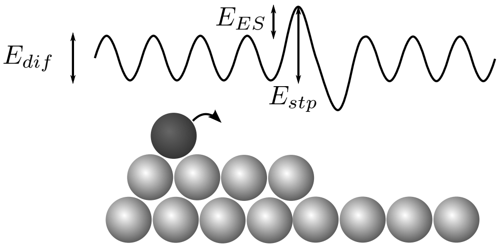

Figure 2.7: Potential of a diffusing adatom near a step edge according to Schwoebel [47].

2.7 Nanowire growth models

Since the growth of silicon whiskers was reported in 1964 many approaches have been undertaken to describe the growth of NW. Both, thermodynamic aspects of nanometer sized structures have been considered as well as kinetic models. Thermodynamic approaches are mostly related to Gibbs-Thomson effect to describe the potential for growth while kinetic models refer to concentration gradients of species to describe material transport by surface diffusion. While the former consider the growth itself meaning material transport from the parent phase to the growing one, the latter assume material transport towards to growth front as being the dominating process. Both approaches lead to different results especially for the radius dependency of the growth rate as will be shown below. In literature either thermodynamic or kinetic models fit best the experimental data depending on the respective growth conditions.

In the following two sections two simplified models will be presented describing both the thermodynamically driven growth of nanowires on the one hand and the diffusion limited growth on the other hand.

2.7.1 Thermodynamic growth model

The first growth model to describe nanowire growth with the help of thermodynamic aspects was presented by Givargizov [49]. He attributed the low dimension of nanowires by correcting the change of the chemical potential during the nucleation process according to Gibbs-Thomson effect (see section 2.3.3).

$$\Delta\mu = \Delta\mu_0 - \frac{2\sigma_w\Omega}{r} \tag{2.35}$$

Here Ω is the atomic volume of the the growing species in the solid and σ_w is the specific surface energy of the nanowire.

Furthermore, the growth rate of a single crystal face as a function of supersaturation can be assumed to be proportional to the n-th power of $\Delta\mu$

$$\frac{dL}{dt} \propto \left(\frac{\Delta\mu}{k_B T}\right)^n \quad \Leftrightarrow \frac{dL}{dt} = b\left(\frac{\Delta\mu}{k_B T}\right)^n \tag{2.36}$$

where b is a kinetic coefficient and n is a number which has to be determined from experiments, e.g. $n = 1$ in the case of linear growth with a rough interface. Givargizov found $n = 2$ to fit his experimental data best (growth rate vs. length). Substitution of equation (2.35) in the growth rate yields

$$\frac{dL}{dt} = b\left(\frac{\Delta\mu_0}{k_B T} - \frac{2\sigma_w\Omega}{r k_B T}\right)^n \tag{2.37}$$

From this equation it can be seen, that Gibbs-Thomson effect leads to a decrease of the growth rate with decreasing radius until a critical radius r^* is reached where growth stops $\left({}^{\Delta\mu_0}/_{k_B T} - {}^{2\sigma_w\Omega}/_{r^* k_B T} = 0\right)$.

$$r^* = \frac{2\sigma_w\Omega}{\Delta\mu_0} \tag{2.38}$$

In this case the supplied supersaturation is completely neutralized due to the curvature of the nanowire. Thus, the higher the supersaturation is the thinner nanowires can be grown. Such a relation between radius and growth rate has been found by Dayeh and Picraux [50] for MOCVD grown nanowires very similar to the results of Givargizov. Obviously, the growth rate is dominated by thermodynamic effects for CVD grown nanowires where the species are deposited preferentially at the catalyst droplet and no material transport by surface diffusion is required. As will be shown in the next section, the opposite case of diffusion induced growth leads to a different relation between nanowire and radius.

2.7.2 Kinetic growth controlled by surface diffusion

In contrast to the thermodynamic model in the previous section, a diffusion model is presented without thermodynamic size effects such as Gibbs-Thomson effect. Merely the material transport is discussed. As already discussed in section 2.6 surface diffusion plays an important role in epitaxial growth especially by MBE. Not only layer growth is influenced by adatom diffusion, but also nanowire growth can be considered as highly dependent on surface diffusion. The better atoms can diffuse along the substrate and nanowire towards the catalyst droplet the higher growth rates can be expected. To analyze influences of surface diffusion during growth of nanowires a model describing the

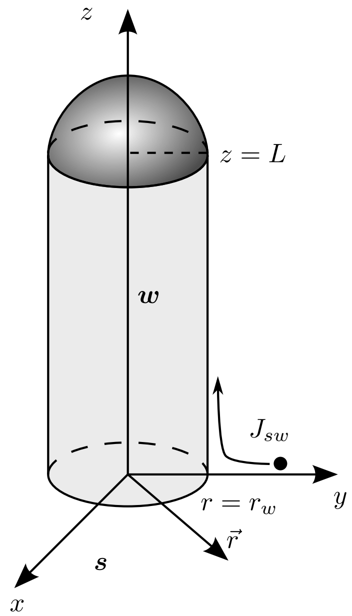

Figure 2.8: Schematic of the coordinate system that is used for the calculations. The domains substrate surface (s) and nanowire sidewalls (w) are indicated where the two differential equations are solved. The adatom flux J_{sw} from the substrate to the nanowire interconnects the two differential equations.

material transport along the substrate and the nanowire is required.

Following Johansson et al. [51], a diffusion model is used to derive the adatom concentration on the substrate as well as on the nanowire. Thus, the resulting material transport to the droplets and the corresponding growth rate of the wires can be calculated. The geometry that has been considered is depicted in figure 2.8.

For simplicity some general assumptions are made: (1) The metal particle is assumed to be hemispheric and (2) there are steady state diffusion conditions from the substrate, along the wire towards the metal particle, (3) the processes inside the particle as well as nucleation processes at the droplet–wire interface have not to be considered, since they are assumed to be much faster and thus not limiting the total growth rate and (4) the inter wire separation is large compared to the diffusion length of the growth species.

The molecular beam impinges on the substrate at a certain rate and species subsequently diffuse until they are incorporated into a catalyst droplet at the beginning of the growth process or reach the base of an already existing nanowire later on. The fundamentals of the model are two diffusion equations, interconnected via the adatom flux J_{sw} from the substrate to the nanowire base to obey mass conservation.

Diffusion towards the nanowire

Diffusion on the substrate can be described by the following equation.

$$D_s \nabla^2 n_s - \frac{n_s}{\tau_s} + R_s = \frac{\partial n_s}{\partial t} \tag{2.39}$$

In equation (2.39) D_s is the diffusivity of the adatoms on the substrate, τ_s is the average time an atom diffuses on the substrate, R_s is the impingement rate of the material coming from the gas phase.

Nanowires can be treated as a sink for diffusing atoms because any adatom that reaches a nanowire is supposed to be incorporated into the wire and thus leaves the substrate. Therefore, the density on the substrate n_s goes towards zero at $r = r_w$.

Since assumption (4) is fulfilled, the adatom density far from the nanowire is equal to $R_s\tau_s$ which leads to the two initial conditions for solving equation (2.39).

$$n_s(r_w) = 0 \qquad n_s(r \to \infty) = R_s\tau_s \tag{2.40}$$

With respect to the symmetry of the problem (cylindrical) polar coordinates are introduced. The adatom density is supposed to have no angular or z dependency which reduces the Laplace operator to the following term

$$\nabla_r^2 = \frac{\partial^2}{\partial r^2} + \frac{1}{r}\frac{\partial}{\partial r} \tag{2.41}$$

The general steady-state solution ($\partial n_s/\partial t = 0$) of diffusion equation 2.39 in cylindrical coordinates has the form

$$n_s(r) = C_1\, I_0\left(\frac{r}{\lambda_s}\right) + C_2\, K_0\left(\frac{r}{\lambda_s}\right) + R_s\tau_s \tag{2.42}$$

where $\lambda_s = \sqrt{D_s\tau_s}$ is the diffusion length of the atom on the substrate, C_1 and C_2 are constants which are determined by initial conditions and I_0 and K_0 are the 0th order modified Bessel functions of the first and second kind respectively. Because a bounded solution is needed C_1 must be equal to zero. Inserting the initial condition $n_s(r_w) = 0$ into equation (2.42) leads to the bounded, steady-state solution of equation (2.39)

$$n_s(r) = R_s\tau_s\left(1 - \frac{K_0\left(\frac{r}{\lambda_s}\right)}{K_0\left(\frac{r_w}{\lambda_s}\right)}\right) \tag{2.43}$$

Diffusion along the nanowire

The effective diffusion along the nanowire is assumed to be one-dimensional along the z direction and can thus be described by the following equation

$$D_w \nabla_z^2 n_w - \frac{n_w}{\tau_w} + R_w = \frac{\partial n_w}{\partial t} \tag{2.44}$$

where n_w, τ_w, D_w and R_w are adatom density, diffusion time, diffusivity and rate of impingement on the nanowire. The steady-state solution of equation (2.44) has to obey the following conditions. The adatom density at the end of the wire ($z = L$) is equal to zero because every adatom is incorporated into the wire at this point according to assumption (3). The adatom flux at the base of the wire ($z = 0$) has to be equal to the adatom flux J_{sw} coming from the substrate to obey mass conservation. This leads to the following boundary conditions

$$n_w(L) = 0 \qquad D_w \frac{\partial n_w(0)}{\partial z} = -D_s \frac{\partial n_s(r_w)}{\partial r} = J_{sw} \tag{2.45}$$

The Laplace operator of the z component in cylindrical coordinates is given by $\frac{\partial^2}{\partial z^2}$. Thus, steady-state solution obeying these conditions can be written in following form

$$n_w(z) = \frac{R_w \lambda_w^2}{D_w} \left[1 - \frac{\cosh(\frac{z}{\lambda_w})}{\cosh(\frac{L}{\lambda_w})} \right] - \frac{\lambda_w}{D_w} J_{sw} \frac{\sinh(\frac{L-z}{\lambda_w})}{\cosh(\frac{L}{\lambda_w})} \tag{2.46}$$

where λ_w is the diffusion length along the nanowire. The adatom flux from the substrate to the nanowire is given by

$$J_{sw} = -R_s \lambda_s \frac{K_1(\frac{r_w}{\lambda_s})}{K_0(\frac{r_w}{\lambda_s})} \tag{2.47}$$

Nanowire growth rate

The nanowire growth rate is determined by the number of adatoms reaching the droplet per unit time which is given by the adatom flux along the nanowire sidewalls at the end of the wire $J_w(z = L)$ multiplied with the circumference of the nanowire $2\pi r_w$. Thus, the vertical growth rate can be expressed as the number of adatoms per unit time and unit area multiplied with the atomic volume Ω of the growth species in the solid. Direct impingement of the growth species on the droplet gives an additional contribution $R_d\Omega$

to the entire growth rate.

$$\frac{dL}{dt} = \frac{J_w(L)2\Omega}{r_w} + R_d\Omega \tag{2.48}$$

where R_d is the effective incorporation rate of atoms, that are captured by the droplet. For example, in CVD processes the ratio between the droplets mantle surface (assumed to be hemispherical) and the nanowire cross-sectional area gives a factor of 2 between the impingement rate and R_d. For MBE growth direction of the molecular beam is roughly along the surface normal which means that R_d can be assumed to be equal to R_s. This can be considered as an upper limit because not every atom which reaches the droplet will be incorporated into the nanowire.

The final result for the growth rate can be expressed as

$$\frac{dL}{dt} = \frac{2\Omega R_w \lambda_w}{r_w} \tanh\left(\frac{L}{\lambda_w}\right) - \frac{2\Omega J_{sw}}{r_w \cosh(\frac{L}{\lambda_w})} + R_d\Omega \tag{2.49}$$

where the first summand represents contributions from direct impingement on nanowire sidewalls, the second summand describes contributions from the substrate and the last summand stands for the direct impingement on the droplet.

For very long nanowires the contribution of diffusion from the substrate can be neglected. Thus, for $L \gg \lambda_w$ the growth rate reduces to

$$\frac{dL}{dt} = \frac{2\Omega R_w \lambda_w}{r_w} + R_d\Omega \tag{2.50}$$

Apparently, within the scope of this model the growth rate increases with decreasing nanowire radius which coincides with experimental results regarding MBE grown nanowires [52–54]. This observations are typical for diffusion limited nanowire growth. Such a behavior was also observed at CVD grown GaAs nanowires at very high V/III ratios where As diffusion toward the gold droplet is the limiting process and therefore shows an increasing growth rate at decreasing droplet radii [55].

Temperature dependence

Within the derived diffusion model the diffusion length λ_s and λ_w in equation (2.49) are the only parameters showing a strong temperature dependency.

Different effects influence the diffusion length with changing temperature. In general, the diffusivity is expected to increase with temperature according to the Arrhenius law. On the other hand, also desorption as a statistical process becomes more likely with in-

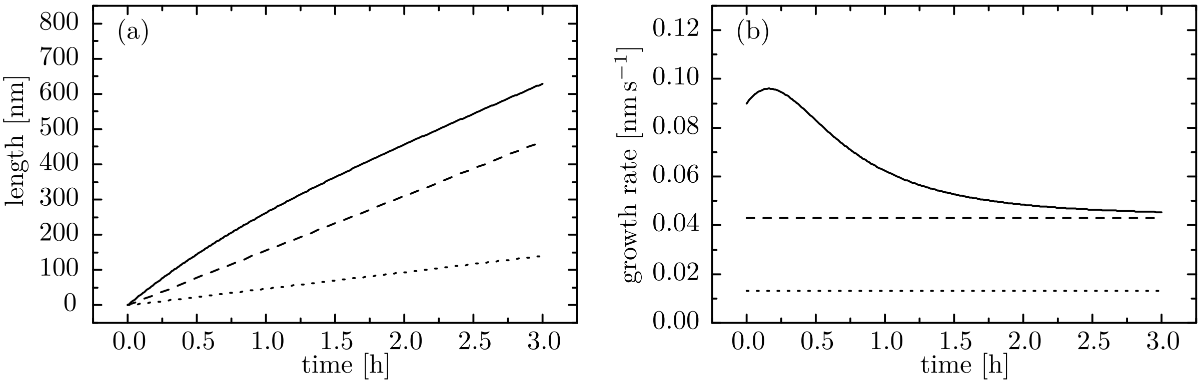

Figure 2.9: (a) NW length and (b) growth rate. Solid lines show the data according to equation (2.49). Dashed lines represent the growth without contribution from the substrate (only impingement on NW sidewalls and droplet). Pointed lines show the growth according to the nominal deposition rate which is $R_s = 0.013\,\mathrm{nm\,s^{-1}}$.

creasing temperature. Adatoms that migrate on the substrate can actually be captured by islands, nanowires, and droplets or can be desorbed. Thus, the effective diffusion length is a function of areal density of nanowires and islands, too. While the nanowire density is essentially given by the catalyst droplets, the island density is typically determined by the nucleation rate which is a function of substrate temperature and it decreases with increasing temperature [40, sec. 2.2.9].

Following Dubrovskii et al. [56] the temperature dependent diffusion length can be described considering the effects mentioned above. The diffusion along NW sidewalls is assumed to be affected only by desorption. Eventually, for the case of well separated nanowires one can find the following expressions for λ_s and λ_w

$$\lambda_s = \frac{1}{\sqrt{2\pi N_w + 2\pi N_{i,0}\, e^{2F_s\left(\frac{T_0}{T}-1\right)} + \lambda_0^{-2}\, e^{-2G_s\left(\frac{T_0}{T}-1\right)}}} \tag{2.51}$$

$$\lambda_w = \lambda_0\, e^{G_s\left(\frac{T_0}{T}-1\right)} \tag{2.52}$$

where N_w is the nanowire density and $N_{i,0}$ the island density at temperature T_0. λ_0 ist the surface diffusion length in absence of any surface hindrances (wires, droplets, islands). The parameters $G_s = (E_{des} - E_{dif})/2k_BT_0$ and $F_s = (3\Lambda_s + 2E_{dif})/2k_BT_0$ are determined by the activation energies for diffusion and desorption (E_{dif},E_{des}) and by the specific condensation heat of surface atoms (Λ_s) where a comparison with equation (2.34) yields $\frac{3}{2}\Lambda_s = \Delta E_a$. Figure 2.10 shows a plot of diffusion length λ_s and λ_w in a temperature range typical for germanium nanowire growth.

The calculated diffusion length on the substrate can be understood as an effective

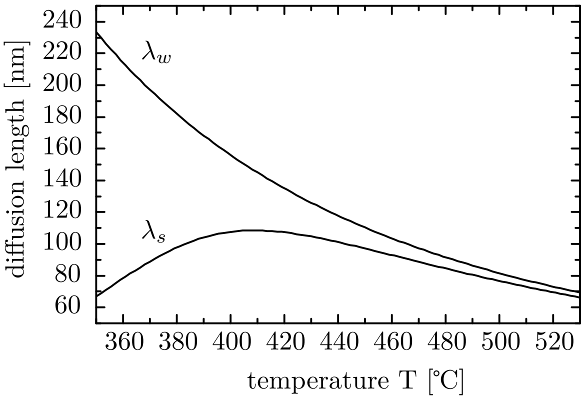

Figure 2.10: Temperature dependence of diffusion length on substrate and NW. Island and NW density are typically of the order of $10^{12}\,\mathrm{m}^{-2}$. The following values have been used for the plot: $N_{i,0} = 1.5 \times 10^{12}\,\mathrm{m}^{-2}$, $N_w = 3 \times 10^{12}\,\mathrm{m}^{-2}$, $\lambda_0 = 120\,\mathrm{nm}$, $F_s = 10$, $G_s = 5$.

diffusion length which has been gained by introducing the probability of an adatom being captured by a nanowire or an island respectively. Substituting expressions (2.51) and (2.52) into equation (2.49) gives the temperature dependence of the growth rate in a diffusion dominated regime.

2.7.3 Involving thermodynamic and kinetic effects

In a kinetic model as it is presented in the previous sections size dependent thermodynamic effects such as Gibbs-Thomson effect are not considered. This assumption is valid as long as the growth is rather dominated by surface diffusion. This can be explained by the nature of physical vapor deposition. While in CVD the material can be deposited selectively by cracking the precursor catalytically at the droplet, in MBE the material is deposited on the entire substrate. Thus, the material transport towards the droplets plays a crucial role for the resulting nanowire growth rate. In this way it is possible to classify the regime of nanowire growth by determining the growth rate at different droplet radii.

Nevertheless, at some critical radius the size dependent thermodynamic effects should predominate the total growth rate. Indeed, there are reports about radius dependent nanowire growth showing an increase of the growth rate with the radius until a maximum is reached. The growth rate drops again at radii beyond the maximum. Obviously, a transition between Gibbs-Thomson dominated growth and diffusion dominated growth was found.

Introducing Gibbs-Thomson effect into a diffusion model requires modified boundary conditions especially at the droplet-nanowire interface where the chemical potential

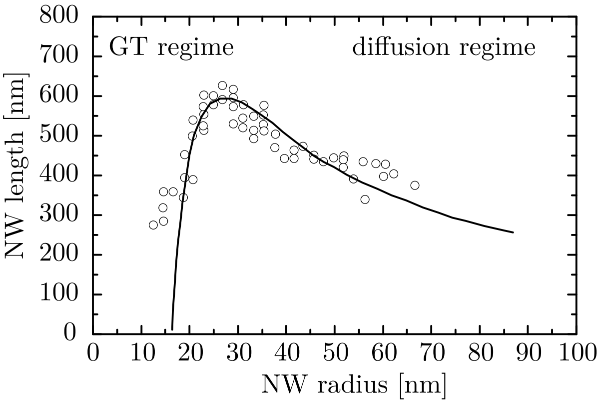

Figure 2.11: NW growth considering Gibbs-Thomson (GT) effect and surface diffusion in the case of GaAs nanowires grown by MBE. At very small radii GT effect predominates diffusion induced growth. In diffusion regime typically As diffusion towards the droplet limits the growth rate (figure adopted from [58]).

should be continuous. This means that $n_w(z = L) = 0$ as it is assumed in equation (2.45) is not valid in this case. A first approach to describe the chemical potential as a function of the adatom density can be done by introducing the coverage $\Theta = n_w \delta_s$ with δ_s as the area of an adsorption site. Hence, the chemical potential of adatoms at low coverage ($\Theta \ll 1$, also called non-interacting dilute lattice gas) is given by [57, sec. 10.2]

$$\mu = \mu_0 + k_B T \ln(\Theta) \tag{2.53}$$

Such a model has been presented by Dubrovskii et al. [58] leading to a much more complex form of the resulting growth rate which is not described in detail in the scope of this thesis. However, good agreement with experimental results from MBE grown GaAs nanowires was demonstrated. The results including a fit of the data with the model are depicted in figure 2.11.

3 Experimental Setup and Sample Processing

In the scope of this thesis, all samples have been processed by means of MBE. The process chamber is part of a UHV cluster (see. figure 3.1) which is located inside a clean air tent providing nominal cleanroom class 100 (max. 100 particles/ft^3 with size $\geq 5\,\mu\text{m}$). The entire UHV cluster is designed to handle four inch wafers at maximum. In this chapter MBE equipment as well as sample processing are described in detail.

3.1 MBE setup

The MBE chamber (Octoplus$^+$ 500) as well as the evaporators were supplied by the company Dr. Eberl MBE-Komponenten. The sample manipulator can handle up to four inch wafers and the substrate heater reaches temperatures up to 1000 °C which is sufficient to desorb silicon oxide under UHV conditions. The pump system consists of a turbo molecular pump together with a cryo pump exhibiting a base pressure of 1×10^{-10} mbar. This excellent vacuum is needed to provide very long mean free path (≈ 1800 km at 10^{-10} mbar) of the evaporated atoms to form a molecular beam that does not interact with the atmosphere in the chamber. Additionally, a nitrogen cooling shroud is integrated into the chamber to cool the inner walls for gettering residual gases and providing a cleaner atmosphere.

The chamber is equipped with two standard effusion cells for metal evaporation, one high temperature effusion cell for germanium evaporation, two electron beam evaporators for silicon or refractory metals, one hydrogen cracker cell and an oxygen cracker cell to provide atomic, ion-free gas beams and a silicon sublimation source to provide extremely small silicon rates.

Several in-situ diagnostics are attached to the chamber such as RHEED, residual gas analyzer (RGA) , quartz crystal microballance (QCM) rate monitor (see fig. 3.2).

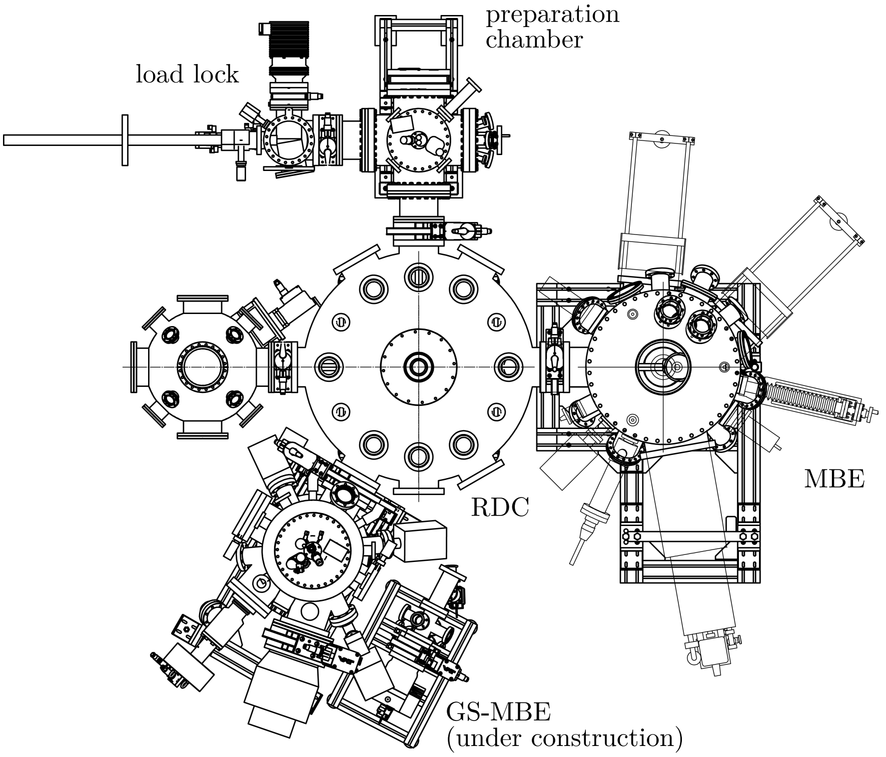

Figure 3.1: Top view on UHV cluster as it is installed in the institute. Samples are inserted at the load lock. After pump down they are transferred through preparation chamber and radial distribution chamber (RDC) (base pressure $10^{-8} - 10^{-9}$ mbar) into the MBE chamber.

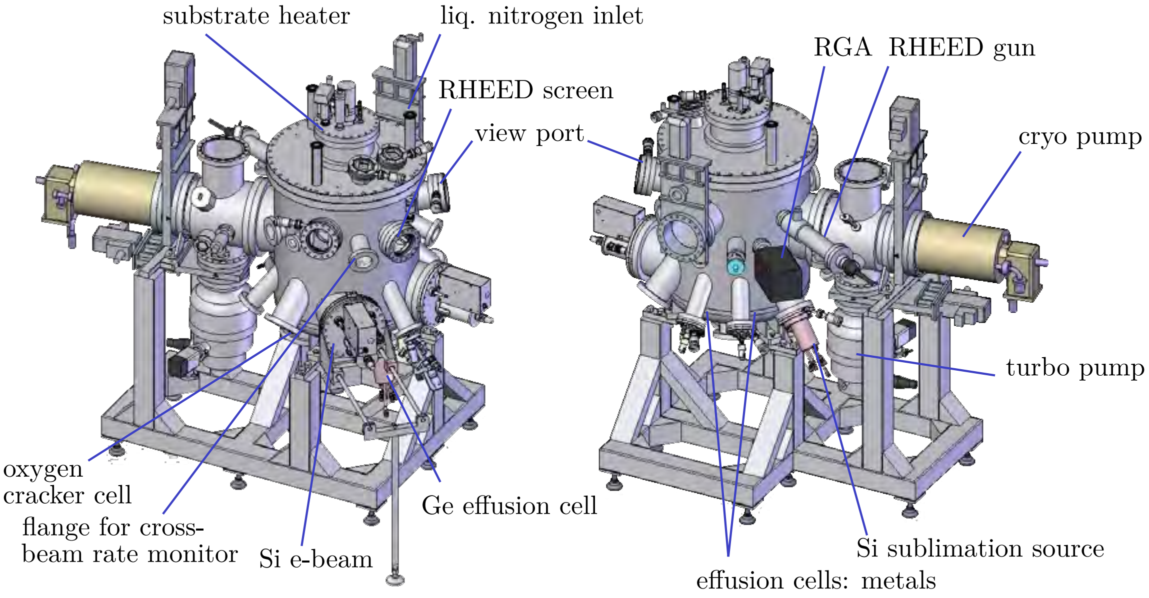

Figure 3.2: Two views on the MBE chamber. Graphics provided by Dr. Eberl MBE-Komponenten.

3.1.1 Effusion cells

Effusion cells are typical evaporators for MBE. They consist of a crucible mostly made of pyrolytic boron nitride (PBN) containing high purity material. The crucible is surrounded by resistive heaters typically made of carbon or refractory metals like tantalum. Heat shields are attached at the top of the cell containing an aperture to form the molecular beam.

The evaporated material is molten in order to get sufficiently high vapor pressure which determines the evaporation rate. The vapor pressure is only a function of the material's temperature according to

$$p_v = p_0\, e^{-\frac{\Delta_v H}{N_A k_B}\left(\frac{1}{T}-\frac{1}{T_0}\right)} \tag{3.1}$$

where p_0 is a known vapor pressure at temperature T_0 and $\Delta_v H$ the molar evaporation enthalpy. Knowing this, the evaporation rate can be calculated by

$$W = \frac{p_v - p_{at}}{\sqrt{2\pi m k_B T}} \tag{3.2}$$

which goes back to Langmuir but is also called the Hertz-Knudsen relation. Here p_v is the vapor pressure and p_{at} is the surrounding pressure which means the pressure inside the MBE chamber in our case. At UHV condition p_{at} can assumed to be zero which leads to the formula already used to derive the chemical potential of a molecular beam in equation (2.13).

The evaporation rate W and the resulting deposition rate can differ significantly due to geometrical conditions, i.e. what portion of evaporated atoms can reach the substrate. This portion is basically determined by mounting positions of source and sample as well as by the angular distribution of the evaporation of effusion cells. An ideal Knudsen cell shows a distribution following a cosine law $W(\theta) = W\cos(\theta)$ [59, sec. 5.2] while standard effusion cells deviate from cosine law. Furthermore, the net deposition rate is determined by the so-called sticking coefficient giving the fraction of all impinging atoms that are really adsorbed on the surface. This coefficient is a function of substrate temperature as it decreases with increasing temperature due to desorption processes. The final growth rate can thus be obtained by an additional factor η containing those coefficients giving the fraction of the deposited atoms from all evaporated atoms.

$$R = \eta\, W\, \Omega = \frac{\eta\, p_0\, \Omega}{\sqrt{2\pi m k_B T}} e^{-\frac{\Delta_v H}{N_A k_B}\left(\frac{1}{T}-\frac{1}{T_0}\right)} \tag{3.3}$$

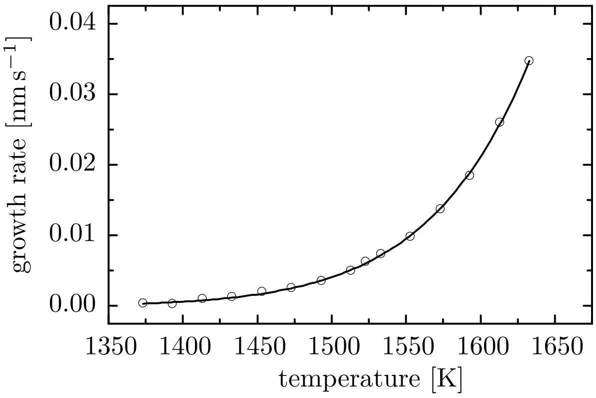

Figure 3.3: Deposition rate as a function of effusion cell temperature. Experimental data (circles) have been fitted with the model in eqn. (3.3) yielding $\eta = 2.4 \times 10^{-4}$. The following parameters have been used: $m_{Ge} = 72.63\,\mathrm{u}$; $\Delta_v H = 334\,\mathrm{kJ\,mol^{-1}}$; $\Omega = 2.26 \times 10^{-29}\,\mathrm{m^3}$; $p_0 = 1\,\mathrm{Pa}$; $T_0 = 1644\,\mathrm{K}$ [60, p. 6-75]

In general, η is also a function of temperature as desorption lowers the sticking coefficient with increasing temperature. Figure 3.3 shows the growth rate of the high temperature effusion cell that was used for germanium evaporation. The data were acquired using a QCM. Fitting the data with equation (3.3) yields the coefficient η. However, to extract the sticking coefficient from η is not possible without knowing the particle flux that impinges on the substrate surface.

The deposition rate is set by PID controllers using the cell temperature as control parameter. As long as the cell temperature is kept stable the evaporation rate of effusion cells is very stable and provides high accuracy and reproducibility.

3.1.2 Electron beam evaporator and rate control

Materials with a high melting point or low vapor pressure, such as silicon or refractory metals can hardly be evaporated using standard effusion cells having typical operating temperatures up to 1400 °C, because no sufficient vapor pressure can be reached up to this temperature. Therefore, electron beam evaporators are used to heat the material. Electrons are accelerated by high voltage of typically several kilovolts whereas the heating power is set by adjusting the beam current. Because the material is only heated in the vicinity of regions where electrons hit the target the beam is usually sweeped across the target. Additionally to evaporation from the locally molten target, a significant fraction of material is sublimated directly depending on the specific sublimation heat.

In the MBE chamber used in this work silicon is evaporated from an electron beam evaporator having a 100 cm^3 crucible and several silicon shielding elements in order to

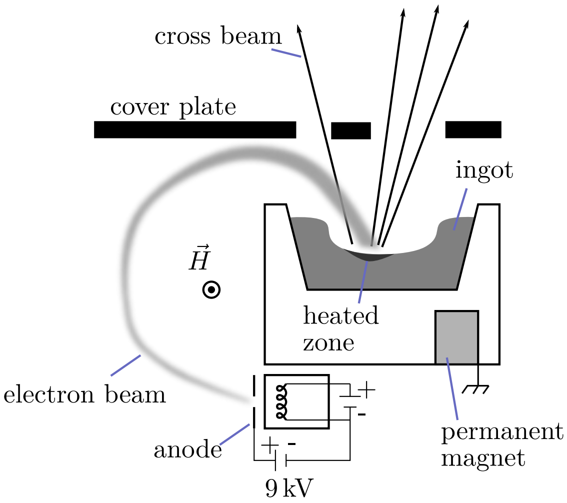

Figure 3.4: Principle of an electron beam evaporator. A permanent magnet leads to a 270° bending of the electron beam. The magnet also catched low energy electrons which are created upon electron impact. The beam is positioned and sweeped across the target by additional deflection coils (not shown). The cross beam points towards a measuring head of a RGA to control evaporation rate.

avoid contamination from co-evaporated metals of the housing.

The continuous impact of electrons onto the target leads to non-stable evaporation rate. The longer the evaporator is operated the more the target is heated up leading to increasing evaporation at constant emission current. Therefore a so-called cross beam rate control has been installed. A second beam (cross beam) is formed through a second hole in the cover plate of the evaporator. This beam crosses a RGA measuring head of a mass spectrometer positioned above the evaporator. Thus the silicon flux through the measuring head can be used as control parameter to keep the evaporation rate constant. A small aperture on the measuring head avoids crosstalk between the deposition beam and the cross beam. Figure 3.4 shows the operating principle of the installed evaporator.

3.1.3 Quartz crystal monitor

Quartz crystal monitors measure deposited material thickness as a function of the resulting shift of the resonance frequency of an oscillating quartz crystal. Quartz is a piezoelectric crystal for which the relation between applied voltage and mechanical deformation is well known. Therefore, in an appropriate cut crystal standing shear waves are generated when alternating voltage is applied. Those quartz oscillators exhibit very high quality factors up 10^6. Thus, common crystals with a resonance frequency of 6 MHz provide resolution down to 1 Hz.

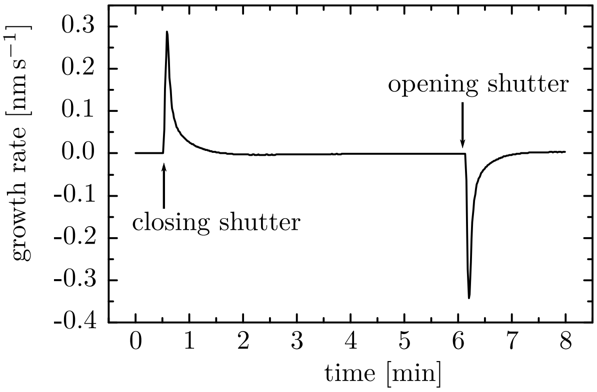

Figure 3.5: Temperature induced artifacts in QCM measurements when the quartz crystal faces the effusion cell with opened and closed shutter. The artifact's amplitudes are about two orders of magnitude higher than the evaporation rate of $0.003\,\mathrm{nm\,s^{-1}}$. After about 2 min the measurement stabilizes.

Depositing material on the crystal leads to a decrease of the resonance frequency. The change of mass of the crystal can be expressed as a function of this frequency shift. For low film thickness the relation of Sauerbrey, who published weighing of thin film by oscillating crystals first, can be applied [61]. Later, the so-called Z-match method was developed by Lu and Lewis which describes the change of mass as a function of the Z-factor, i.e. the ratio between the acoustic impedances of film and quartz [62]. This method provide accurate measurements up to a frequency shift of 40%.

The installed measuring head is a bakeable double crystal hold suited for UHV applications by *Intellimetrics*. AT-cut crystals (cut angle 35.25° to optical axis) with 6 MHz resonance frequency were applied which exhibit a shear oscillation so that the top and bottom half of it move into opposite directions. Those crystals show good temperature stability. However, temperature gradients which generate stress in the crystal lead to strong artifacts during the measurement. Such effects are observed particularly when a shutter of a hot source (effusion cell) is opened. The radiation from the source impacts the crystal surface first leading to a high temperature gradient. After a certain time the gradient is lowered after heat as dissipated through the crystal and the measurement stabilizes again. Figure 3.5 shows typical artifacts as the recorded while source shutter is opened or closed.

In most cases the measuring head is located aside from the sample. Therefore, the deposition rate is different and a correction factor called tooling factor is introduced. To determine this factor a reference measurement is required to determine the real thickness of the deposited material. Therefore, calibration samples have been grown for each single evaporator. After determining the thickness by XRR measurements the tooling factor is determined as follows

$$T = \frac{\text{deposited thickness (XRR)}}{\text{measured thickness (QCM)}} \tag{3.4}$$

3.1.4 Reflection high energy electron diffraction (RHEED)

RHEED is an electron diffraction technique used for in-situ characterization of the surface of crystalline layers and substrates inside of vacuum deposition chambers. As electrons interact heavily with surrounding gas RHEED systems are typically installed in UHV deposition chambers for MBE or pulsed laser deposition. An electron gun generates a beam of electrons which hits the surface a very small angles of less than 5°. Similar to low energy electron diffraction (LEED) the momentum perpendicular to the surface is small so that most of the electrons are reflected instead of penetrating into the sample. Electrons are diffracted by surface atoms and interfere under certain angles forming regular patterns on a phosphor screen. An advantage of RHEED is that electron gun and screen are aligned across the evaporation direction. Therefore, evaporators can be attached to the bottom of the chamber below the sample.

The electron beam that hits the surface at glancing angle is reflected almost completely and forms the specular spot on the screen which arises at the vertex of ring-shaped diffraction pattern. Reflected electron waves interfere at specific angles and form a diffraction pattern which represents the fourier transform of the probed surface, i.e. the reciprocal lattice according to the crystalline order of the surface atoms. Glancing incidence of the electrons makes them interact only with the top few atomic layers of the sample which allows to assume a 2D lattice. Thus, the reciprocal lattice consists of parallel rods perpendicular to the surface [63]. According to the Ewald construction constructive interference occurs only at scattering vectors for which Ewald's sphere intersects the reciprocal lattice. Projections of intersections onto the screen lie on circles called Laue zones which represent the order of diffraction. Figure 3.6 illustrates the pattern formation of RHEED measurements.

By means of RHEED different information can be gained about the surface symmetry of the sample, layer growth mode or even growth rate. From the spacing between diffraction maxima the lattice constant of the surface lattice can be determined. Reconstruction of the crystal surface can be observed as well as other geometrical features like

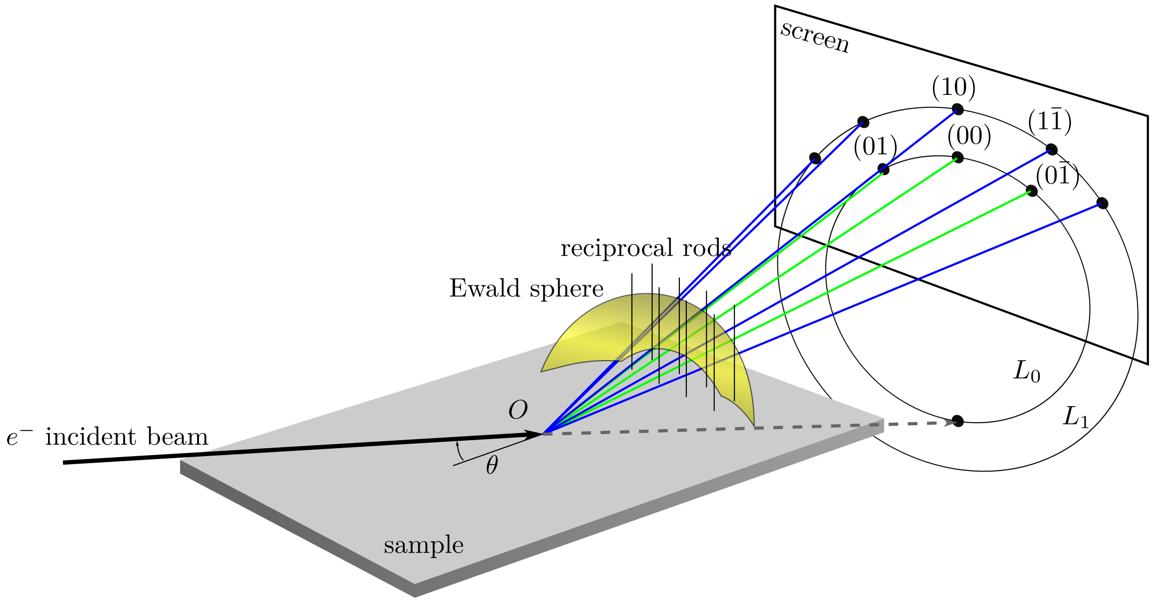

Figure 3.6: RHEED pattern formation. The reciprocal lattice degenerates to parallel rods. Diffraction maxima lie on circles on the screen. Each circle corresponds to a Laue zone L_n of n-th order.

regular steps (vicinal surfaces) as they occur on miscut substrates.

The layer growth mode can be monitored because the diffraction pattern changes to 3D transmission pattern without circular Laue zones when 2D growth goes over to island growth. This transition of the pattern comes from diffraction of the electrons which are transmitted through emerging islands.

In layer-by-layer growth the intensity of specular beam and diffracted spots can oscillate. When a layer is completely closed the intensity is high. Growth of the next layer starts with 2D islands which introduces atomic steps on the surface leading to an increase of the roughness. Therefore, the RHEED intensity drops until the coverage of the new layer has reached 0.5. The intensity rises again at higher coverage because diffraction from the new layer predominates and the roughness decreases again. Thus, one intensity oscillation corresponds to one growing layer. When a new layer starts to grow before the previous one is finished the surface roughness increases during the growth leading to a decrease of the oscillation amplitude. In contrast, the intensity remains constant in the case of step-flow growth on miscut substrates because the average number of steps remains constant.

A further possible application of RHEED in nanowire growth is the analysis of transmission patterns as they occur in 3D growth mode. If NW growth takes place selectively without any island nucleation in between, the beginning of NW growth can be determined when transmission patterns arise [64]. Similar, phase transition of the catalyst droplets can be monitored as additional diffraction spot arise from solid catalyst particles [65]. With the help of this technique VSS growth could possibly be identified in-situ by means of RHEED.

In the scope of this thesis RHEED was applied to check substrate quality mainly before and after oxide desorption. Typically, reconstruction patterns arise after desorption which is done at high temperatures (see section 3.3). Those patterns indicate an oxide free surface which is ready for epitaxial growth.

3.2 Sample preparation

Growth experiments were carried out using germanium substrates that were produced in the IKZ. Both growth of the single crystal and the wafer processing including cutting as well as chemical-mechanical polishing (CMP) were done in the institute. Thereby, the single crystals were grown from the melt by means of the Czochralski process [66].

The (100), (110) and (111) grown crystals were cut into wafers of $25 \times 25\,\mathrm{mm}^2$ with a thickness of about 600 µm. In the CMP process a surface roughness (for roughness measurements see AFM section 4.3) of typically below 1 nm is reached.

Although the surface roughness after CMP is very low a thin layer containing defects can remain at the surface in which the crystal structure may be damaged by the abrasion process which is also called sub-surface damage [67]. In order to obtain nearly perfect substrate surfaces samples undergo a wet chemical preparation which is described in detail in the following section 3.2.2.

In addition to wafers produced in IKZ germanium substrates of the same orientations as mentioned above were purchased from Semiconductor Wafer Inc., Taiwan.

Epi-ready silicon substrates which were applied for heteroepitaxial growth of germanium nanowires (see sec. 5.3.6) as well as for spin coating experiments described in section 5.6.1 were purchased from *Crystal GmbH*.

3.2.1 Chemical-Mechanical polishing

After the wafers have been cut from a single crystal, they are polished by a chemical-mechanical polishing procedure adopted from CMP recipes used for silicon to obtain a surface roughness of a few nanometers or even below one nanometer. Therefore, in the final polishing step a slurry is applied that consists of silicon dioxide colloids with an average diameter of 35 nm which are dispensed in a sodium hypochlorite (NaOCl) solution. Sodium hypochlorite oxidizes the surface homogenously while the colloids remove the oxide and therefore do not damage the germanium directly.

However, standard silicon CMP may cause minor surface damage at germanium due to the mechanical hardness compared with silicon. Thus, the quality of the surface may differ when using different polishing cloths or by applying different pressures while pressing the cloth against the sample during the polishing process. The final roughness as well as the thickness of a remaining defective surface layer can be influenced by these factors. To investigate the impact of different polishing conditions a selection of three widely used cloths has been chosen, namely Chemcloth (*Logitech Ltd*), Chemopad Perforated (*Logitech Ltd*) and Polycon (*Pieplow & Brandt GmbH*), a fully synthetic relatively long-stranded cloth which is a standard cloth for silicon CMP. The polished substrates have been investigated using AFM, EBSD and TEM in order to study roughness and surface morphology but also to clarify the existence of any sub-surface damage. The results can be found in section 5.1.1.

3.2.2 Wet-chemical preparation

As the surface properties of the used germanium wafers play a crucial role in the growth of nanowires, the substrates underwent further steps of wet-chemical preparation before insertion into the MBE chamber.

Silicon and germanium substrate preparation mostly consists of different steps involving cleaning followed by subsequent oxidation and oxide removal in order to remove any contaminations from the surface. Semiconductor surfaces tend to oxidize within a very short time in ambient air. Therefore, in a last step the freshly cleaned surface is terminated by a monoatomic layer which provides protections from further oxidation on the way to the UHV chamber.

There are standardized cleaning procedures in the literature for silicon wafer processing (*RCA SC-1* [68]). In most cleaning processes silicon oxide is formed at the surface and subsequently etched by aqueous HF or NH_4F. However, these well established cleaning methods can not be applied directly to germanium because germanium oxide is not stable (e.g. soluble in water) and thus, provides no protection for the underlying germanium. Subsequent etching cycles in aqueous acids can therefore roughen the germanium surface [69].

Hydrogen terminated surfaces can generally be obtained by applying HF. However, there is general agreement that H-terminated germanium surfaces do not possess the stability that is known for H−Si surfaces. Alternatively, halogen termination can be obtained in vacuum [70] or in solutions. Especially, the chlorine and bromine termination have been studied extensively on Ge [71]. Roughness evolution due to etching cycles and carbon contamination level have been studied by photoelectron spectroscopy by Sun et al. [72].

In the scope of this thesis mainly the chlorine termination was applied as it is sufficiently stable while samples are transferred to the load lock of the UHV cluster (see section 3.1). Other terminations such as bromine or sulfide termination were applied to investigate the influence on in-plane growing nanowires which is described in detail in section 5.4.

Germanium substrates

Cleaning solutions were applied at room temperature unless otherwise stated. All samples in the wet-chemical treatment underwent an initial cleaning step with 1:1 mixture of acetone ($(CH_3)_2CO$) and isopropanol (C_3H_8O) in an ultrasonic bath. After rinsing the samples in deionized water (DIW) an oxidation and oxide removal step was applied repeatedly [73, 74]:

chemicals	mix ratio	time
$HCl : H_2O$	1 : 4	30 s
$H_2O_2 : NH_4OH : H_2O$	1 : 1 : 4	30 s

Table 3.1: Wet-chemical Oxidation and oxide removal on Ge substrates. The process was repeated twice.

In the next step the surface is terminated by one of the chemical treatments that are listed in table 3.2. Contrary to hydride passivation, the passivation with HCl or HBr leads a monoatomic layer of the halogens [75] which can be explained by a scheme of the passivation process that is depicted in figure 3.7. Also in the hydrogen termination process a fluoride terminated surface is formed temporarily in an intermediate state which is unstable and finally converted into hydride terminated surface [68]. This behavior can be explained by different degrees of dissociation α which is defined according to the reaction $HA + H_2O \rightleftharpoons H_3O^+ + A^-$

$$\alpha = \frac{[A^-]}{c_0} \tag{3.5}$$

α gives the fraction of acid molecules that are ionized by splitting off a proton (H^+) where c_0 is the initial concentration of undissociated molecules. While HCl and HBr are almost completely dissociated HF shows a very low degree of dissociation (see table 3.3). Lots of undissociated HF molecules are present in the solution and can thus transform the fluoride termination into a hydride one.

passivation type	chemicals	mix ratio	time
Hydride:	$HF : H_2O$	1 : 4	20 s
Chloride:	$HCl : H_2O$	1 : 4	10 min
Bromide:	$HBr : H_2O$	1 : 4	6 min
Sulfide:	$HF : H_2O$	1 : 4	20 s
	$(NH_4)_2S : H_2O$	1 : 5	20 min at 80 °C

Table 3.2: Different treatments for the termination of germanium substrates from aqueous solutions. The stability of the passivating layer increases from hydride to sulfide termination.

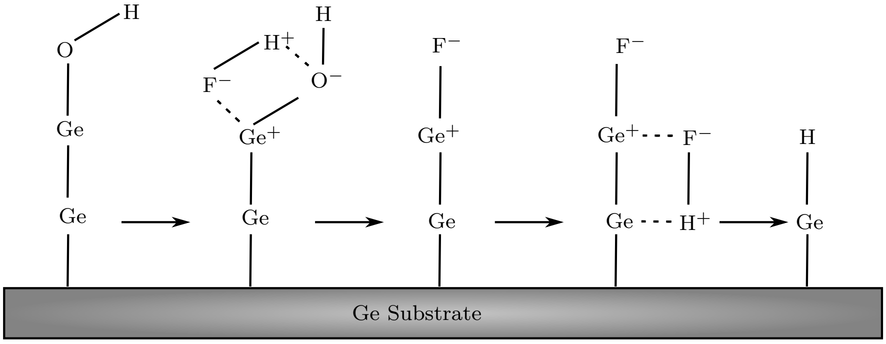

Figure 3.7: Hydrogen passivation scheme explaining the process during surface reaction of oxidized germanium and hydrofluoric acid analog to silicon [68, pp. 543]. As an intermediate state a fluoride termination is formed which is eventually transformed into an hydride termination while germanium fluoride is formed.

hydrohalic acid	α
HF	0.07
HCl	0.876
HBr	0.899

Table 3.3: Degree of dissociation of applied acids [76]

The stability of halogen surface passivation layers mainly depends on reoxidation by H_2O in ambient air. Research on those passivation layers revealed increasing stability

passivation	χ	$\chi - \chi_{Ge}$	r_{VdW} [pm]
hydride	2.20	0.19	120
fluoride	4.00	1.99	147
chloride	3.16	1.15	175
bromide	2.96	0.95	185
sulfide	2.58	0.57	180
oxide	3.44	1.43	152

Table 3.4: List of Pauling electronegativities and Van der Waals radii of passivating elements on a germanium surface. The polarization is represented by the difference of electronegativities ($\chi_{Ge} = 2.01$).

with higher atomic number which is ascribed to different factors. The first factor is electronegativity χ of the passivating halogen atoms which decreases with higher atomic numbers. High electronegativity causes stronger polarization of the bonds between halogen atoms and the underlying substrate atoms which facilitates attack by also polarized water molecules leading to disintegration of the passivating layer and oxidation of underlying germanium. The same mechanism initiates the transformation of a fluoride termination into hydride termination as it is described above.

The second factor is called steric factor which is a geometrical argument referring to the size of the passivating atoms. The assumption is that larger passivating atoms make it more difficult for H_2O to attack the polarized Ge atom [71, p. 63]. The size of atoms can be given by Van der Waals' radius which also increases with higher atomic number. Therefore, bromide passivation is assumed to provide the highest stability among halogen passivations. Both, electronegativity and Van der Waals radius of the applied passivating atoms are listed in table 3.4.

The stability of sulfide passivation can be explained because sulfidation closely resembles oxidation of germanium which exhibits so-called bridge bonds Ge−S−Ge [77] and therefore, also sulfide passivation layer can be desorbed in the temperature range from 460 K and 750 K according to Anderson et al..

After passivating the substrate surface the samples are dried in flowing nitrogen and inserted into the MBE chamber.

Silicon substrates

Silicon substrates of epi-ready grade were purchased from *Crystal GmbH* and were cleaned similar to germanium wet-chemical preparation before they are being inserted into the UHV system.

The substrates are cleaned in a 1:1 mixture of acetone ($(CH_3)_2CO$) and isopropanol (C_3H_8O) in an ultrasonic bath for 10 min followed by a rinse in deionized water. Subsequently, *RCA standard clean 1* (SC-1) treatment was applied which is described in the following [68]. The SC-1 solution consists of H_2O_2, NH_4OH and deionized water at a mix ratio of 1:1:4. The solution is headed up to 80 °C before the sample is immersed for 10 min. Afterwards, the substrates are rinsed in deionized water for 5 min. While mainly organic contaminants are removed due to the solvating action of NH_4OH and the oxidizing action of the alkaline H_2O_2. In addition, the native oxide is removed slowly while reoxidation of underlying silicon takes place at approximated the same rate. This oxide regeneration is believed to remove particles and impurities effectively.

Finally, the substrates are HF dipped to remove silicon oxide from the surface and to protect the bare silicon with hydrogen termination.

3.3 Growth process

In the frame of this thesis germanium nanowires were grown via the VLS mechanism (see sec. 2.1) using gold as metal droplet onto germanium substrates. Diameter and areal density are widely given by the arrangement of the droplets. Thus, droplet formation is one of the key aspects in nanowire growth. Nanowire growth itself is initiated subsequently by providing Ge as molecular beam from a high temperature effusion cell. In the following section the experimental details of the growth process are described.

After wet-chemical preparation, the samples were immediately inserted into the load lock. After pump down the sample holder is transferred into the MBE chamber where the process starts with an oxide desorption step to remove residual surface oxide that may have remained from the wet-chemical treatment. Germanium oxide can be desorbed under UHV conditions at temperatures above 400 °C [73]. Therefore, substrates were annealed at 700 °C for 30 min prior to gold deposition. Silicon oxide is more stable than germanium oxide and requires temperatures as high as 900 °C to desorb. Silicon substrate are therefore annealed at 900 °C for 1 h.

3.3.1 Droplet formation

After surface oxide desorption gold is evaporated in order to form droplets which determine the places where VLS growth is initiated. Droplet formation has been discussed theoretically in section 2.4.1. As a result, it follows from equation (2.29) that the size of critical nuclei decreases at higher supersaturation. Thus, at higher evaporation rates leading to higher supersaturation it is more likely for atoms to form another droplet instead of joining an already existing one. Thus, the droplet density can be directly influenced by deposition rate. Another important parameter for the arrangement of droplets is the substrate temperature which influences surface diffusivity of gold atoms. According to the Arrhenius equation (eqn. (2.33) the diffusivity increases with temperature. Therefore, at high temperatures gold atoms can diffuse along the substrate for longer time which results in larger droplets because it is more likely for an adatom to find an already existing droplet instead of undergoing any nucleation process. Therefore, droplet size can be reduced by lower temperatures. While droplets form on the substrate they begin to dissolve material from the substrate until the equilibrium concentration of germanium in the droplet is reached. Depending on the substrate temperature more the 28 at.% germanium can be dissolved in the droplets according to the Au-Ge phase diagram.

Typically, 1 nm of gold has been deposited at a rate of $0.017\,\mathrm{nm\,s^{-1}}$ and at a substrate temperature of 430 °C. In order to reduce the diameter and to change the areal density of the droplets either temperature or deposition rate have been varied.

3.3.2 Nanowire growth

After gold droplets have formed germanium deposition was started to initiate nanowire growth. According to Au-Ge phase diagram nanowire growth by VLS mechanism is expected at temperatures higher than eutectic temperature of $T_e = 361\,°\mathrm{C}$. Therefore, the substrate temperature was varied to find appropriate growth conditions and to investigate the influence on the average growth rate.

Furthermore, growth was interrupted after different time spans to investigate time evolution of growing nanowires and to determine any incubation time between the beginning of germanium deposition and the beginning of nanowire growth.

The other experimental parameter during the growth is germanium deposition rate which may influence the supersaturation inside the catalyst droplets. Therefore, the deposition rate was varied to investigate the influence on the growth.

3.4 Spin Coating

Embedding can play an important role in further processing of grown nanowires in terms of contacting from the top, insulating against each other or stabilization of those structures with high aspect ratios. Therefore, spin coating was chosen as a cheap process, easy to handle while it is still applicable in nanotechnology.

Nanowires are promising structures for optoelectronics, thermoelectrics or even lithium-ion batteries. However, encapsulation of nanowires is a prerequisite in order to contact nanowires from the top. The encapsulation should provide some general characteristics. The nanowires should be insulated to maintain the performance of each single nanowire. Furthermore the filling material should be transparent to meet the specific optoelectronic demands. There are further properties which can be of importance especially for electronic applications. The big surface-to-volume ratio of nanowires could lower the performance of any nanowire device due to many surface states which may act as recombination centers. Therefore, an appropriate filling material should also be able to form a good interface with the nanowire to reduce surface recombination.

Among different techniques to fill the gaps in between nanowires one of the cheapest and quickest is spin coating. Spin coating is known particularly from semiconductor industry to coat wafers with a thin layer of photo resist.

In the frame of this work, hydrogen silsesquioxane (HSQ) was chosen to encapsulate the nanowires. HSQ is a polymer containing no carbon and is known as an electron-beam resist which provides very good contrast allowing the creation of structures of dimensions down to 10 nm [78]. HSQ has a cage-like Si−O−Si structure. The cage transforms into a net-like structure similar to silicon oxide by curing or oxygen plasma treatment [79]. Figure 3.8 shows the cage and the net configurations. During the curing process Si−H bonds are broken and hydrogen is released which leads more and more to SiO_2 stoichiometry.

HSQ layers have been prepared by means of spin coating with a *WS-650 MZ-23NPP* from Laurell Technologies. *FOx-14* HSQ spin on solution called flowable oxide with a kinematic viscosity of 0.6 cSt was purchased from *Dow Corning*. Different rotation speeds have been tested to prepare different layers with different thicknesses.

After coating the samples undergo a so-called soft bake on a hot plate at about 220 °C to evaporate residual solvent. Additionally, HSQ starts to flow and develops very good gap-filling capability during the soft bake. In the next step samples are cured thermally to transform HSQ into net structure. This so-called hard bake was done under nitrogen atmosphere at varying temperatures up to 700 °C.

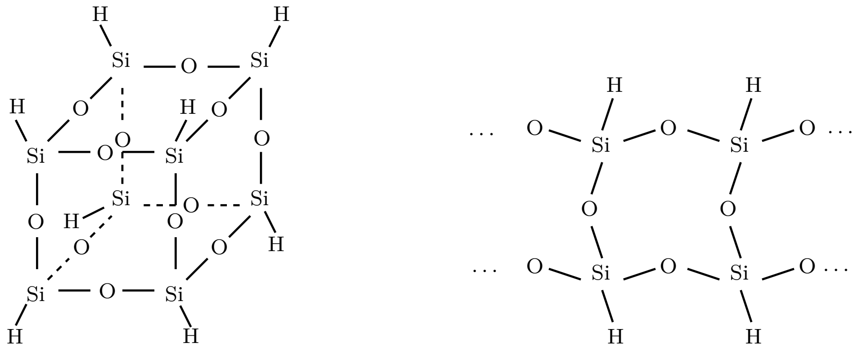

Figure 3.8: Known structures of HSQ. (a) cage structure which transforms into (b) net structure upon curing or oxygen plasma treatment. Figure from [79]

The change in the structure has been investigated by means of fourier transform infrared spectroscopy (FTIR), e.g. to determine the cleavage of typical cage-like bonds like $O_3Si{-}H$. Table 3.5 gives an overview of the characteristic vibrational modes which can be detected by FTIR.

vibration mode	cage structure [cm^{-1}]	net structure [cm^{-1}]
$\nu(O_3Si{-}H)$ stretching	2250-2260	—
$\nu(Si{-}O{-}Si)$ stretching	1130	1070
$\nu(H{-}SiO)$ bending	860, 890	830

Table 3.5: Detectable vibrational modes in FTIR. Values can be found in [79]

4 Characterization Methods

Samples were characterized by a variety of different methods including microscopical, X-ray and optical techniques including scanning electron microscopy to characterize surface morphology of grown structures, energy dispersive X-ray spectroscopy for elemental analysis, transmission electron microscopy for detailed analysis of the crystal structure on an atomic scale in selected areas, atomic force microscopy to image the surface topography and determine the surface roughness of substrates as well as buffer layers, X-ray reflectometry for measurement of the thickness of deposited layers. Additionally ellipsometry and fourier transform infrared spectroscopy were applied to measure layer thickness or optical parameters respectively.

4.1 Scanning electron microscopy (SEM)

Typically, nanowires and nanostructures have dimensions smaller than the resolution of conventional optical microscopes which is limited by Abbe's well known diffraction limit of roughly half of the applied wavelength [80].

Therefore, characterization of processed samples by means of SEM was carried out at a regular basis. A sample is imaged by raster scanning it with a focused electron beam. Electrons are generated from filament emitters or field emitters. The latter provide lower energy spread and larger emission current density [81]. The purpose of the electron optics is to demagnify the beam cross section to form an electron probe at the surface of specimen. Thereby, electrons are accelerated to their primary energy by a voltage difference of several kV between cathode and anode. The resolution of an SEM can reach values below 10 nm and is basically determined by the final cross section of the electron probe. Figure 4.1 shows a schematic setup of an SEM.

Electrons hitting the surface interact with the atoms and generate different kinds of signals, involving low energy electrons (secondary electrons), high energy electrons (mainly back-scattered electrons) and X-rays, that contain information about the surface topography, crystallography or composition.

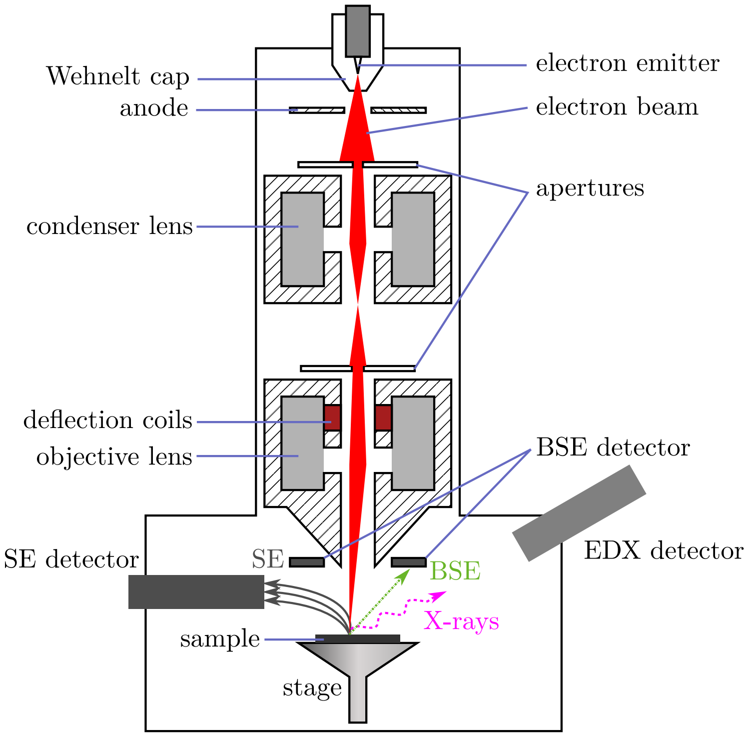

Figure 4.1: Principle of a scanning electron microscope. SE - secondary electrons, BSE - backscattered electrons, EDX - energy dispersive X-ray detector.

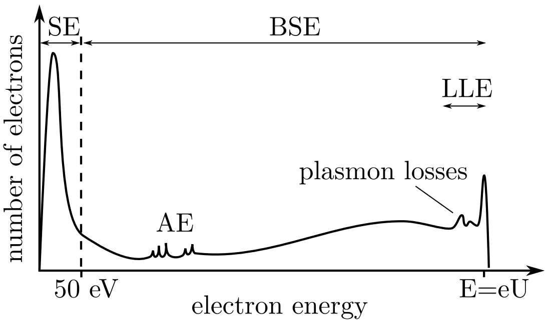

Figure 4.2: Schematic energy spectrum of emitted electrons involving secondary electrons (SE) with $E_{SE} < 50\,\mathrm{eV}$, backscattered electrons with $E_{BSE} > 50\,\mathrm{eV}$ and Auger electrons (AE) between 50 eV and 2 keV (diagram according to fig. 1.5 in ref. [81]). High energetic electrons which undergo direct reflection at the sample are also called low loss electrons (LLE).

SEM investigations presented in this theses were carried out with a Nova 600 Nanolab DualBeam from FEI company. It is combination of an SEM with a focused ion beam gun (FIB). The electron gun is equipped with a Schottky field emitter and provides accelerating voltages from 200 V to 30 kV. The FIB gun works with a gallium liquid metal source. Probe currents from 1 pA to 20 nA are available at accelerating voltages from 5-30 kV. In addition several gas injection sources are available for deposition or etching purposes. For sample manipulation a 5-axis motorized stage with a minimum step size of 100 nm is installed. Furthermore, the system is equipped with an energy dispersive X-ray detector as well as a phosphor screen for EBSD pattern recording.

4.1.1 Secondary electrons (SE)

The SE mode is most important to investigate the surface morphology of the samples. The spectrum of emitted electrons involves secondary electrons at energies lower than 50 eV (most probable at 2-5 eV) and backscattered electrons (BSE) at high energies with an elastic peak at the primary energy (see fig. 4.2). SE are generated by inelastic collisions to such high energy levels that the excited electrons can overcome the work function and exit the material. The low exit depth of SE of a few nanometers leads to small information volumes and allows resolutions between 1 nm and 10 nm to be reached. SE have low exit energies and can effectively be collected by means of a positively biased collector grid in connection with a scintillator-photomultiplier combination, often called Everhart-Thornley detector [82].

Different contrast mechanisms can be identified in SEM micrographs. The SE yield depends on the tilt angle of the specific surface element where surfaces tilted towards the detector appear brighter. Furthermore the yield increases at small particles or edges making them to appear lighter than the surrounding area. Biased areas of the specimen can repel or retard the SE which leads to voltage contrast where negatively biased areas appear bright and positively biased areas dark. SE are also generated by backscattered electrons that have passed through the material and back towards the surface. Typically, BSE contrast is therefore superimposed on every SE micrograph [81].

4.1.2 Backscattered electrons (BSE)

In contrary to SE, BSE have high energies, move on straight trajectories and are therefore not affected by electrostatic collection fields. BSE with the highest energies, often called low loss electrons (LLE, see fig. 4.2), are mainly scattered into a small solid angle and are often detected by through lens detector (TLD) or separate detectors mounted elsewhere near the pole piece of the electron optics.

The most important contrast mechanism of BSE is the dependence of the backscattering coefficient on the mean atomic number Z, which allows domains with different values of Z to be recognized. Heavy elements with a high Z have higher backscatter coefficients and appear brighter in the SEM image. The backscatter coefficient also depends on the orientation of the lattice planes of crystalline samples relative to the electron beam since channeling effects lead to anomalous absorption or transmission. This so called channeling contrast can be used to image grains in polycrystalline material by rocking the electron beam over the sample or the sample relative to the beam respectively.

4.1.3 Energy-dispersive X-ray spectroscopy (EDX)

Energy-dispersive X-ray spectroscopy is a characterization method to analyze elemental composition of the specimen. X-rays, excited by the high energetic electrons in an SEM, are detected to analyze the chemical composition of volumetric regions near the surface of the sample. This technique provides qualitative and quantitative analysis of contained elements.

Atoms in the material are ionized by interacting with the incident electron beam. The impinging electrons are scattered at the atomic electrons that can be excited and ejected from their shell. If the energy of incident electrons is high enough core energy levels can be ionized. Electrons from upper energy levels filling the vacancy release energy that is converted to an characteristic X-ray quantum or the energy may be transferred to another electron that leaves the sample as an Auger electron. Both X-ray energy and kinetic energy of the Auger electron are determined by the difference of the energy levels between vacant and higher-energy shell. The X-ray generation is depicted in figure 4.3.

The energy of emitted X-rays is characteristic for each element and can be classified in series according to the shell in which the electron hole was created, e.g. K shell. The second label is a Greek letter denoting the upper shell from which the electron originates that fills the vacancy. For L shells and higher the spin-orbit coupling leads to a splitting of energy levels denoted as an arabic subscript number, e.g. Lα_1.

The energy of X-ray quanta is measured by an Si(Li)-detector [81] that is operated at liquid nitrogen temperature. X-rays striking the detector are absorbed by photoelectric effect and electron-hole pairs are created. Thus, the X-ray energy is directly proportional to the number of electron-hole pairs resulting in a certain pulse height of the collected charge in the detector. The energy resolution of such detectors is typically in the range

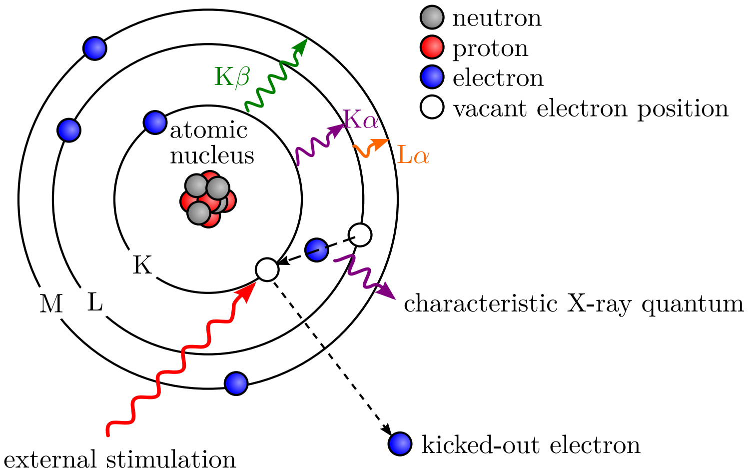

Figure 4.3: X-ray generation due to core level ionization. The energy of the emitted X-ray quantum is characteristic for the element.

of 120-140 eV.

The lateral resolution is limited by the penetration depth of the electron beam in the specimen. Incoming electrons are scattered inside the material and excite X-rays in a volume of a few micrometers in diameter. Electrons reaching the EDX detector also create electron-hole pairs and thus generate additional background signal in the spectra. Therefore, EDX measurements in this work were done using the collecting field of the Everhart-Thornley detector to reduce background generated by electrons.

The EDX detector with an energy resolution of 129 eV is part of the EDAX "Trident" system including EDX, EBSD and WDS and is attached to the FEI Nova 600 Nanolab SEM. Data collection and analysis were done with Genesis X-ray microanalysis software from EDAX Inc.

4.1.4 Electron backscattered diffraction (EBSD)

In EBSD the electron beam is used to analyze the crystallography of the specimen. The advantage of this method is that no rocking of either the sample or the incident beam is necessary. Therefore, the spatial resolution is only limited by the electron probe diameter.

The sample is tilted by 70° and the EBSD detector (phosphor screen with CCD camera) is mounted at 100° relative to the incident beam. A fraction of incident electrons are scattered inelastically by atoms in the material to form a divergent source of electrons close to the surface of the sample. These electrons partly incident lattice planes at angles

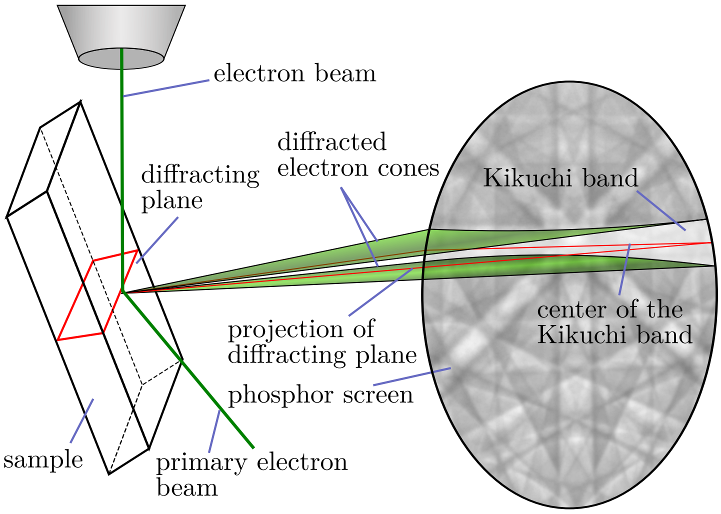

Figure 4.4: Schematic of the image formation in EBSD. High electron energy leads to large cone angles of the diffracted electrons. Thus, indicated cone sections approximate to straight lines in SEM. The center of each Kikuchi band corresponds to the projection of the diffracting lattice planes.

that satisfy the Bragg equation

$$n\lambda = 2d_{hkl}\sin(\theta) \tag{4.1}$$

where n is an integer, λ is the electron wavelength, d_{hkl} is the lattice plane spacing and θ is the angle of incidence of the electron on the diffracting plane. These electrons are diffracted to form a pair of cones (Kossel cones) with large aperture angels whose axes are perpendicular to the diffracting lattice plane leading to a characteristic diffraction pattern. Imaging these patterns on a phosphor screen results in so called Kikuchi bands of increases electron intensity in the region between the cones (see fig. 4.4). The center of Kikuchi bands correspond to the projection of the diffracting planes on the phosphor screen. Hence, each band can be indexed by Miller indices of the diffracting plane which has formed the Kossel cones.

The intensity of Kikuchi bands is sensitive to crystalline perfection of the sample, structural defects or impurities. Therefore the contrast in EBSD patterns can be exploited to observe the quality of the surface of specimen. In the frame of this thesis this technique has been applied to check the surface quality of substrates made in IKZ. Therefore a reference sample was created depositing an almost perfect germanium layer homoepitaxially on Ge(111) and a spot with destroyed, scratched surface for background measurement. Both, reference sample and the IKZ-made substrate were attached to the

45° tilted sample holder. By tilting the holder for another 25° the desired 70° incident angle could be reached. A high quality region of the reference sample was chosen to focus the EBSD pattern. Setting this as the reference measurement, the same procedure was carried out for the scratched region with destroyed surface. The result was set as background to be deduced from the measurements. Eventually the substrate under investigation was analyzed.

The EBSD is part of the EDAX "‘Trident"’ system including EDX, EBSD and WDS and is attached to the FEI Nova 600 Nanolab SEM. Data collection and analysis were done with OIM^{TM} 5.31 Software from EDAX Inc.

4.2 Transmission Electron Microscopy (TEM)

The basic functionality of a transmission electron microscope (TEM) is analog to optical microscopes. In standard TEM the electron beam is not focussed on a single spot on the specimen, but illuminates a larger area. The transmitted electron wave is recorded with a phosphor screen or CCD detector. Electrons strongly interact with matter of the specimen. Therefore the samples have to be extremely thin in order to provide good electron transparency.

The resolution of such microscopes is basically limited by the wavelength λ of the incident wave according to Abbe's diffraction limit [83]

$$\Delta x = \frac{\lambda}{2n\sin(\alpha)} \tag{4.2}$$

where n is the refractive index and α is the half aperture angle of the objective lens. According to de Broglie, the wavelength of matter waves is given by

$$\lambda = \frac{h}{p} \tag{4.3}$$

where h is the Planck constant and p the momentum of the particle. Thus, the wavelength can be drastically decreased using particles with a high momentum. In TEM electrons are accelerated using high voltages to relativistic energies for which the wavelength can be written as

$$\lambda = \frac{hc}{\sqrt{2m_0c^2eU + e^2U^2}} \tag{4.4}$$

where c is the speed of light, e is the elementary charge, m_0 is the electron mass and U the accelerating voltage. Owing to the small de Broglie wavelength of electrons with high kinetic energy ($\lambda_e = 1.97 \times 10^{-12}\,\mathrm{m}$ at 300 keV) the resolution of a TEM can be much higher compared to optical microscopes.

However, the resolution that can be achieved in TEM is lowered by optical aberrations, especially spherical aberration, limiting the maximum aperture angle of the objective lens. Aberration correctors can be used to reduce these optical aberrations and therefore increase image quality and resolutions significantly.

TEM offers a variety of different operation modes and contrast mechanisms. Incoming electrons are scattered in the specimen. The scattering cross-section is larger for elements with higher atomic number but also increases with the sample thickness. This contrast is called mass-thickness contrast. For crystalline specimens electrons are diffracted depending on the sample orientation according to Bragg's law (equation 4.1). In this case the contrast is called diffraction contrast.

Images can be recorded in bright field mode by selecting the non-scattered beam using an objective aperture. In dark field mode electrons are selected that are scattered into a specific direction (Bragg reflected beam) [84]. In this way specimen areas appear bright that contribute to the selected Bragg-diffraction spot.

Another contrast mechanism is called phase contrast or high-resolution TEM (HRTEM) respectively. Diffracted electron waves pass the sample with no energy loss but are phase shifted. A contrast pattern is formed in the image plain by interference of the diffracted wave and the direct electron wave. This pattern is in direct relation with the crystal structure of the sample and represents a projection of the lattice planes. Resolutions below 1 Å can be achieved in this way.

Similar to SEM, the illumination of samples with high energetic electrons of low energy spread provides techniques to analyze the crystal structure of the sample. There is a variety of electron-diffraction modes in TEM in which the so-called selective area electron diffraction is the most common technique [84]. Diffraction patterns of the specimen can be recorded by adjusting the objective lenses such that the back focal plane can be imaged. These patterns show typically diffraction spots for crystalline samples depending on lattice spacing, symmetry and orientation of the specimen relative to the beam path. In the case of polycrystalline or amorphous samples the image consists of a series of rings.

A further mode of operation in TEM is scanning transmission electron microscopy (STEM). The electron beam is focused on the sample to form a small electron probe that is raster scanned to form an image. Transmitted electrons are collected using current detectors, e.g. Faraday cup, and correlated with the position of the scanning beam to form an image. The raster scanning makes STEM suitable for analytical techniques like mapping by EDX.

TEM investigations presented in this thesis were conducted using a *FEI Titan 80-300 (S)TEM* which offers accelerating voltages from 80 to 300 kV and provides a lateral resolution better than 1 Å in phase contrast mode by means of an aberration corrector in the objective-lens. Additionally, elemental mappings in STEM mode have been made using a *JEOL JEM 2200FS* equipped with a *BRUKER XFlash 5030T* EDX detector.

4.2.1 Conventional sample preparation

In order to obtain good electron transparency samples have to be extremely thin in the range of several tens of nanometers. Samples must be prepared carefully in a multi-step process consisting of sawing and different polishing techniques as describes in the following paragraphs.

Conventional preparation of samples for TEM is based on cutting the desired areas from the sample, agglutinating them, polishing the resulting block to approximately 10 to 15 µm thickness, and finally using ion milling to create a small hole at the glue line, around which the specimen is transparent for electrons and the thickness is just a few nanometers. This area can be observed by TEM.

For the investigation of the germanium nanowires, stripes from two different areas were cut from the sample with a diamond wire saw. These stripes were agglutinated with a two-component adhesive and then cut again, so as to fit them into specially designed titanium rings.

Mounted on a small glass cylinder in a tripod, the sample is polished with a series of diamond abrasive films with decreasing grain sizes. After the desired surface quality has been achieved, the sample is detached from the glass cylinder, a stabilization ring is attached to the polished surface and the sample is mounted upside down on the glass cylinder again. The entire polishing process is repeated for the second side until a total sample thickness of 15 µm is reached. Each grain size may abrade approximately double the thickness of the previous grain size to remove not only the crystal defects from cutting but also those caused by the polishing itself. For this purpose the polishing follows the polishing scheme in table 4.1.

For the final ion milling step the sample is inserted into a special sample holder allowing the Ar^+ ions to reach the sample from both sides. After insertion into and evacuation of the chamber, two ion guns are milling the sample with 4 keV argon ions at an incident angle of 4° from each side. After a small hole becomes visible at the glue line, lower energies at higher angles are used to remove the damaged, amorphized layer from the

thickness [µm]	grain size [µm]
100	30
70	15
50	9
35	6
25	3
15	1
15	0.1

Table 4.1: Polishing scheme for conventional TEM sample preparation: with each grain size approximately double the thickness of the previous grain size is abraded.

surface, before the sample can eventually be extracted and used for TEM.

4.2.2 Lamella preparation by focused ion beam (FIB)

Alternatively, TEM samples have been prepared by cutting thin lamella using the focused ion beam (FIB) technique. Sample preparation by means of FIB is especially suited if the target area is too small for conventional preparation, for example in case of a specific nanowire together with the underlying substrate. The cross-sectional lamella which is centered around the target area is cut from the sample and attached to a transport grid which can be directly inserted in to the TEM. The preparation was carried out using a dual beam FEI Nova 600 Nanolab. A dual beam system allows in-situ imaging of the area of interest while processing the sample with the focused ion beam providing good control of the FIB process. Further details of the system are described in section 4.1.

The lamella is aligned with a $\langle 112\rangle$ direction of the substrate such that the viewing direction in TEM is along a [011] zone axis. In the first step of the process the selected area is covered with a protective Pt layer. For Pt deposition a platinum precursor is injected and cracked by the ion beam or the electron beam. The region is marked by two deep cross-shaped cuts which help to position the target area during the automated FIB processing (see fig. 4.5). After cutting wedges on both sides of the target area a several hundred nanometer thick lamella remains the center. To keep the damage caused by ion bombardment as low as possible further thinning is done at low ion currents of a few pA. Finally, a TEM window of 80 nm thickness is thinned in the center of the lamella.

In order to transfer the lamella to the TEM copper grid it has to be released from the substrate before. Therefore, a U-shaped cut is placed at the lower part of the lamella which is then carried by remaining connection points (see fig. 4.6). The latter are cut after the tip of a micromanipulator (by Kleindiek Nanotechnik) is attached to the lamella and eventually the lamella can be lifted off the substrate.

The lamella is then transferred with the help of the micromanipulator to the TEM copper grid and is attached to it by Pt deposition (see fig. 4.7). After cutting the connection between lamella and tip the micromanipulator can be retracted. The copper grid can be directly placed into a TEM sample holder.

Compared to conventionally prepared TEM samples FIB-cut lamellas have lower quality as the are too thick for high resolution TEM and are often bended which makes it difficult to orientate the specimen relative to the electron beam.

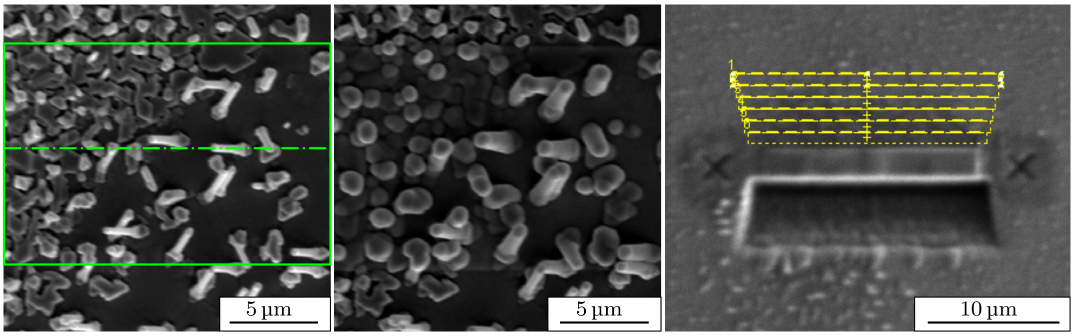

(a) **(b)** **(c)**

Figure 4.5: The series of SEM micrographs shows subsequent steps of FIB lamella preparation. (a) Selected area (green box) with nanowire aligned with the center line of the later lamella. (b) Same area as on the left after Pt protective coverage. (c) crosses mark the center of the lamella. Slice-wise cutting of wedges on both sides of the target area indicated by yellow boxes.

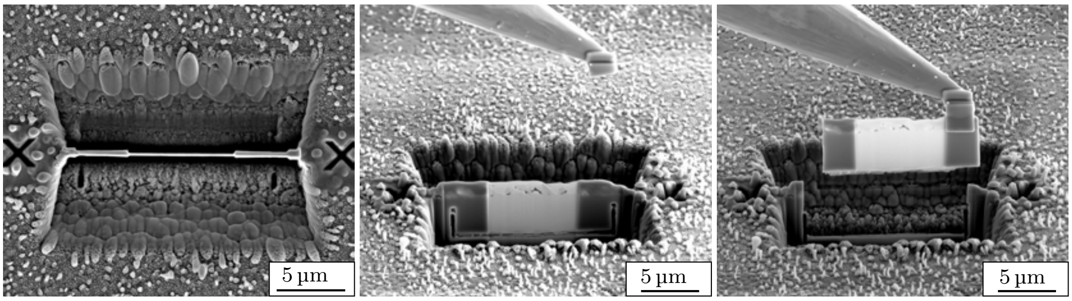

(a) **(b)** **(c)**

Figure 4.6: Series of SEM micrographs showing the takeout process of the FIB lamella. (a) topview of a completely thinned lamella with TEM window of 80 nm thickness in the center. (b) Titled view of the lamella. The U-cut can clearly be seen. The tip of the micromanipulator approaches the lamella from the top. (c) lamella attached to the micromanipulator by Pt deposition. Contact points on the left and right of the lamella were cut.

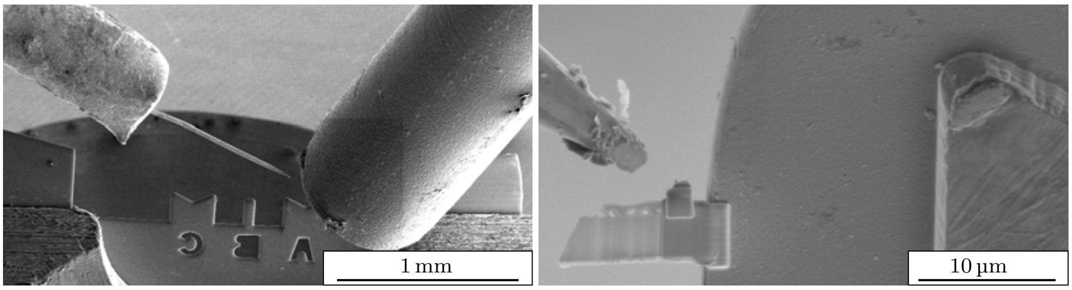

(a) **(b)**

Figure 4.7: Attaching the FIB lamella to a copper TEM grid. (a) Overview showing micromanipulator and Pt injector in front of the copper grid. (b) successfully attached lamella and retreating micromanipulator.

4.3 Atomic Force Microscopy (AFM)

AFM is a scanning probe microscopy technique and was invented by Binnig, Quate and Gerber in 1986 [85]. In contrast to its predecessor, the scanning tunneling microscope (STM) , AFM does not require conductive samples since the forces between a nanoscopic tip and the surface atoms of the sample are used as basic interaction for imaging during raster scanning across the sample. The tip is attached to a cantilever which is typically 35 µm wide and 125 µm long. The force between sample and tip leads to a bending of the cantilever which can be optically detected. By controlling the tip-sample-distance such that the cantilever bending is kept constant the surface topography of the sample can be imaged. This constant force mode is also called contact mode. It is depicted schematically in figure 4.8. This mode operates in the repulsive regime of the force-distance relation which can be well described by a 12-6-Lennard-Jones potential shown in figure 4.8b. The attractive potential (blue branch) is mainly caused by Van der Waals forces whereas the repulsive potential (red branch) comes from overlapping orbitals of tip and sample surface.

There are further modes of operation, called non-contact mode and tapping mode (also semi-contact mode), working dynamically by letting the cantilever oscillate near the resonance frequency. In these modes the amplitude of the cantilever oscillation is influenced by the forces between tip and sample and is thus a function of the distance between tip and sample and serves as control parameter to track the surface topography of the sample.

In tapping mode the tip is approached to the surface until it taps the sample slightly which leads to a damping of the oscillation. Due to the short period of contact between

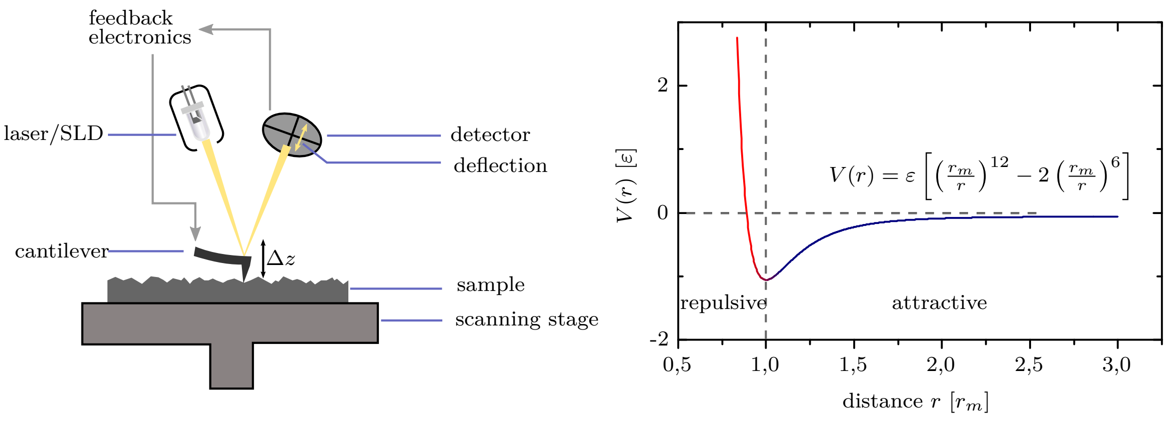

(a) **(b)**

Figure 4.8: (a) Schematic image of an AFM. The cantilever bending is optically detected by reflecting light from a laser or a superluminescent diode (SLD) from the cantilever backside onto a four quadrant photodiode. The deflection and thus the force between sample and tip is kept constant by feedback electronic (PID controller). (b) 12-6 Lennard-Jones potential. r_m is the distance according to the minimum of the potential and ε is the depth of the minimum. The red branch indicates the repulsive potential whereas the blue branch indicates the long range attractive van der Waals potential.

tip and sample, compared to contact mode, less lateral forces occur that can influence the measurement or even lead to artifacts.

There are also artifacts caused by the measuring system of an AFM. For instance, very steep slopes are difficult to image because the feedback loop can overreact which leads to so called z edge overshoot. This can be widely avoided by adjusting the PID parameter or by reducing the scanning speed of the tip. There are other feedback induced artifacts that are not in the scope of this thesis but can be found elsewhere [86].

Furthermore, there are artifacts caused by the geometry of the tip or the angle between the probe and the surface. Every AFM image can be understood as a convolution of the sample surface $f(x, y)$ and the tip geometry $g(x, y)$.

$$(f * g)(x, y) = \int_{-\infty}^{\infty} \int_{-\infty}^{\infty} f(t_1, t_2) g(x - t_1, y - t_2)\, dt_1\, dt_2 \tag{4.5}$$

Thus, the ideal tip would be delta shaped ($g(x, y) = \delta(x)\delta(y)$) which results in the real sample surface $f(x, y)$ after deconvolution. This mechanism for image formation leads to broadened imaging, especially of small features on the surface. Figure 4.9 shows a simulation of an artificial surface geometry of hemispheres scanned with a standard tip as it was used in the frame of this work. This example serves as a model for AFM images of gold droplets as they are formed during the growth process (see 2.1). In order to measure the true droplet diameter the topography images have to be corrected by a deconvolution with the tip geometry given in figure 4.9b.

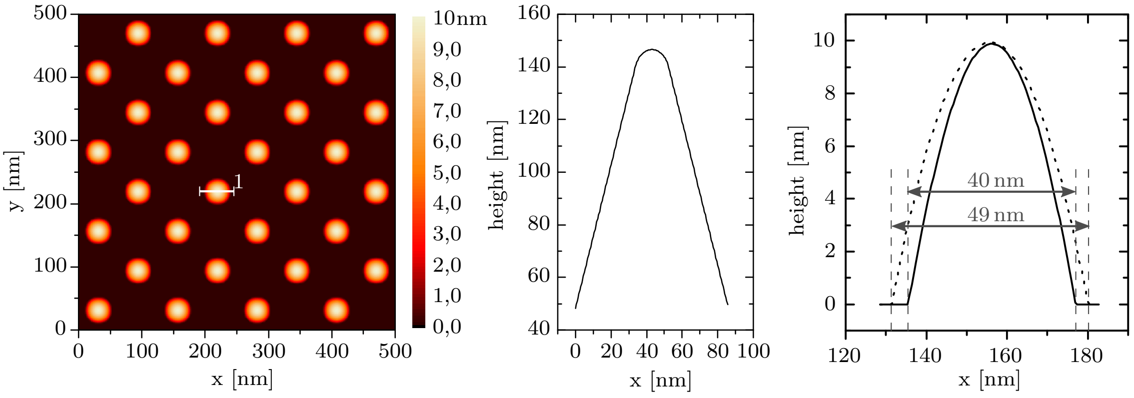

(a) **(b)** **(c)**

Figure 4.9: (a) Artificial Topography of hemispheres of 10 nm height and 40 nm diameter used as input data for convolution with a modeled tip. (b) Profile of the modeled tip data with 10 nm tip radius and a full tip cone angle of 40°. (c) Profiles along line 1 in (a) showing dilation effect due to convolution of the initial data with the modeled tip. The diameter is increased by about 9 nm which corresponds to relative error of about 22%.

AFM was used in tapping mode on a regular basis in the frame of this thesis in order to determine the substrate surface roughness or to study droplet formation and distribution. The measurements were carried out using a "MFP 3D" microscope from Asylum Research. Standard tapping mode cantilevers with a nominal resonance frequency of 325 MHz and a spring constant of $46\,\mathrm{N\,m^{-1}}$ from MicroMash were applied. The measuring head of the microscope is placed inside a sonic protective housing to be insolated against disturbing sound from the laboratory environment, e.g. foot fall sound and speech. Under these circumstances, a lateral resolution can be reached of about 10 nm according to the tip radius of standard tapping mode cantilevers whereas the height resolution is of the order of 0.1 nm. Thus, single atomic steps can be resolved. AFM image processing has been done using the open source software *Gwyddion*.

4.3.1 Statistical analysis of topography images

Typically, an AFM image consists of discrete height values $z(x_i, y_j)$ ($i \in [1, N]$ and $j \in [1, M]$) which add up to an image of the sample surface having $N \times M$ data points. The distribution of those height values can give valuable information about characteristics of the scanned surface. An important and probably the most common value for statistical surface characterization is the root mean square (RMS) roughness R_q of a surface which gives the standard deviation of all data points from the mean value and is defined as

$$R_q = \sqrt{\frac{1}{NM}\sum_{i=1}^{N}\sum_{j=1}^{M}\left(z(x_i, y_j) - \bar{z}\right)^2} \tag{4.6}$$

However, R_q does not give any information about the distribution of deviations from the mean value [87]. Therefore, two values are important for a proper characterization of the surface roughness: Skewness R_{sk} is a measure of asymmetry of height distribution which is positive if the scanned surface exhibits more peaks than valleys. Skewness is negative for the opposite case, e.g. a planar surface with predominant valleys. It is defined as follows

$$R_{sk} = \frac{1}{NMR_q^3}\sum_{i=1}^{N}\sum_{j=1}^{M}\left(z(x_i, y_j) - \bar{z}\right)^3 \tag{4.7}$$

Excess kurtosis R_{ku} is a measure for the surface sharpness and is equal to 0 if the height distribution is Gaussian. If R_{ku} is smaller than zero the surface is rather flat while $R_{ku} > 0$ corresponds to many peaks. Kurtosis is calculated in the following way:

$$R_{ku} = \frac{1}{NMR_q^4}\sum_{i=1}^{N}\sum_{j=1}^{M}\left(z(x_i, y_j) - \bar{z}\right)^4 - 3 \tag{4.8}$$

It may be noted that excess kurtosis is derived from the statistical measure kurtosis which is given by $R_{ku} + 3$. Both terms are often used interchangeably.

4.4 Ellipsometry

Ellipsometry is an optical, non-destructive measurement technique that characterizes light reflection from samples by measuring the change in the polarization state. The name ‘ellipsometry’ comes from the fact, that polarized light often becomes elliptically polarized upon reflection. This is caused by different reflection coefficients for s- and p-polarized light due to the difference in electric dipole radiation [88, sec. 2.3]. Furthermore, the phase difference between the polarizations (initially zero in most cases) can be changed due to optical anisotropy resulting in different propagation speed for different polarizations.

Ellipsometry measures two values (Ψ, Δ) which represent the amplitude ratio Ψ and phase difference Δ between p- and s-polarized light (fig. 4.10). In particular the re-

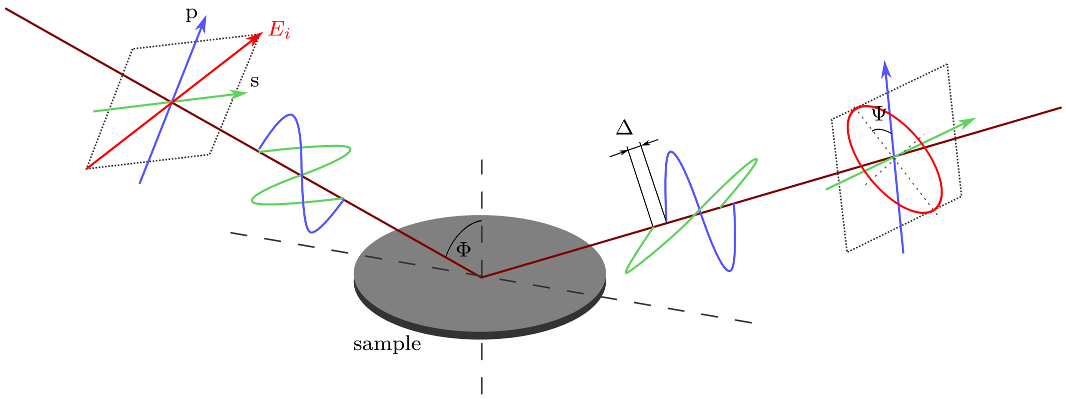

Figure 4.10: Illustration of ellipsometry principle. Incoming light is 45° linearly polarized in most cases. Amplitude and phase of p- and s-polarized components can be changed due to reflection which mostly results in elliptically polarized light.

flectance ratio ρ of p-polarized and s-polarized light is measured, which is defined as

$$\rho = \tan(\Psi)\, e^{i\Delta} = \frac{r_p}{r_s} = \frac{\left(\frac{E_{rp}}{E_{ip}}\right)}{\left(\frac{E_{rs}}{E_{is}}\right)} \tag{4.9}$$

Here, p and s denote p- and s-polarized light whereas i and r denote the electric fields of incident and the reflected wave respectively.

As Ψ and Δ are functions of the applied wavelength in spectroscopic ellipsometry (Ψ, Δ) spectra are measured. In particular, optical constants like refractive index n and extinction coefficient k as well as layer thickness can be determined from the measurement. However, the interpretation of the results from Ψ and Δ is rather difficult. Therefore, the optical constants have to be extracted indirectly by using a layer model of the investigated sample. Hence, fitting the experimental data with the model yields the optical constants and layer thickness.

The setup of the specific ellipsometer depends on how the polarization state of the reflected light is determined. In the simplest case the analyzer is rotated to determine the polarization of the reflected light [88, sec. 4.2.2]. However, rotating the analyzer limits the time that is needed for one measurement. Different techniques have been developed, such as phase modulation ellipsometry, to overcome this drawback. The phase of the reflected light and thus the polarization state can be modulated by using a photoelastic modulator leading to an oscillating intensity signal at fixed polarizer or analyzer angles. The polarization can be modulated very fast (50 MHz) making real-time ellipsometry possible at frame rates as low as 20 µs. A possible setup for phase modulation ellipsometry is depicted in figure 4.11.

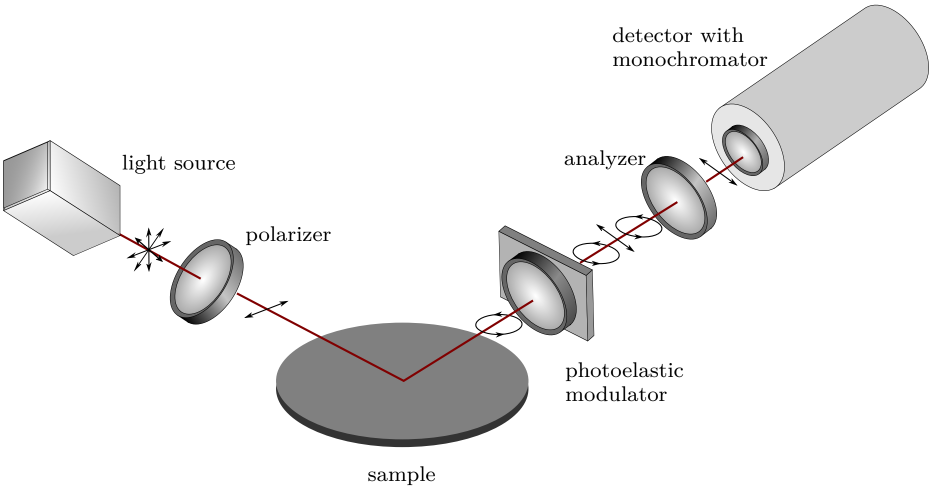

Figure 4.11: Schematic image of a possible setup for phase modulation ellipsometry. The phase of the reflected light is modulated (additional phase change of the form $\delta = F \sin \omega t$). The modulator is often placed in the path of the incident light. The light source is mostly a xenon lamp.

In the frame of this thesis ellipsometry was applied to determine the thickness of HSQ layers, which have been spin-coated onto different substrates (see section 5.6.1). The ellipsometer used for these measurements is a *MM-16*^{TM} from *HORIBA Jobin Yvon*. It is equipped with a spectrometer providing a wavelength resolution of 2 nm in the range of 450 - 850 nm. It was operated at an incident angle of 70°. The measurements have been cross-checked by X-ray reflectometry (see section 4.5) to confirm the suitability of the model which was used to fit the experimental data. Data acquisition, data analysis and modeling was done using the software *DeltaPsi2* provided by the ellipsometer's manufacturer.

4.5 X-Ray Reflectometry (XRR)

In order to determine the thickness of deposited or coated layers on a substrate X-ray reflectometry (XRR) has been used. It was also used to determine the thickness of layers deposited by MBE to calibrate the in-situ rate measurements, i.e. quartz crystal microbalance and cross-beam rate control (see 3.1.3). Also the thickness of HSQ layers measured by ellipsometry has been confirmed by XRR.

In XRR the incident X-rays with a defined wavelength are reflected at the surface and at the interfaces between different layers. Interference of the beams reflected at the interfaces with the primary beam leads to intensity oscillations when varying the incident angle in a $\Theta - 2\Theta$ scan (see figure 4.12).

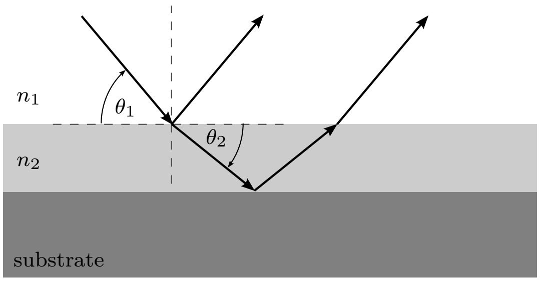

Figure 4.12: Beam path in XRR when $n_2 < n_1$. Reflected beams can interfere at certain incident angles. X-rays at an incident angle which obeys $\cos\theta_{1c} = 1 - \delta$ travel along the surface upon refraction.

The complex refractive index of most materials differs only slightly from unity with a real part smaller than one for X-rays and extreme UV light. Therefore, instead of the usual form $\tilde{n} = n + i\kappa$ it is often expressed in the following way

$$\tilde{n} = 1 - \delta + i\beta \tag{4.10}$$

where δ represents the refraction and β the absorption [89, sec. 3.1]. Since the real part of $\tilde{n}$ is slightly smaller than unity it follows from Snell's law that at grazing incidence the reflectivity becomes unity below a critical angle

$$\cos\theta_c = 1 - \delta \tag{4.11}$$

This effect is called total external reflection analogous to the counterpart, e.g for visible light (total internal reflection). As the absorption is typically in the range of $10^{-6} - 10^{-5}$ in the X-ray regime, θ_c is very small. Thus, equation 4.11 can be approximated for small angles (Taylor expansion unit square term) which leads to

$$\theta_c \approx \sqrt{2\delta} \tag{4.12}$$

At incident angles above θ_c the X-ray beam can penetrate into the material and is reflected, i.e. at the interface to the substrate which gives rise to interference fringes. By varying the incident angle in a $\theta - 2\theta$-scan (incident angle and detector angle are the same) intensity oscillations according to the interference maxima and minima can be measured. The period of these oscillations mainly depends on the thickness and the applied X-ray wavelength.

$$\Delta\theta = \frac{\lambda}{2t} \tag{4.13}$$

From the drop of the intensity with increasing θ the roughness of surface and interfaces can be extracted. Figure 4.14 shows a XRR measurement of a 13 nm gold layer on a Si(111) substrate. The measurements were done at a HRXRD from *Seifert* (nowadays *GE Inspection Technologies*) using a highly monochromatic Cu $K\alpha_1$ beam (8.047 keV, [90]). Analysis and simulation of the data were done with the software *RC Ref Sim*, Vers. 1.09 developed at IHP in Frankfurt (Oder) by Dr. Peter Zaumseil.

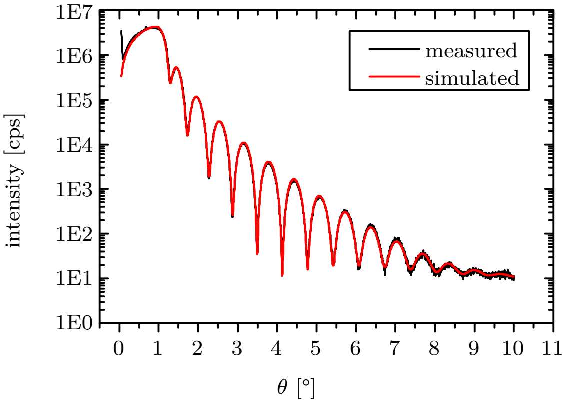

Figure 4.13: XRR measurement (black curve) and simulation (red curve) of a gold layer with a thickness of 13 nm on a Si(111) substrate.

4.6 Fourier transform infrared spectroscopy (FTIR)

FTIR is a technique to obtain infrared spectra of gaseous, liquid or solid compounds in order to analyze the chemical composition. In fact, molecular vibrations are excited due to absorption of photons from incoming light. Incoming infrared light interacts with molecules having a permanent dipole moment which makes those dipoles oscillating. Therefore, diatomic molecules like hydrogen, oxygen or nitrogen having no permanent dipole can not be excited to vibrate under IR illumination.

In contrast to dispersive spectrometers which change the incident wavelength by a monochromator, in FTIR the spectrum is obtained from the fourier transformation of an interferogram. Therefore, a Michelson interferometer is part of any FTIR spectrometer. Polychromatic light passes a beam splitter. The two beams are reflected at one stationary mirror and another mirror which can be moved. The two reflected beams interfere after passing the beam splitter for a second time. The recombined light travels through the sample or may be reflected partly. The detector records the transmitted (reflected) intensity as a function of position of the movable mirror which is also called an interferogram.

Recording and evaluating the interferogram provides information from all wavelengths simultaneously. Therefore, FTIR provides quicker measurements and higher signal-to-noise ratio compared to other spectrometers using dispersive optics.

FTIR has been used in order to characterize HSQ layers before and after curing to monitor changes in the optical transmission spectra due to structural transformation of the layers. Typical absorption bands can be assigned to characteristic vibrational modes which indicate the transformation of HSQ.

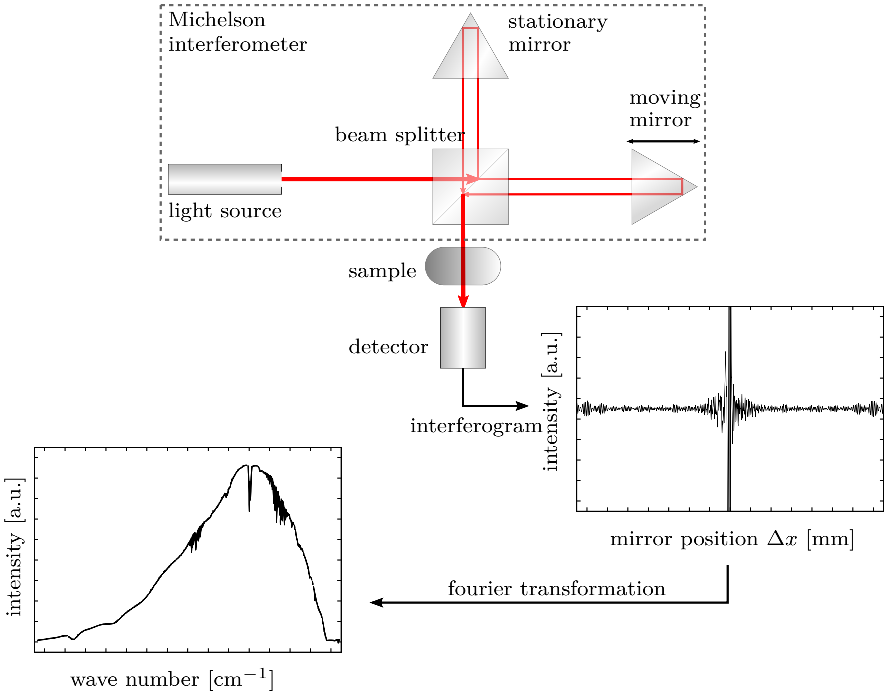

Figure 4.14: Working principle of FTIR. After the Michelson interferometer the beam passes the sample. The detected intensity varies as the position of the moving mirror is changed. $\Delta x = 0$ corresponds to equal pathways of both split beams. Fourier transformation yields intensity as function of wave number.

5 Results and Discussion

5.1 Substrate Characterization

In epitaxy the growth is strongly influenced by the quality of the substrate surface involving morphology and chemical cleanliness. Both criteria are mainly influenced by the substrate preparation like polishing or wet-chemical treatment before the samples are inserted into the UHV chamber. Therefore, different steps of germanium substrate processing have been investigated. The following sections describe how the substrate quality is influenced by different polishing conditions as well as by different wet-chemical treatments.

5.1.1 Influence of the Polishing Process

Most of the applied germanium substrates were made in IKZ. Since the substrate preparation plays a crucial role for the surface quality and hence the growth results, different polishing cloths have been tested in the CMP process in order to observe the influence on the surface quality. For characterization AFM was applied to determine the RMS roughness and surface morphology was studied by means of EBSD and TEM.

Three different polishing cloths have been applied (see sec. 3.2.1) at different contact pressure for the final step of CMP of Ge(111) substrates. The results of the roughness measurement are presented in figure 5.1. Although all substrates show a very low roughness fairly below 1 nm, a clear dependency on the applied cloth can be observed. The smoothest surface is obtained by using Chemcloth whereas the silicon standard CMP cloth provides the highest RMS value. Also the pressure at which the cloth is pressed against the substrate and which is commonly given in units of $\mathrm{g\,cm^{-2}}$ (converted in SI units: $1\,\mathrm{g\,cm^{-2}} \cong 98.1\,\mathrm{N\,m^{-2}}$) plays an important role. On the one hand higher pressure leads to higher abrasion and thus to fast processing, on the other hand higher pressure obviously leads to a higher roughness of the surface. Thus a compromise has to be found. In the frame of this work $200\,\mathrm{g\,cm^{-2}}$ and $300\,\mathrm{g\,cm^{-2}}$ have been compared in order to find appropriate polishing conditions. As a result the smoothest surfaces could be obtained by applying the lower pressure.

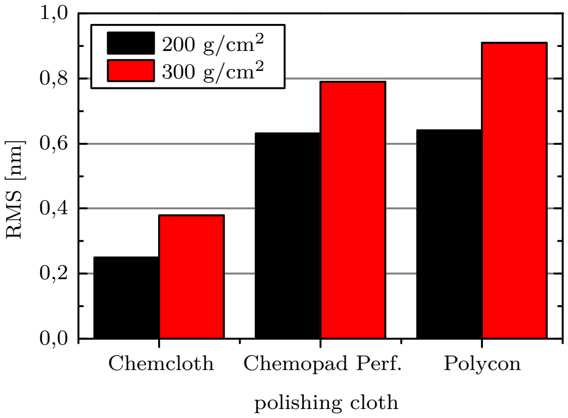

Figure 5.1: Roughness measurements of Ge(111) substrates polished with three different polishing cloths. Each cloth has been applied at a pressure of 200 g cm^{-2} and 300 g cm^{-2}. A scan size of 5 µm was applied.

In order to determine the quality of the surface in terms of structural defects (sub-surface damage) EBSD measurements have been done to obtain mappings of the so-called image quality factor (IQ). The latter is basically a function of contrast between Kikuchi bands and the background where higher contrasts indicate a higher perfection of the crystal structure of the probed area. EBSD probes the uppermost atomic layers and is therefore sensitive to any distortion in the crystal lattice near the surface. Thereby, relative values for the surface quality can be given in comparison of different samples or in comparison with a standard sample. Figure 5.2 shows IQ maps from differently polished substrates. Substrates polished with a Chemcloth also provide the highest image quality factor which is in good agreement with the roughness measurements presented above. However, from IQ maps it is complicated to distinguish between structural defects of the lattice and roughness induced drop of the IQ factor.

Therefore, TEM samples of a substrate polished with Chemcloth and another one polished with Polycon have been prepared to confirm whether there is any sub-surface damage. TEM images are presented in figure 5.3. For direct comparison two different substrates have been glued against each other and have been prepared by conventional TEM preparation including polishing and Ar ion milling (see section 4.2.1).

According to these TEM studies no sub-surface damage could be observed which confirms the good quality of the substrates. Several monoatomic steps can be found. However, the distance between the steps is typically lower than the lateral resolution of the

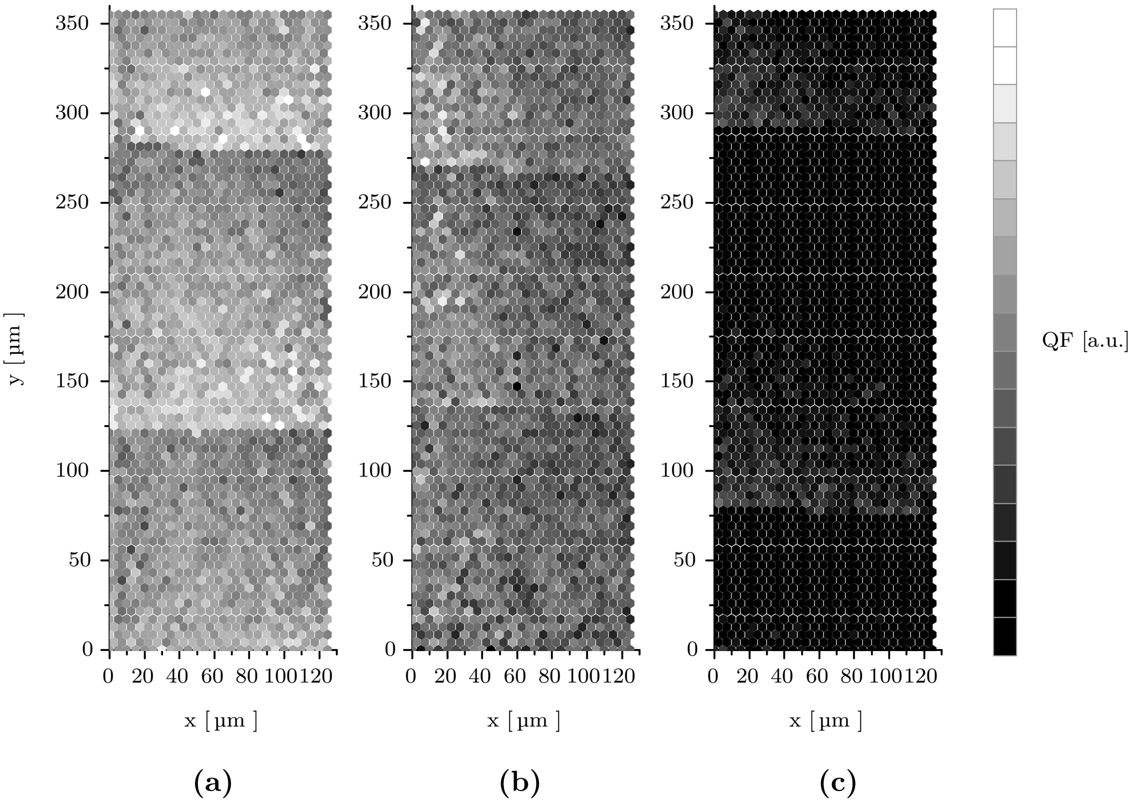

(a) **(b)** **(c)**

Figure 5.2: EBSD image quality (IQ) factor maps of germanium substrates polished with different polishing cloths at 300 g cm^{-2}: (a) Chemcloth, (b) Chemopad Perforate and (c) Polycon. The IQ factor gives the band contrast and thus the pattern quality. Brighter Pixels indicate a higher pattern quality. The maps cover a sample area of 125 µm × 355 µm.

AFM measurements. Therefore, these steps (about 7 steps within 50 nm) can not be correlated with RMS roughness measured by AFM.

5.1.2 Influence of passivation treatments

Typically, the substrates are of epi-ready grade and provide an RMS roughness below 1 nm. As described in section 3.2.2 substrates undergo further wet-chemical cleaning to provide a contamination free surface prior to epitaxy. In order to analyze the effect of chemical treatment, two pieces of a sample have been inserted into the MBE chamber, one of them freed from dust by flowing nitrogen merely covered with native oxide while the other was chloride passivated. It may be noted, that wet-chemical treatment accompanies with removal of material upon etching processes in HCl. Both pieces have been annealed at 700 °C to desorb passivation layer and oxide layer respectively. In this way, the initial condition of the substrate surface before growth can be compared with and without

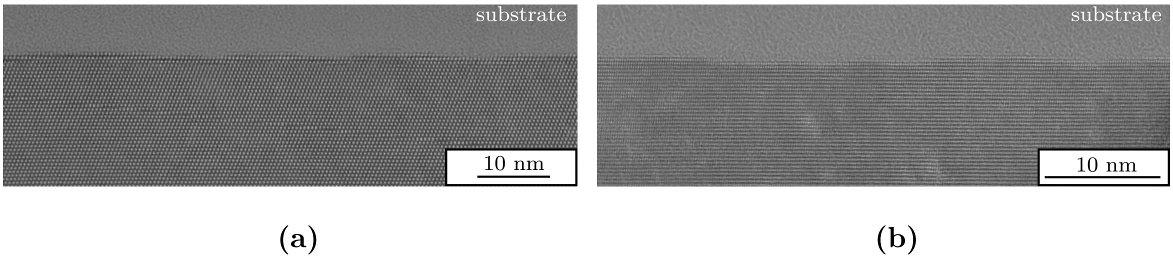

(a) (b)

Figure 5.3: TEM micrographs of Ge(111) substrates targeting possible sub-surface damage caused by CMP. Two different polishing clothes have been used: (a) Chemcloth, (b) Polycon.

wet-chemical passivation.

The samples have been characterized by means of AFM which is presented in figure 5.4. Both show a very similar RMS roughness below 0.5 nm. Nevertheless, there are differences in the surface topography. The non-treated sample exhibits many small hillocks and valleys whereas areas of constant height level are considerably larger on the Cl-passivated sample meaning that there are larger areas which can be assumed as atomically flat. This finding is confirmed by statistical analysis of the AFM images. Although the surface shown in figure 5.4(b) has a higher RMS value, the described characteristics can be seen on the basis of the negative excess kurtosis value R_{ku} which stands for rather large flat areas while it is positive for the untreated surface indicating the presence of many small peaks and valleys. The values are given in table 5.1. In that sense, the kurtosis correlates with the number of atomic steps per unit area which is less on pretreated substrates.

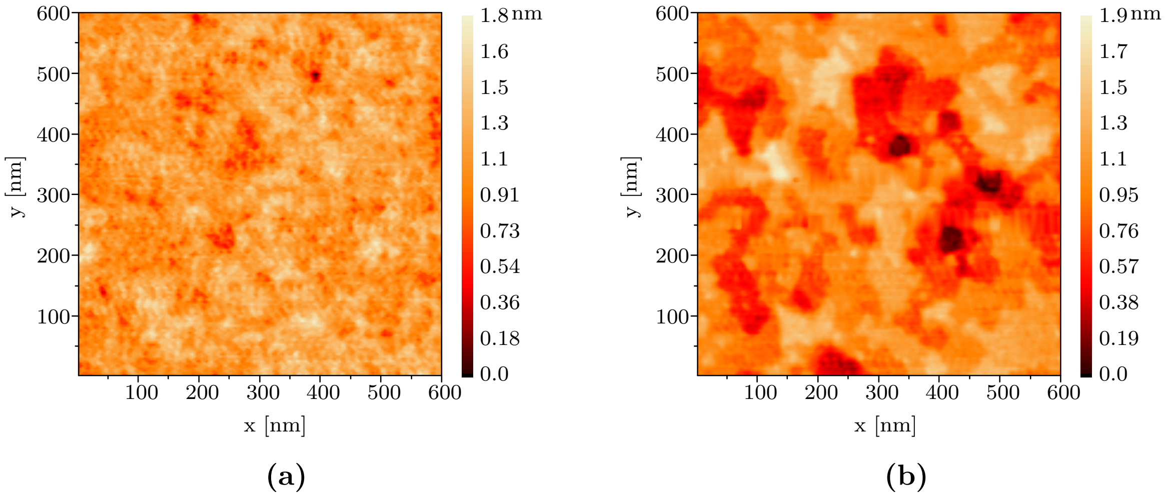

(a) (b)

Figure 5.4: AFM scans of Ge(111) substrates after annealing under UHV conditions. Substrates underwent different preparation: (a) Non-passivated with native oxide and (b) Cl-passivated prior to annealing.

pre-treatment	roughness R_q	excess kurtosis R_{ku}
as polished	0.19 nm	0.13
Cl-passivated	0.28 nm	-0.17

Table 5.1: Roughness and kurtosis for Ge(111) which are non-passivated and Cl-passivated prior to annealing. Values are taken from statistical evaluation of figure 5.4 (a) and (b) respectively.

5.2 Droplet Formation

There are two different ways to create gold droplets by evaporating Au. A common way is to deposit a layer of gold onto the cold substrate. Subsequent heating above the eutectic temperature leads to dewetting of the substrate and the formation of droplets. Thereby the droplet diameter is basically a function of thickness of the gold layer. The second method is to deposit gold onto the heated substrate. The gold droplets form successively in the initial stage of deposition. The diameter of droplets can be influenced by substrate temperature, deposited amount of gold and the evaporation rate which gives an additional parameter to tune diameter distribution of the gold droplets. This is a general advantage of the second route of droplet formation.

While gold is deposited on the heated substrate atoms diffuse along the surface until a position is reached where they nucleate or are incorporated into an existing droplet. As a result, a certain distribution of droplet radii is established. Figure 5.5 shows one example for such a distribution which can be approximated by a Gaussian fit. Droplet formation is possible even below the eutectic temperature (361 ℃) because atoms are evaporated from the hot effusion cell and are able to form clusters before their kinetic energy dissipates. In this way very small clusters of radii down to 20 nm or below have been created.

A temperature series starting at low temperatures has been undertaken to find a lowest temperature at which gold droplets form. Starting at 350 ℃ the temperature was lowered until no droplets have been observed anymore. Eventually, temperature was found to be low enough between 270 ℃ and 250 ℃ to hinder gold atoms to form droplets. Instead, diffusion of the atoms is lowered such that they begin to form aligned clusters according to the underlying symmetry of atomic steps that are present on the substrate surface. This effect can be illustrated well on Ge(001) substrates that provide those steps along [1 1 0] and [1 -1 0] resulting in a rectangular alignment of gold clusters. Size reduction of the droplets and formation of aligned clusters are shown in figure 5.6.

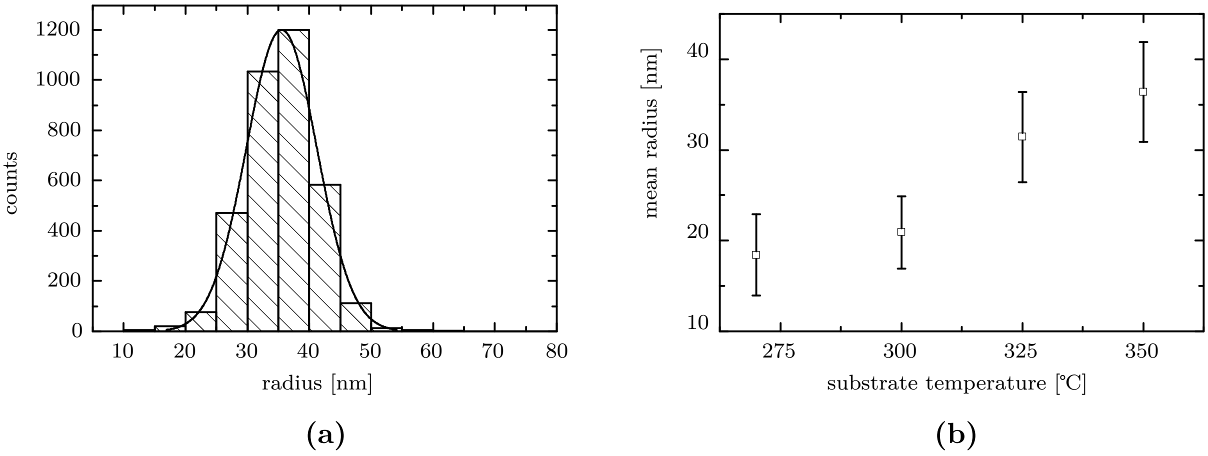

Figure 5.5: (a) Au droplet distribution at a deposition rate of 0.0342 nm s^{-1} and a substrate temperature of 350 °C. (b) Temperature dependence of droplet radius. Error bars indicate standard deviations from size distributions as shown in (a).

However, in order to use the droplets for nanowire growth by the VLS mechanism the sample temperature has to be ramped up to growth temperature of the nanowires which is typically above 400 °C (see sec. 5.3.5). Consequently, Ostwald ripening sets in which lets the radius distribution shift to higher radii. It turns out, this process takes place fast enough to establish a mean droplet radius which is typical for the final nanowire growth temperature. This means, creating small droplets at low temperatures does not define the final nanowire radius and thus a different method has to be found to effectively decrease the average droplet diameter.

In a further approach, evaporation rate and total amount of gold have been tuned in order to obtain droplets as small as possible even at substrate temperatures of 430 °C. First, the droplet size is determined by the total amount of gold, which equals 1 nm layer thickness in previous experiments that were carried out at low substrate temperatures (see above).

Additionally, droplet formation can be considered as being governed by surface diffusion of the gold atoms as it is described in section 2.4.3. This means higher diffusivity leads to lower areal density of the droplets because it is more likely to find an already existing droplet to join instead of taking part in another nucleation event. On the other hand, nucleation density (nucleation events per unit area and unit time) increases with impingement rate of the atoms and therefore higher droplet density with lower average droplet radii are expected if the total amount of gold remains constant. Consequently,

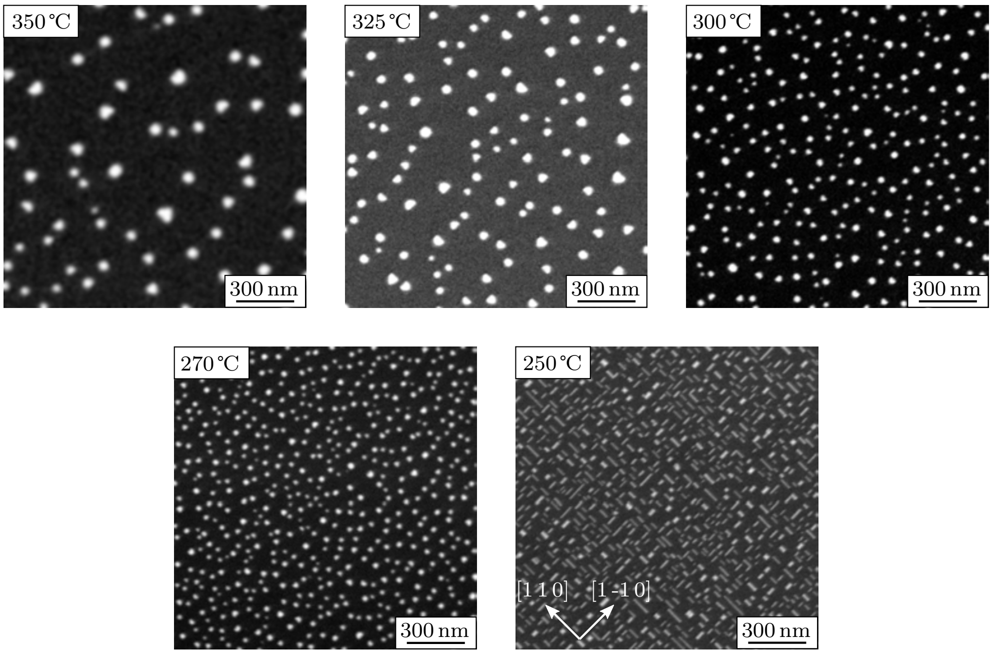

Figure 5.6: Series of SEM images illustrating the change in droplet formation at decreasing temperatures below the Au–Ge eutectic temperature.

less gold deposited at high rates should effectively decrease the average droplet radius. Therefore, samples have been prepared using 1.0 nm, 0.8 nm and 0.5 nm of gold at 6-fold deposition rate compared to previously used $0.017\,\mathrm{nm\,s^{-1}}$. The samples were characterized by means of AFM measurements which were analyzed statistically. Obtained data are presented in figure 5.7.

Contrary to the expectation saying that the average droplet radius should decrease, there was no clear trend going along with decreasing amount of gold. Instead the average height of the droplets becomes smaller with less amount of gold and correspondingly the aspect ratio decreases by a factor of two. This means the droplets become rather flat than reducing their radius significantly which indicates pinning of the triple phase line (boundary/circumferrence of the drop) due to surface roughness of the underlying substrate. Therefore, at small radii the specific surface conditions of the substrate may influence the resulting droplet radius even more than process parameters like temperature, rate or total amount of gold. Such a strong dependency on substrate properties may lead to worse reproducibility while the width of size distribution of droplets can increase.

Alternatively, monodisperse, colloidal gold could be used to provide gold particles with the desired diameter providing a sharp size distribution. Colloidal gold is available in suspensions and can be spin coated. Thereby, the particle concentration needs to be adjusted to obtain an appropriate areal density on the sample.

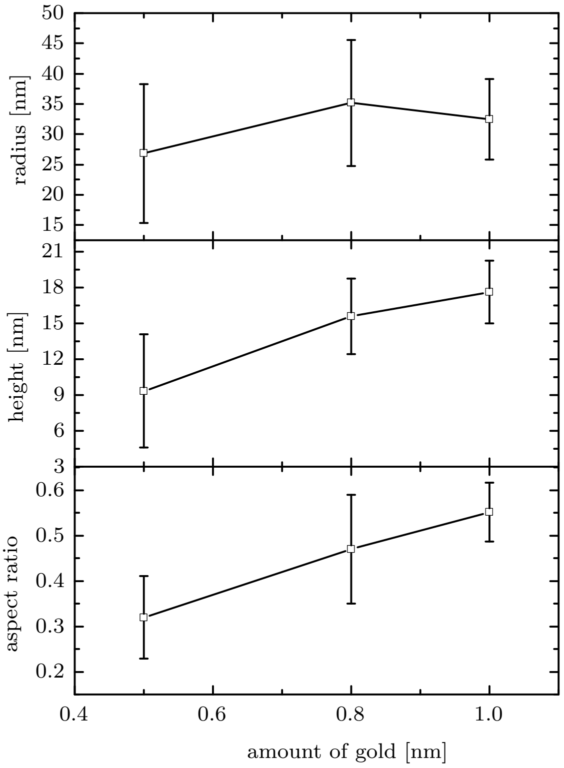

Figure 5.7: Statistical analysis of small droplets. Error bars represent standard deviations from statistical evaluation. Gold was deposited at a rate of 0.10 nm s^{-1}.

5.2.1 Influence of passivation

As described at the end of the previous section, surface conditions such as roughness or surface termination may play an important role for droplet formation. In this section the influence of surface passivation, as it is described in section 3.2.2, on the droplet formation is explained. Two pieces of the same Ge(111), one of them Cl-passivated and the other without chemical treatment, have been simultaneously processed. After annealing 1 nm of gold was deposited at a rate 0.017 nm s^{-1} and at a substrate temperature of 430 °C. Subsequently, the samples were analyzed by means of AFM which is presented in figure 5.8.

As can be seen, droplet formation depends on whether the substrate has been treated wet-chemically including surface termination or not. Many small droplets form on a non-passivated substrate whereas less but bigger droplets are observed on the previously

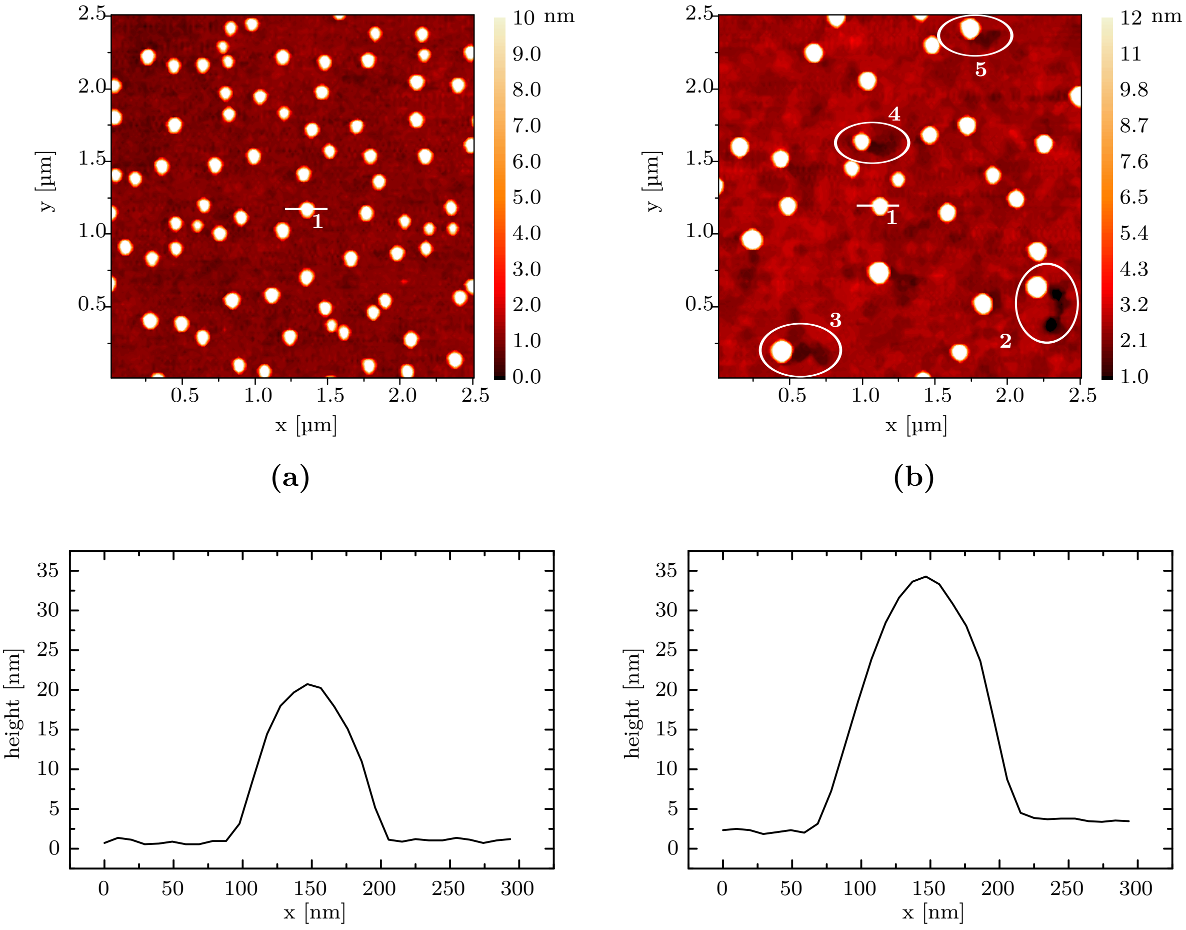

(a) **(b)**

(c) **(d)**

Figure 5.8: AFM scans of gold droplets on Ge(111) (a) non-passivated and (b) passivated. The lines marked with 1 indicate locations where profiles in (c) and (d) have been recorded. In (b) many droplets exhibit trench-like traces with a depth of merely 2–4 monolayers. Most obvious traces were marked by regions 2-5.

wet-chemically treated surface. This can be explained by surface roughness effects. As explained in section 5.1.2, terminated surfaces exhibit lower surface roughness after annealing whereupon atomic surface steps and terraces become visible. It seems clear that diffusivity on those surfaces is higher compared to non-treated substrates.

The characteristics of differently pre-treated surfaces also has an impact on the movement of already existing droplets as can be seen in 5.8(b) where many of them show small depressions with a depth of a few atomic layers. Obviously, droplets are able to move while they grow further and begin to dissolve the substrate until they are saturated which finally creates a small trench behind them. The mobility of droplets on passivated substrates can be explained on the basis of the surface excess kurtosis (see sec. 5.1.2).

(hkl)	σ_{Si} [$10^{-3}\,\mathrm{J\,m^{-2}}$]	σ_{Ge} [$10^{-3}\,\mathrm{J\,m^{-2}}$]
(001)	1879.82 [a], 2130 [b]	1657.18 [a], 1835 [b]
(011)	1535.88 [a], 1510 [b]	1412.78 [a], 1300 [b]
(111)	1254.24 [a], 1230 [b]	1153.72 [a], 1060 [b]

Table 5.2: Surface energies of selected Si and Ge surfaces. Footnote *a* corresponds to reference [91] while *b* corresponds to [92].

The latter is negative on passivated substrates which correlates with less atomic steps per unit area. Atoms at step edges are preferentially dissolved because they exhibit a higher chemical potential (are more loosely bound). This can be a driving force for droplet movement along an edge. In contrary, a non-passivated surface shows more steps per unit area such that a droplet is in contact with many step edges. Therefore, no resulting movement will occur along a predominant direction in most cases. This may also have consequences for the nucleation of nanowires which is explained in detail in section 5.4.

5.2.2 Wetting behavior on germanium and silicon

Wetting of gold on silicon or germanium surfaces is mainly governed by the specific surface energy of the respective substrate surface. In general, surfaces with higher surface energy are preferentially wetted because the total energy can be lowered by the formation of a liquid-solid interface. Typically, silicon surfaces have higher surface energies than their germanium counterpart as can be seen in table 5.2 which gives an overview of such values taken from literature for different crystallographic faces.

In order to check whether gold shows different wetting behavior on silicon and germanium surfaces, Si(111) and Ge(111) substrates have been prepared and 1 nm of gold has been deposited at 450 ℃. The processed samples have been analyzed by means of AFM which is depicted in figure 5.9. As a result, gold wets Si(111) better which is indicated by the formation of many tiny gold clusters all over the surface. However, the distribution of the clusters does not indicate any Ostwald ripening which would result in less clusters in the vicinity of the larger droplets. Thus, cluster do not form under the same conditions as the larger droplets do. It is rather assumed that they result from a gold wetting layer which disintegrates due to cool down of the sample after the deposition process.

On Ge(111) no clusters are detected in the vicinity of droplets and consequently, droplets on germanium are expected to be larger as all gold is rather collected in the droplets than being spread over the surface and forming a wetting layer. This conclusion could be also confirmed and is illustrated by line profiles in figures 5.9(c), (d). These findings will be of great significance in the following section, since nanowire growth is significantly influenced by the wetting of the solvent.

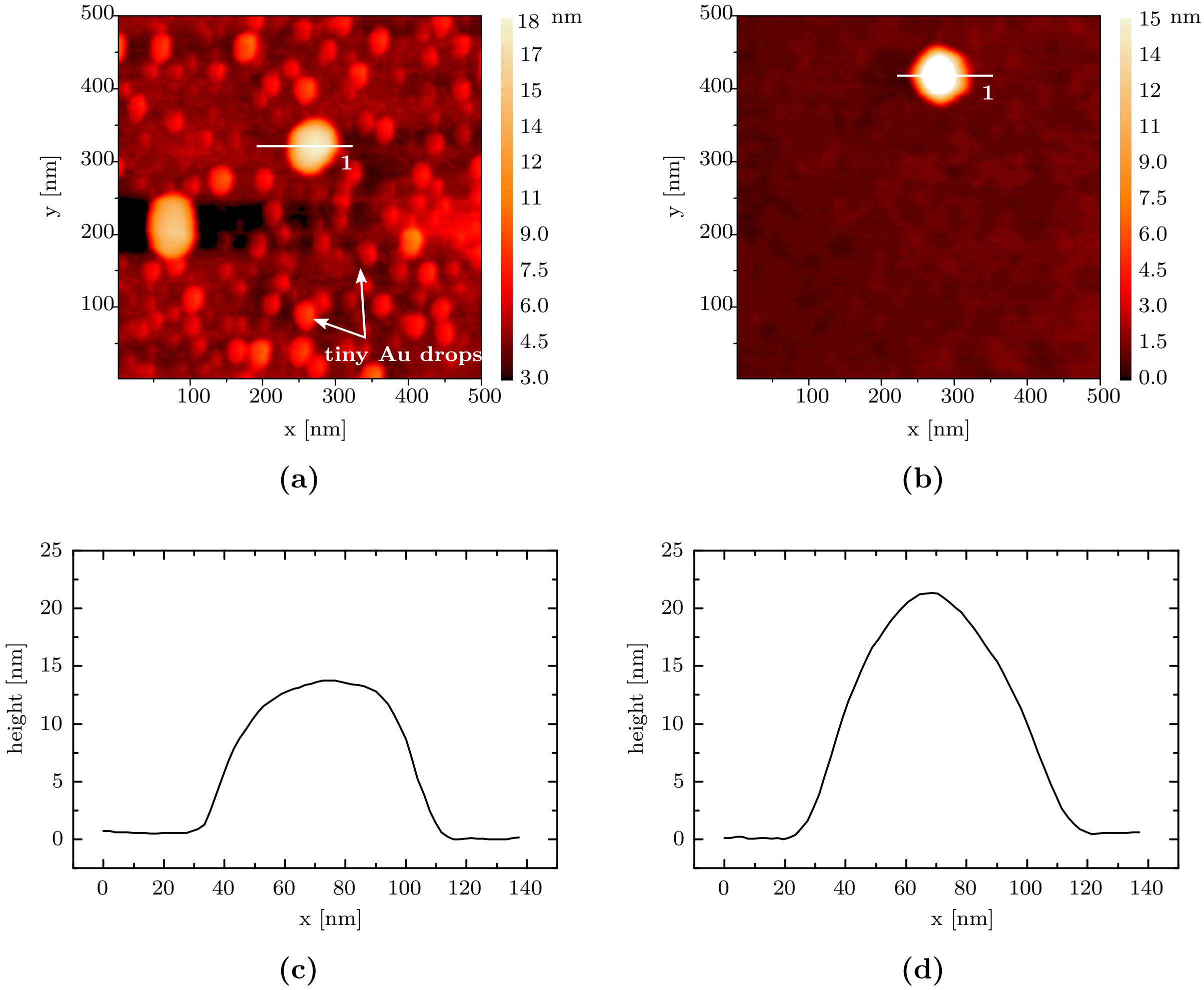

(a) (b)

(c) (d)

Figure 5.9: Gold shows different wetting behavior on (a) Si(111) and (b) Ge(111). On silicon many tiny droplets remain on the surface whereas on germanium only big droplets are observed while the germanium surface in between shows no indication for gold clusters.

5.3 Nanowire growth

After droplet formation the temperature is ramped to the respective NW growth temperature and the germanium deposition is started. Whereas silicon nanowires are typically grown at 500 °C or higher [54] growth of germanium nanowires by MBE takes place at temperatures above 370 °C. It may be noted at this point that germanium nanowire growth at temperatures far below the eutectic temperature (361 °C) has been reported in literature but only in CVD processes using germane (GeH_4) or digermane (Ge_2H_6). In the frame of this thesis nanowire growth was observed from 370 ℃ to 510 ℃.

5.3.1 Morphology of germanium nanowires

In the following sections the morphology of germanium nanowires is reported, i.e. axial growth directions and faceting of the nanowires. Those two characteristics are closely connected since different crystallographic growth directions also lead to different side wall faceting of the nanowires. In general, the main driving force for growth direction and faceting is the minimization of the free energy which is mainly influenced by surface energies of exhibited facets as will be discussed within this section.

Growth direction

In contrast to silicon nanowires which grow preferentially along ⟨111⟩ on (111) oriented substrates [54] Ge nanowires show different growth directions on Ge(111). Figure 5.10 shows a typical growth results on a Ge(011) and a Ge(111) substrate.

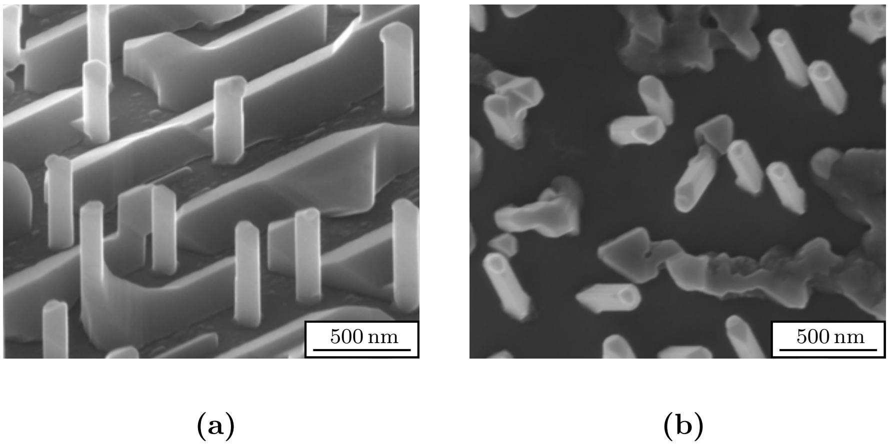

(a) (b)

Figure 5.10: Ge NWs grown on (a) Ge(011) and (b) Ge(111) substrates. NWs grow perpendicular to the surface on Ge(011) (45° tilted view) whereas three characteristic growth angles can be identified on Ge(111). Island growth can be seen in between the NW which is typical for MBE growth. Growth conditions: substrate temperature: 430 ℃, deposition rate: $0.0128\,\mathrm{nm\,s^{-1}}$.

To analyze this phenomenon, experiments have been carried out on (001), (011) and (111) oriented germanium substrates. The inclination of the nanowires on the respective substrates was measured by means of SEM by tilting the sample stage until the nanowires are approximately parallel to the optical axis. Thus, the tilt angle of the stage is equal to the inclination angle of the nanowires.

As a result, characteristic growth angles between substrate normal and nanowire axis could be identified. Stereographic projections of the germanium lattice provide useful overview about angles between lattice planes in the germanium lattice (space group Fd$\bar{3}$m) to find out if any crystallographic direction is related to the measured angles. An analysis has shown that each of the growth angles corresponds to a $\langle 011 \rangle$ crystallographic direction.

substrate	measured angle	angle of $\langle 011 \rangle$
Ge(001)	45°	45°
Ge(011)	0°, $> 52°$	0°, 60°
Ge (111)	35°	35.3°

Table 5.3: Measured growth angles of Ge NW and angles between $\langle 011 \rangle$ and substrate normal. Measurements were done by tilting the SEM sample stage until wire and optical axis are parallel. The maximum tilt angle of the stage is 52°. The uncertainty is about 1°.

Indeed, nanowire growth was observed along each of the possible $\langle 011 \rangle$ directions. Even more, those growth directions have been found exclusively. Table 5.4 gives an overview of the growth directions which are observed.

Nanowires grown along $\langle 111 \rangle$ could not be observed which seems to be typical for physical vapor deposition as it has been reported in literature [93, 94]. This effect can be attributed to lower supersaturation compared to CVD in which the gaseous precursor is catalytically cracked which results in a high material flux into the droplet. The change in growth direction from $\langle 111 \rangle$ to $\langle 011 \rangle$ was explained theoretically by Schwarz and Tersoff [95]. Details on their model and different approaches are described in the section 5.3.3.

Faceting

Not only growth directions differ significantly from the morphology which is known from silicon nanowires but also different facets can be expected which form the sidewalls as well as the nanowire tip. The reason for different faceting is basically given by the minimization of total surface energy of the sidewalls. Silicon nanowires growing along $\langle 111 \rangle$ can not develop $\{111\}$ side facets which are parallel to the growth axis. Ross et al. [96] found a so-called sawtooth faceting instead which consists of alternating $\{111\}$ and $\{113\}$ facets (see figure 5.11).

Since germanium nanowires grow preferentially along $\langle 011 \rangle$ in contrast to silicon nanowires, different sidewall faceting can be expected, too. Indeed, germanium nanowires have been found to be defined mainly by four $\{111\}$ facets (see figure 5.10 and 5.12). Thereby, thin

substrate, growth angle	SEM micrograph	illustration	stereogram
Ge(001) 45°	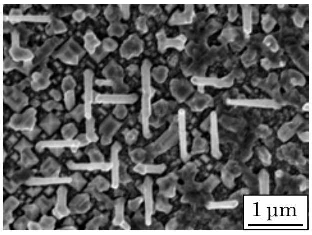	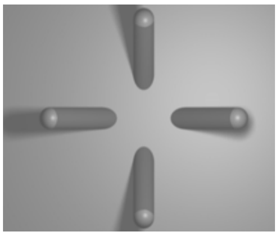	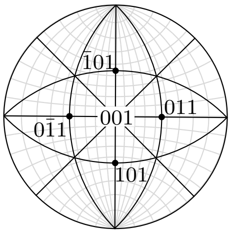
Ge(011) 0°, 60°	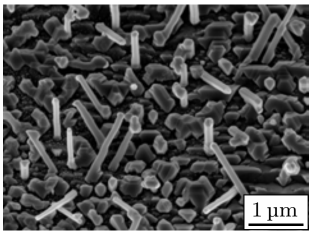	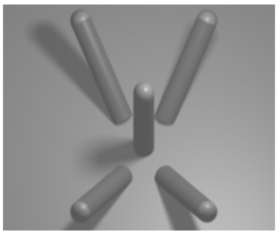	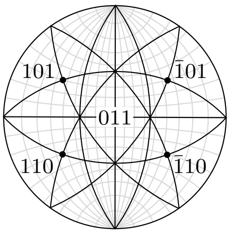
Ge(111) 35.3°	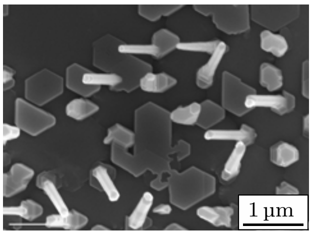	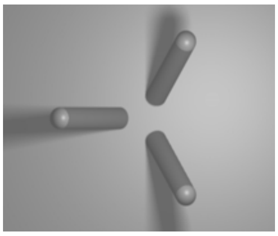	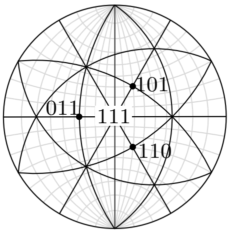

Table 5.4: Overview of observed growth directions of germanium NW on Ge(001), Ge(011) and Ge(111) substrates. Illustrations show rendered 3d models of the NW. Angles were taken from table 5.3.

nanowires exhibit another two {001} side facets which tend to diminish at thicker wires upon faster radial growth of {001} compared to {111} facets (due to higher packing density of a {111} surface). The {111} side facets are atomically flat with merely single atomic steps as could be confirmed by TEM cross-sectional investigations which is illustrated in figure 5.12. The steps may originate from Ge diffusion along the sidewalls as mainly steps downwards have been found in the direction of growth. However, those single atomic steps do not result in any significant tapering of the wire as can be seen in SEM micrographs like e.g. in figure 5.10.

Furthermore, the investigated Ge nanowires do not have a flat {011} facet at the tip. Instead, a v-shaped tip has been found on many SEM micrographs. To clarify the tip's nature TEM studies could provide useful information. However, in transmission electron micrographs the nanowire tip is covered by the gold droplet as can be seen in figure 5.13(a). To overcome this obstacle, EDX mapping was used to image the elemental distribution of Au and Ge in the nanowire. Ge Kα radiation can easily penetrate the

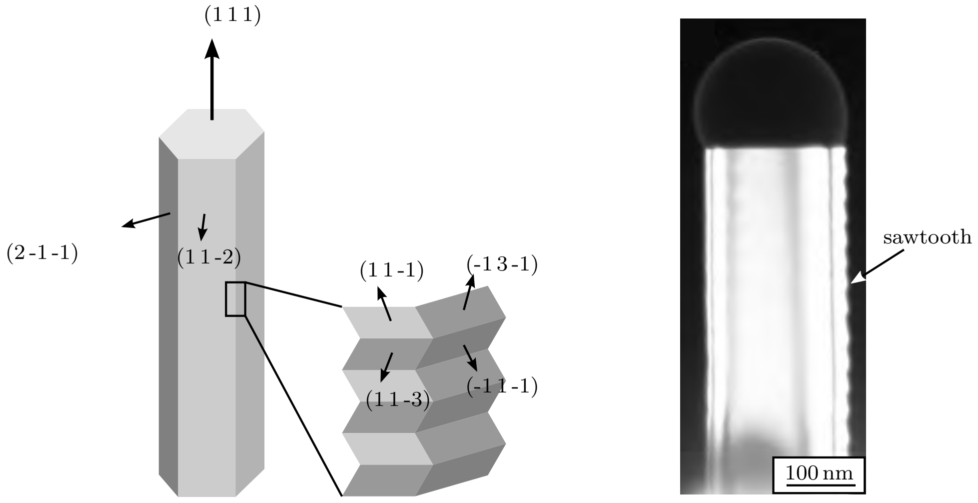

(a) (b)

Figure 5.11: Sawtooth faceting of Si NW sidewalls. (a) Si NW show hexagonal cross section bordered by six {112} oriented sidewalls consisting of alternating {111} and {113} nano-facets. (b) TEM micrograph taken from [96].

gold particle and thus gives the Ge distribution in the tip region. Thus, the gold can be masked and the bare germanium nanowire can be visualised. Figures 5.13 (b) and (c) show the obtained Au Mα and Ge Kα maps. The Ge-map clearly shows the v-shaped morphology of the tip of which an opening angle was determined to be $110 \pm 5°$. To identify the facets which form the v-shape, possible combinations of facets have been searched in the Ge(011) stereograph. As such, the angle between the surface normals of (111) and (-111) is equal to 70.5° giving an opening angle between the corresponding facets of 109.5°. This finding is in good agreement with TEM studies done by Hanrath et al. [97].

5.3.2 TEM investigation of nanowire base

The growth direction obviously turns towards any of the available $\langle 011 \rangle$ directions at the beginning of the growth. Therefore, the structural analysis of the nanowire base is of interest to reveal whether there are any defects (e.g. twin boundaries) introduced in the course of nanowire nucleation.

So far, the change towards $\langle 011 \rangle$ directions has not been observed by means of TEM. In this work, TEM samples of nanowires have been prepared in order to observe crystalline perfection at the nanowire base. Two different samples have been prepared, one by FIB and the other by conventional preparation. FIB allows a direct selection of a single

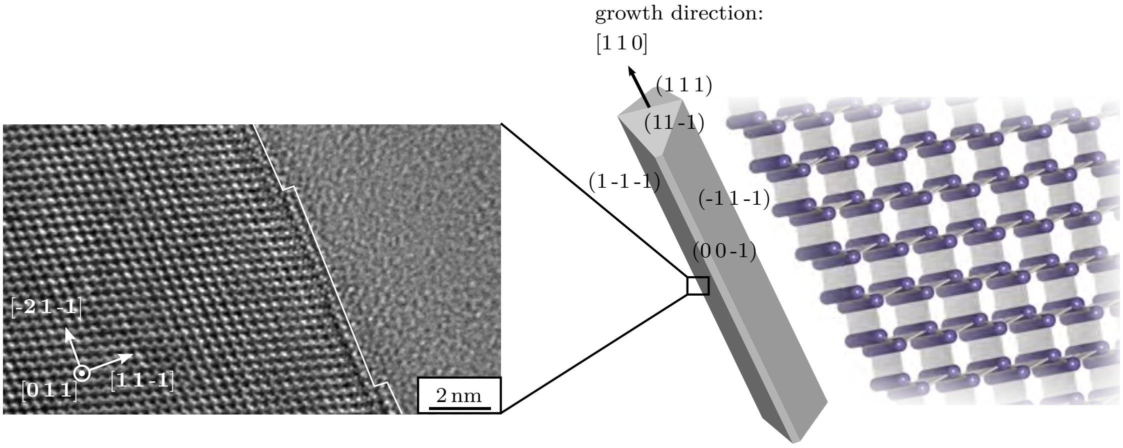

Figure 5.12: Morphology of germanium NWs. The model shows a $\langle 110 \rangle$ grown NW showing a faceting as it is described in the text. The TEM micrograph on the left shows a cross section of a 111 side facet which exhibits single atomic steps (illustrated by white line).

nanowire to by investigated (see sec. 4.2.2). Figure 5.14(a) shows a TEM micrograph of the sample prepared as FIB lamella in which a section of the inclined nanowire can be seen whose surface is enclosed by a platinum protection layer. Another interesting phenomenon in figure 5.14(a) is the presence of a socket at the nanowire base which either nucleates before the nanowire is growing on top or it formes during the growth due to further attachment of germanium. However, socket formation does not occur at all nanowires but seems to be a random effect. At higher magnifications it turns out that the thickness of the FIB lamella (nominal 80 nm) is substantially larger than of conventionally prepared samples which makes it difficult to resolve the crystal lattice. Therefore, the second sample has been prepared by conventional preparation (sandwich technique) in which two pieces are glued together in a face-to-face geometry and are thinned in various steps (see sec. 4.2.1). Although such samples enable higher resolution, the thinned region is positioned randomly and does not necessarily contain the base region of a nanowire for characterization since only every third nanowire is aligned along the plane which is defined by the TEM lamella. Fortunately, the preparation of a single nanowire was successful, eventually.

Figure 5.14(b) shows a TEM micrograph in which the crystal lattice in the base region of the nanowire is resolved. Two diffractograms (proportional to squared absolute value of FFT) from substrate and nanowire have been extracted showing the same periodicity and orientation of the lattice which confirms that no crystal defect, such as twinning, initiates the inclined growth. However, twins which already exist in the substrate and protrude the surface as shown in figure 5.14(b) can be preferred sites of nucleation but are

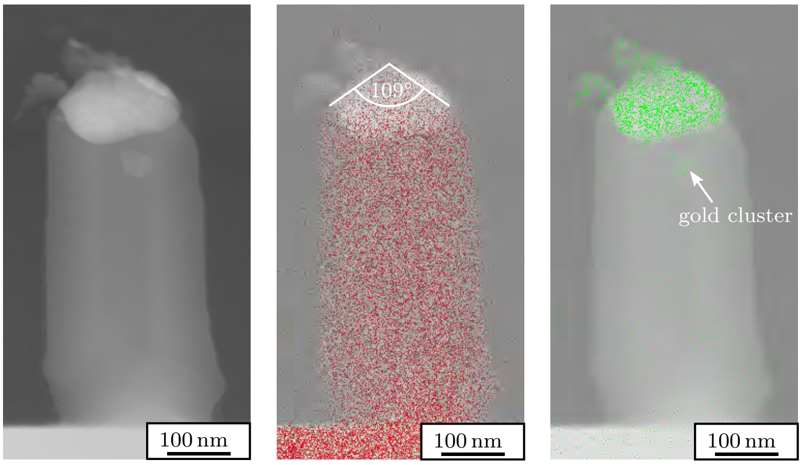

(a) (b) (c)

Figure 5.13: EDX scans of GeNW. The sample was aligned along the ⟨011⟩ zone axis (viewing direction). (a) TEM image of non-inclined Ge NW on Ge(011) substrate. (b) EDX map of Ge Kα. (c) EDX map of Au Mα.

not supposed to be responsible for inclined growth either. Consequently, preferred growth along ⟨011⟩ is evoked by thermodynamic effects concerning the reduction of surface or edge energies which will be discussed in the next section.

5.3.3 Origins of directional nanowire growth

Directional growth of nanowires is of great importance because on the one hand maintaining the desired growth direction is mandatory for any future application and on the other hand controlled directional growth can be of interest in terms of guiding the nanowire e.g. towards a desired contact.

The effect of kinking initiated by changes of growth conditions is well known for silicon nanowires [98, 99]. Thereby, kinking is evoked by another facet that emerges from the triple phase boundary and evolves to the new top facet. As reported by Madras et al. the described process leads to kinking from one ⟨111⟩ growth direction to another while no structural defects are introduced [98, 99].

The morphological characteristics of germanium nanowires described previously in section 5.3.1 differ significantly from those which are known for silicon. Most similarities can be found at silicon wires grown at very low diameters below 10 nm which also show preferential ⟨011⟩ growth [100, 101]. The latter effect has been attributed to a reduction of edge and surface energies of nanowire sidewalls which leads to ⟨011⟩ growth below a certain critical radius.

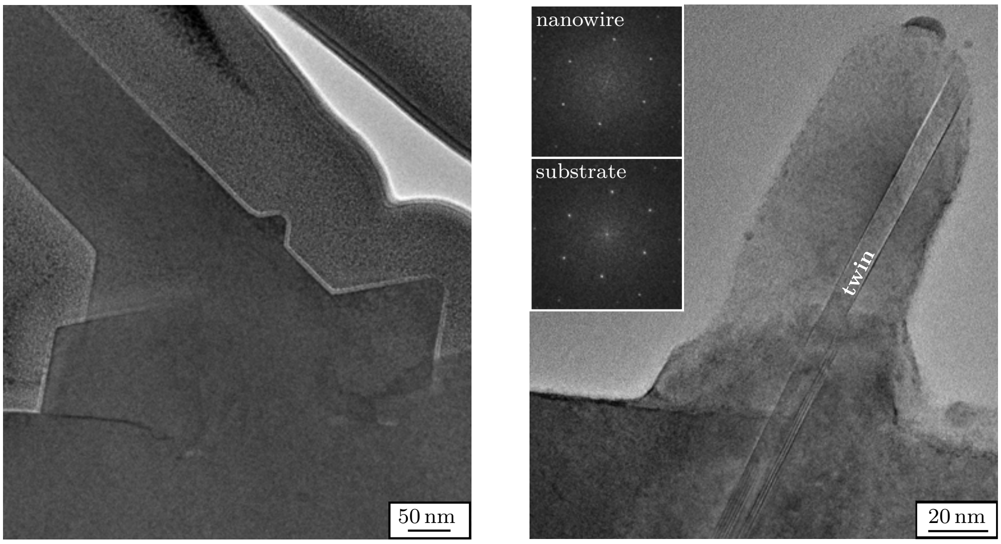

(a) (b)

Figure 5.14: TEM micrographs of ⟨011⟩ grown NW. (a) FIB cut lamella. Nanowire grown on top of an island. Surface is covered with platinum protection layer. (b) Conventionally prepared sample showing one of smaller nanowires. A twin originating from the substrate (as grown Ge layer) proceeds into the nanowire the same way as the non-twinned lattice does.

However, such a radius dependency is not known in the case of germanium while directional growth of germanium nanowires is subject to current research in several groups [94]. Kramer et al. presented a model considering 2D nucleation inside the droplet depending on supersaturation [102]. Thereby, a (011) nucleus has a smaller critical energy ΔG^* (see section eqn. (2.28)) at lower supersaturation whereas (111) nucleation shows smaller ΔG^* in the opposite case. The fundamentals of the model are depicted in figure 5.15.

However, the model of Kramer et al. has some shortcomings. First of all, it is assumed that germanium nanowires nucleate via 2D nucleation which is not in accordance with experimental results made by Ross et al. who observed layer by layer growth in a step flow mode starting at the triple phase line [23]. The nucleation energy is supposed to be significantly lower at the triple phase boundary and therefore it seems that no 2D nucleus is forming during the growth. Furthermore, it is shown in section 5.3.1 that no (011) top facet is found on top of the wire but a v-shaped tip consisting of two (111) facets which indicates that no (011) 2D nucleation takes place.

Another model introduced by Schwarz and Tersoff considers two (111) facets which form a v-shaped tip, as it occurs in the case of germanium nanowires, and which can grow simultaneously depending on the supersaturation [95]. The situation is depicted

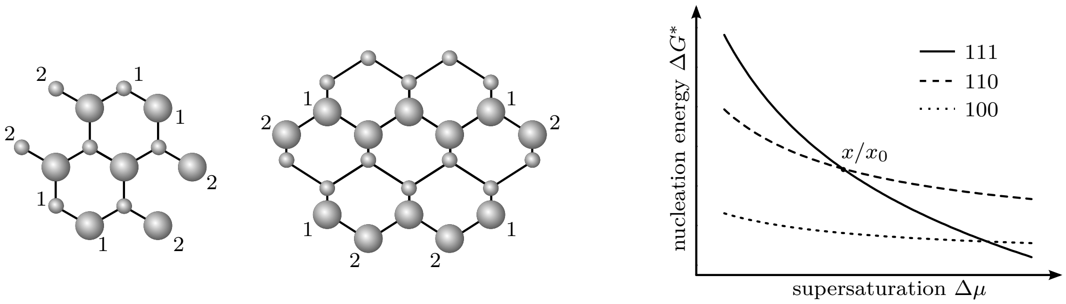

(a) **(b)**

Figure 5.15: 2D nucleation model according to Kramer et al.. (a) Shape of 2D nuclei on (111) and (110) surface (left and right respectively). Subjacent atomic layers are depicted by smaller circles. Numbers indicate additional unsaturated bonds at nucleus' edge. (b) Critical nucleation energy on different surfaces as a function of supersaturation.

in figure 5.16. According to Schwarz and Tersoff the growth velocity v_i of a facet i is proportional to the difference of the chemical potential of germanium inside the droplet and in the respective facet.

$$v_i \propto (\mu_l - \mu_i) \tag{5.1}$$

In general the chemical potential of germanium in two equivalent facets should be equal and thus growth velocities of the two (111) facets should be equal, too. This is true in the case of high supersaturation where the size of the respective facets has almost no influence on the difference of the chemical potential in the liquid and the solid. Therefore, the nanowire will maintain the initial growth direction, e.g. $\langle 111 \rangle$ (see fig. 5.16(a)).

In the case of low supersaturation, as it occurs in physical vapor deposition processes, the situation can change significantly. According to Schwarz and Tersoff, if the two $\{111\}$ facets have different sizes the smaller facet exhibits a higher curvature of the edge (smaller radius) resulting in a higher chemical potential μ_i leading to lower growth velocity. It should be generally noted, that fast growing facets shrink at the expense of slow growing ones. Therefore, the two facets always tend to be of the same size during growth at low supersaturation which highly stabilizes the $\langle 011 \rangle$ growth direction which is shown in figure 5.16(b).

It may be noted, that the existence of a nanofacet at the triple phase boundary as it is indicated in figure 5.16(a) has been found by Gamalski et al. [103]. However, they report on a small (011) facet which arises and disappears in an oscillatory fashion while the original growth direction remains unchanged.

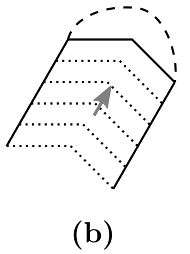
(a) (b)

Figure 5.16: NW growth model by Schwarz and Tersoff: (a) high supersaturation with the same growth velocity of small and bigger facets which maintains growth along ⟨111⟩ and (b) low supersaturation with different growth velocities of facets with different sizes leading to stabilization of growth along ⟨110⟩. Dashed lines indicate droplet. Dotted lines represent (111) faces of the growth front.

However, the described mechanism leading to different growth directions can not give any answer on the question why germanium behaves considerably different than silicon. Obviously, the distinct preference of germanium nanowires to grow along ⟨011⟩ directions while forming flat {111} side and top facets is energetically very stable under the described growth conditions. This is reasonable since the (111) surface exhibits the lowest surface energy and it seems clear that the total surface energy of side facets can be effectively lowered by forming such faces.

On the other hand, silicon nanowires exhibit a completely different side wall faceting although also (111) faces have the lowest surface energy for that material (see tab. 5.2). The question is: Why do silicon nanowires prefer a rather complicated sidewall faceting (sawtooth)? The answer could be given by taking a look at the wetting behavior of gold. As demonstrated in section 5.2.2 silicon is wetted slightly better due to higher surface energies compared to germanium. This finding coincides with observations made by Hertog and coworkers [104]. By careful TEM studies, they found the sidewalls of silicon nanowires to be decorated by lots of gold clusters which affirms the good wettability of silicon with gold. In terms of surface energy, wetting can be understood as kind of termination which lowers the total energy and stabilizes the surface. In other words, gold may act as an surfactant on silicon in contrary to germanium which therefore forms different side facets.

Unlike reported from many physical vapor deposition experiments (MBE), there are germanium nanowires grown on various (111)-oriented substrates along the [111] direction [105, 106]. The remaining question is, how this can be possible. The answer may lie in different growth processes. According to current state of research known from literature, ⟨111⟩ oriented germanium nanowires were obtained in the presence of a carrier gas which is commonly hydrogen in CVD processes using GeH_4 or Ge_2H_6. Hydrogen is able to saturate open bonds at the nanowire surface and thus reduces the specific surface or edge energy as it may happen due to gold wetting of silicon nanowires. This passivation process cannot take place in MBE growth on germanium under UHV conditions.

Consequently, growth while hydrogen is injected into the chamber could be a key in order to influence the growth direction. Thereby, the $\langle 011 \rangle$ direction seems to be energetically most stable and will maybe not be susceptible for any surfactant effect once it is established. Therefore, hydrogen may merely influence the growth at the beginning rather than during later stages of growth. In other words, a controlled kinking by means of hydrogen injection can not be expected in the frame of this hypothesis.

Both, an increase of the supersaturation of the droplet as well as the influence of the surface condition during the growth have been tested in a series of experiments. Increasing the supersaturation is basically possible by applying higher germanium rates for the growth. Accordingly, the germanium source temperature was increased up to the possible maximum of about 1400 °C which corresponds to $0.1\,\mathrm{nm\,s^{-1}}$, approximately ten times the rate at 1250 °C source temperature which was used for most of the experiments. However, no change in the growth direction has been observed in the covered parameter range so far. Further increase of the evaporation rate could be possible by electron beam evaporation (EBE) of germanium. Pecora et al. [107] reported on $\langle 111 \rangle$ grown germanium nanowires by EBE at significantly larger evaporation rates. However, they only found a small fraction of $\langle 111 \rangle$ grown nanowires with growth rates almost as low as the growth rate of epitaxial layer between the wires and with very low aspect ratio.

Due to the lack of hydrogen supply at the MBE chamber, first experiments have been carried out in which germanium and gold were co-evaporated during nanowire growth in order to reach a certain gold coverage in place of naturally wetting as observed on silicon. However, this approach did not show any change in the growth direction. Further experiments with hydrogen injected in to the chamber need to be done to clarify the role of hydrogen and the nature of directional growth.

5.3.4 Length–Radius relation of Ge nanowires

An important characteristic of nanowire growth is the length–radius relation. On the one hand, nanowire growth can be mainly influenced by thermodynamic aspects of such small structures which is known as Gibbs-Thomson effect which is described in detail in section 2.7.1. If nanowire growth takes place in such a regime, the growth rate is expected to decrease at smaller nanowire radius. On the other hand, material transport towards the metal droplet can lead to limitations of the growth rate. In such a regime which is driven by surface diffusion the growth rate is expected to increase with decreasing radius. Therefore, a length vs. radius plot can give important information to understand the nature of nanowire growth.

As described in the section above, germanium nanowires exhibit a rhombohedral cross section and therefore, the meaning of radius needs to be clarified. In the following, half of the width measured along the [1-1 0] direction (NW grown along [1 1 0]) which corresponds to one diagonal of the cross section is taken as the nanowire radius. This value can be determined from top-view SEM images and is used for the following measurements.

Nanowires grown on Ge(111) substrates were used for this study. The length was measured on the basis of SEM images considering that those merely provide a projection of the nanowires. Therefore, the measured values are divided by the sine of the inclination of nanowires (35.3°) to obtain their real length. The measured nanowire width can be assumed to be imaged correctly and was divided by two to obtain the nanowire radius eventually. The analyzed SEM micrographs were recorded at 20.000-fold magnification with a distance per pixel of 3.12 nm which therefore gives the accuracy limit of the measurements.

Nanowires have been analyzed in the range between 43 nm and 88 nm. Figure 5.17 shows the plot of length against width, which indicates an increase of the nanowire length with decreasing radius. As a consequence, germanium nanowire growth by MBE can be considered as being dominated by material transport towards the metal droplet, which is important to be noticed to understand temperature dependence of the growth which is presented in the next section.

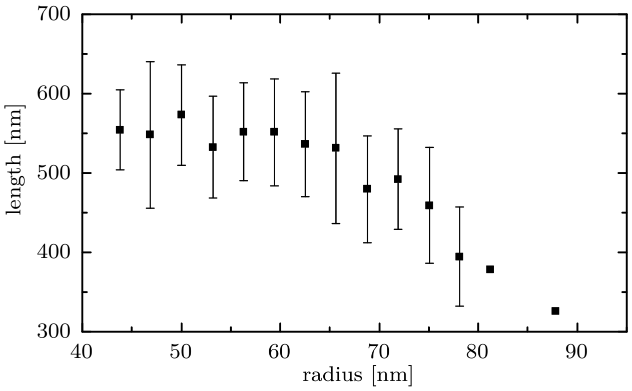

Figure 5.17: Length–width relation of Ge NW grown on a Ge(111) substrate. Accuracy was limited by the 3.12 nm distance per pixel of the analyzed SEM images.

5.3.5 Temperature dependent growth

As described in section 2.6 MBE growth is dominated by diffusive material transport of the growing species. A growth model based on surface diffusion effects has been introduced in section 2.7.2 which describes the contribution of diffusing atoms on the nanowire growth rate. Experiments have been carried out at temperatures varying from 370 °C to 510 °C while remaining all other experimental conditions constant to investigate the influence of germanium surface diffusion on the average growth rate of nanowires. The total deposited amount of germanium was chosen to be small (46 nm) in order to avoid the formation of a closed epi-layer on the substrate. This makes it possible to measure the length of nanowires without the need to determine any thickness of an epi-layer.

Extensive SEM studies have been done to determine the average nanowire length for various samples. The experiments have been carried out on Ge(111) substrates where the nanowire length can be determined in the same manner as it is described in section 5.3.4. Figure 5.18(a) shows the measured nanowire length while error bars represent the standard deviation of the values. The data show an increase of the length with temperature until a maximum is reached at 430 °C. Higher temperatures result in shorter wires until no nanowire growth could be observed above 510 °C. The length ranges from 220 nm to 305 nm, which is up to 6 times larger than the nominal layer thickness equal to 46 nm.

This growth characteristics can be well explained by various aspects of diffusive material transport both on the substrate and along the nanowire sidewalls. At lower temperatures, the characteristics is governed by a competition between nanowire growth and island nucleation where nanowire growth is more favourable at increasing temperatures. On the other hand desorption reduces the effective surface diffusion length with increasing temperature which dominates the characteristics at elevated temperatures. Details can be found in section 2.7.2 where kinetic aspects of nanowire growth are explained.

Fitting the model

In the frame of the diffusion model the final nanowire length can be calculated as a function of the substrate temperature. Therefore, the final equation (2.49) which describes the nanowire growth rate can be applied to fit the growth results. By solving the differential equation $dL/dt = f(L, parameters)$ for L where parameters are a set of variables that occur in equations (2.49), (2.52) and (2.51) the corresponding nanowire length can be obtained. Most of the parameters can be determined from experiments. Table 5.5 shows the list of parameters that have been considered to remain constant for every data point in figure 5.18(a). Thereby, areal density of islands as well as areal density and radius of nanowires have been obtained from SEM image analysis. The average nanowire density N_w is of the order of $1 \times 10^{12}\,\mathrm{m}^{-2}$, which corresponds to the droplet density determined by atomic force microscopy at samples without germanium deposition.

In a fitting routine, equation (2.49 with temperature dependent λ_s and λ_w is solved for every iteration step while the parameters that are unknown, namely λ_0, F_s and G_s are optimized to fit the diffusion model to the measured data. A Maple™ script was written to perform the entire calculation including solution of the ordinary differential equation and a subsequent fitting routine which applies a Gauss-Newton algorithm.

As shown in figure 5.18(a) (solid line), the model fits the measured data well with a RMS of the residuals of 24 nm. The fitted parameters obtained by the calculation are listed in table 5.6 where $\lambda_0 = 126\,\mathrm{nm}$ refers to a free surface at a temperature $T_0 = 430\,^\circ\mathrm{C}$. With this, the diffusion length on the substrate λ_s as well as the diffusion length on the nanowire sidewalls λ_w at 430 °C can be calculated according to eqn. (2.51) and (2.52): $\lambda_s = 103\,\mathrm{nm}$, $\lambda_w = 126\,\mathrm{nm}$.

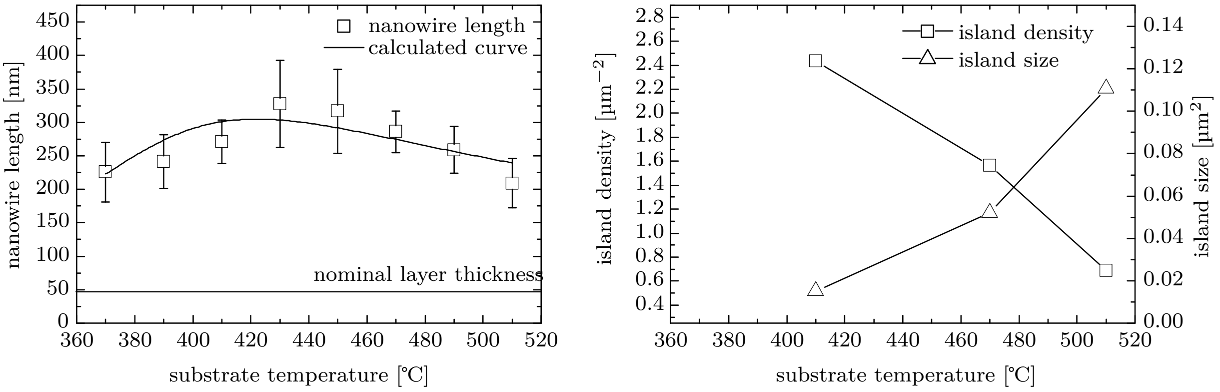

(a) **(b)**

Figure 5.18: (a) Results for NW length vs. substrate temperature from experiments and calculations. Open squares indicate the measured nanowire length after 1 h of growth and with nominal layer thickness of 46 nm. The solid curve shows the calculated dependence of wire length on temperature using the parameter values from the fit procedure. Error bars indicate the standard deviation from the statistical analysis of the individual nanowire length. (b) Temperature evolution of island size and density. Squares indicate the island density N_i whereas triangles show the measured island size.

As a result, Ge surface diffusion towards the gold droplets has to contribute to nanowire

variable	symbol	value
impingement rate substrate	R_s	$5.7 \times 10^{17}\,\mathrm{m}^{-2}\,\mathrm{s}^{-1}$
impingement rate nanowire	R_w	$R_s \sin(35.3°)$
NW radius	r_w	60 nm
reference temperature	T_0	430 ℃
NW areal density	N_w	$3 \times 10^{12}\,\mathrm{m}^{-2}$
island areal density at T_0	$N_{i,0}$	$1.5 \times 10^{12}\,\mathrm{m}^{-2}$

Table 5.5: Experimentally determined parameters for the fitting routine which is described in the text.

fit parameter	symbol	value
diffusion length	λ_0	126 nm
parameter for island formation	F_s	11.6
parameter for desorption	G_s	4.8

Table 5.6: Parameter obtained from fitting the kinetic growth model to the measured data.

growth to a large extent and needs to be considered not least because the nanowire length is considerably larger than the corresponding layer thickness of deposited material. Furthermore, the temperature evolution of the final nanowire length can be described well by surface diffusion phenomena including island formation on the substrate and desorption.

Beside an increase of the diffusion length with temperature according to the Arrhenius equation, the deposited Ge does not only contribute to the growth of nanowires but also to the formation of islands between them which can capture diffusing adatoms. This results in a lower effective diffusion length. The density of those islands is a function of temperature and decreases with increasing temperature, which implies that the reduction of the diffusion length by capturing effects becomes less important. This explains increasing growth rates with rising temperatures up to 430 ℃. The decrease of the nanowire growth rate at temperatures higher than 430 ℃ can be explained by surface diffusion effects, too. Beyond 430 ℃, desorption becomes more likely and adatoms detach from the substrate before they can be incorporated into any nanowire.

Island formation

Additionally, island formation has been evaluated on selected samples by measuring island size and areal density as a function of temperature. Therefore, spontaneously nucleated islands (without the influence of gold droplets) which show characteristic triangular shape (according to threefold rotational symmetry of Ge(111) surface) have been surveyed and dimensioned by SEM. Figure 5.18(b) shows the resulting average island sized at different temperatures. As can be expected from nucleation theory (described elsewhere, [40, sec. 2.2.9.2]) the areal density of islands decreases with increasing temperature while the average size (area) of individual islands increases. This finding has been directly involved in the kinetic growth model to describe the effective diffusion length as a function of the areal density of already formed islands N_i on the substrate. A dynamic examination of island formation during nanowire growth which considers time evolution of island density and size has not been carried out in the scope of this investigation.

Influence of Desorption

Further experiments have been carried out to check the rising influence of desorption with increasing temperature. Therefore, germanium was deposited at 370 ℃ and 510 ℃ using the same deposition rate as it has been applied for nanowire growth, but without previous gold evaporation. Any difference in the resulting layer thickness is therefore caused by different desorption rates at the two temperatures. Long evaporation time is needed to make the loss of material upon desorption detectable. For the sake of good comparability, the same type of substrates as for the temperature dependent growth experiments have been used. Another advantage of using Ge(111) substrates consists of better island growth compared to heteroepitaxy of germanium onto silicon substrates, for instance. On the other hand, some difficulties arise when determining the layer thickness. Optical or X-ray based techniques that provide thickness measurement, e.g. ellipsometry or XRR, typically exploit any change in material properties such as refractive index or density. This is not the case if germanium is deposited onto germanium substrates. Therefore a mask made of molybdenum was constructed with a $19 \times 19\,\mathrm{mm}^2$ opening in which the deposition on the substrate takes place. Figure 5.19 shows the experimental setup in detail. Germanium is deposited onto a defined area on the substrate which makes it possible to determine the layer thickness by weighing with a precision analytical scale. Thus, the change in mass can be correlated with the layer thickness. Another method to determine the thickness is by measuring the profile of the edges which form at the rim of deposited area.

Experiments have been carried out on Ge(001) substrates which were deposited for 10 h 51 min at the same deposition rate as it was applied for nanowire growth.

The total mass of samples was measured using a *Mettler AT20* precision scale directly

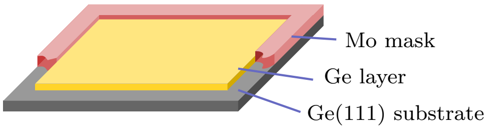

Figure 5.19: Molybdenum window defining the deposited area on the substrate.

temperature	mass increase	layer thickness
370 °C	520 µg	271 nm
510 °C	502 µg	262 nm
	18 µg	9 nm

Table 5.7: Effect of desorption on the final layer thickness. The last row gives the difference between the first two rows.

after wet chemical substrate termination and after the deposition, respectively. The scale provides a sensitivity down to 2 µg with a reproducibility of 3 µg. The difference in total mass has been determined for three samples of the same kind and yielded an error of about 5 µg. The results corresponding to growth temperatures of 370 °C and 510 °C are presented in table 5.7. Using $\Delta d_{Ge} = \Delta m_{Ge}/(19 \times 19\,\mathrm{mm}^2 \varrho_{Ge})$, where ϱ_{Ge} is the mass density of germanium, the derived difference of the layer thicknesses is therefore about 9 nm.

Furthermore, the difference of desorption rate at 370 °C and 510 °C can be calculated as follows: A 9 nm layer with a total area of $19 \times 19\,\mathrm{mm}^2$ contains $N_{Ge} = (9\,\mathrm{nm} \cdot 19 \times 19\,\mathrm{mm}^2) N_A / \mathcal{V}_{Ge} = 1.44 \times 10^{17}$ atoms, where $\mathcal{V}_{Ge} = 13.63 \times 10^{-6}\,\mathrm{m}^3\,\mathrm{mol}^{-1}$ is the molar volume of germanium. The resulting difference in the desorption rate finally amounts to

$$\Delta W_{des} = \frac{N_{Ge}}{At} = 1.02 \times 10^{16}\,\frac{1}{\mathrm{m}^2\,\mathrm{s}} \tag{5.2}$$

The total amount of germanium atoms which desorb within 1 h from a sample at which nanowires have been grown can be approximated as follows while the nanowire length as a function of time is kept constant at an average length $l_w = 250\,\mathrm{nm}$ for simplicity.

$$\Delta N_{Ge} = (A_0 + N_w A_0\, 2\pi r_w l_w)\, t \Delta W_{des} = 1.51 \times 10^{16} \tag{5.3}$$

Here the values have been taken from table 5.5 while A_0 gives the processed sample area equal to $19 \times 19\,\mathrm{mm}^2$ in the present case and the second summand in the brackets represents additional area, i.e. summed lateral area of the nanowires. The change of the nanowire length caused by ΔN_{Ge} atoms is than given by

$$\Delta l_w = \frac{1}{N_w A_0} \frac{\Delta N_{Ge} \mathcal{V}_{Ge}}{N_A \pi r_w^2} = 56\,\mathrm{nm} \tag{5.4}$$

This result can be seen as an upper limit for the difference of the nanowire length. Nevertheless, the effect of desorption could be demonstrated by comparatively simple experiments. Keeping in mind, that nanowire growth is much more influenced by desorption due to the high surface to volume ratio of nanowires it seems to be clear that desorption is an important process which can limit the nanowire growth rate at higher nanowire length and elevated temperatures. In other words, desorption reduces the effective diffusion length and thus the nanowire growth rate.

In addition, the experimental setup allows determination of the layer thickness by measuring edge profiles of the deposited area with a profilometer. However, the opening of the mask did not provide a sufficiently well defined edge which causes blurring of the profile. Furthermore, minor vibrations coming from the substrate rotation during growth caused movement of the Mo mask within the substrate holder which causes double or multiple steps at one edge. Another obstacle of those measurement is substrate curvature and corrugation which makes data manipulation necessary after the measurement. Different ways of flattening the data have been tested, e.g. measuring the substrate prior to deposition or polynomial fitting to subtract the substrate influence from the measurement. However, the reproducibility of the results was insufficient which lead to large errors such, that the deviation exceeded the value of the layer thickness which was expected of the order of 10 nm. Figure 5.20 shows an example that illustrates difficulties in the interpretation of those measurements and as a consequence, those measurements have not been used to verify the effect of desorption.

5.3.6 Germanium nanowires on silicon substrates

As described above, germanium nanowire growth is accompanied by the formation of an epitaxial layer between the nanowires. This is typical for physical vapour deposition as the evaporated material is deposited all over the substrate and not selectively at the catalyst droplets. Nucleation and growth of this layer strongly depend on the underlying substrate and the diffusion thereon. If material nucleates soon after it impinges on the surface the atoms can not diffuse towards the droplet to contribute to nanowire growth.

Changing the surface properties, e.g. by functional layers, in a way that diminishes or even prevents nucleation between nanowires could be a possible pathway to facilitate

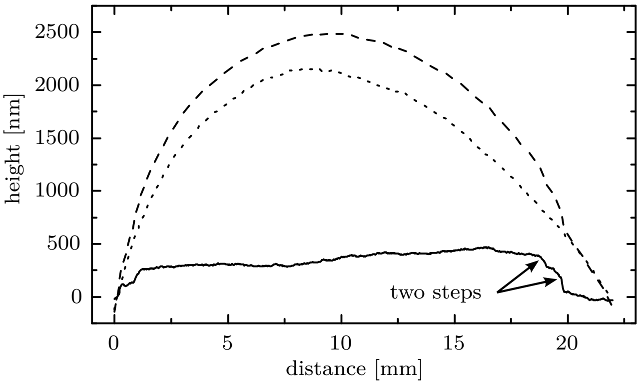

Figure 5.20: Ge layer profiles. Dashed line corresponds to substrate with Ge layer on top while dotted line shows measurement of bare substrate. Strong curvature and corrugation can be seen. Solid line shows extracted data for the layer. Edges appear not sharp and show multiple steps. Increasing layer thickness from the left to the right can be considered to be an artifact since samples are rotated during the growth.

nanowire growth.

As such, growing germanium nanowires onto silicon substrates provides a relatively simple way to improve diffusion properties of germanium. It is well known, that silicon oxide exhibits significantly lower activation energies for diffusion and desorption compared to silicon. Values for activation energies found in literature are presented in table 5.8. Therefore, oxidizing the silicon substrate after droplet formation could effectively enhance diffusion between the droplets while the latter mask the underlying substrate where nanowires are supposed to grow.

Oxidation of the silicon surface after droplet formation could be done by taking the sample out of the UHV chamber and keeping it for a few hours under ambient air. However, in addition to the time consumption of this approach the sample surface becomes contaminated again by dust, water or carbon compounds.

Another approach is in-situ oxidation by injecting oxygen directly into the MBE chamber. As annotated in figure 3.2, the MBE chamber is also equipped with an oxygen cracker cell. Oxygen is injected into the cell and passes a hot filament such that oxygen molecules are cracked thermally. Cracking efficiency of up to 70% can be achieved depending on cell temperature and oxygen flux.

By adjusting the oxygen flux with a feedback loop using the oxygen partial pressure as the process value a constant oxygen partial pressure of up to 3×10^{-8} mbar can be established with a O/O_2 ratio of about 1/10 which can be increased at lower oxygen throughput. The real flux from the source to the substrate has not been measured in the

surface	E_{dif}	E_{des}
Si	$0.676 \pm 0.03\,\mathrm{eV}^{a}$	—
SiO_2	$0.24 \pm 0.05\,\mathrm{eV}^{b}$	$0.44 \pm 0.03\,\mathrm{eV}^{b}$

Table 5.8: Activation energies for diffusion and desorption of germanium on silicon. Footnotes *a* and *b* correspond to references [108] and [109] respectively.

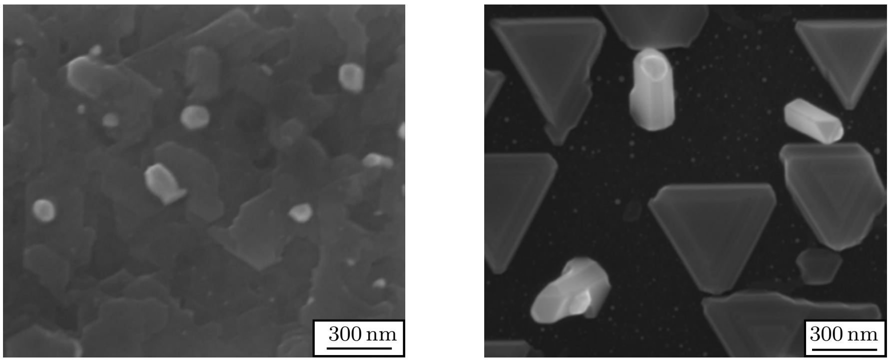

(a) **(b)**

Figure 5.21: Ge NW on Si(111) substrates. (a) A sample which did not undergo oxidation after droplets have formed. (b) Same process including the oxidizing step.

scope of this work due to a lack of an appropriate flux monitor.

In order to demonstrate the effect of in-situ oxidation after the gold droplets have formed, two Si(111) substrates have been prepared by means of SC-1 followed by an HF-dip as described in section 3.2.2.

Prior to growth, the samples were heated up to 900 °C for 1 h to remove silicon oxide that may has remained after the chemical treatment or has formed on the way to the UHV system. In the next step, gold droplets are created in the same way it has been done on germanium by depositing 1 nm of gold at a substrate temperature of 450 °C. Subsequently, only one of the substrates underwent the in-situ oxidation process in which an oxygen partial pressure of 2×10^{-8} mbar was maintained for 20 min at a substrate temperature of 450 °C. Eventually, germanium was deposited at the same substrate temperature and a deposition rate of $0.025\,\mathrm{nm\,s^{-1}}$ for 1 h to grow the nanowires.

The samples were characterized by means of SEM which is presented in figure 5.21. As can be seen in figure 5.21(a), no nanowire growth is observed on the non-oxidized sample while a homogeneous epitaxial layer has grown between the droplets. In contrary, nanowires have been successfully grown accompanied by growth of separated islands in between which is presented in 5.21(b). Although the substrate was supposed to be oxidized outside the droplets, the observed islands are in epitaxial relation with the

Si(111) substrate as they show the same orientation. This can be explained as follows. The created oxide is supposed to be rather thin and may thus provides pinholes which enable epitaxial growth inside. Such pinholes have been observed in silicon oxide layers up to 30 nm thick [110]. Once an island has nucleated in such a pin hole, it serves as place of preferred attachment of further atoms that are diffusing on the surrounding silicon oxide which may lead to lateral overgrowth. Further research is needed in order to confirm this hypothesis, e.g. by means of TEM studies. Nevertheless, it could be demonstrated that surface modifications like oxidation change the growth behaviour tremendously. As expected, the growth of a homogenous epi-layer could be diminished while germanium nanowires have been grown successfully at the same time. Further experiments are needed in order to find the best process parameters to create a well oxidized surface between the droplets which effectively suppresses epitaxial growth.

5.4 In-plane growth

Next to the formation of conventional nanowires and islands another morphology has been observed. So-called in-plane nanowires have been found which also grow via the VLS mechanism but parallel to the substrate along the surface.

Once germanium nucleates inside a droplet, the latter seems to glide off onto the substrate and starts to be pushed aside as the the in-plane nanowire grows further. The growth scheme is depicted in figure 5.22. As those structures occur under the same conditions as conventional nanowires are grown, in-plane growth might have its seeds in certain characteristics of the underlying substrate like roughness or the presence of adsorbates which could come from the wet-chemical treatment. It turns out, that the quality of surface passivation plays an important role for the growth of in-plane nanowires as will be described in the next sections. More than that, an appropriately passivated germanium surface favors in-plane instead of vertical nanowire growth which is rather suppressed after wet-chemical passivation. Furthermore, preferred growth directions, similar to conventional nanowires, have been identified on differently oriented germanium substrates.

5.4.1 Morphology and growth direction of in-plane nanowires

As explained in section 5.3.1 conventional Ge nanowires grow along $\langle 011 \rangle$ directions preferentially by MBE. To investigate, if similar behavior can be found also in the case

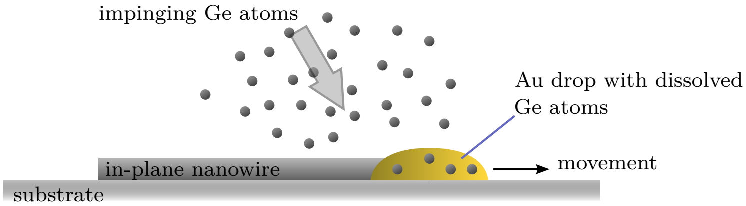

Figure 5.22: Growth scheme for in-plane NW according to VLS mechanism.

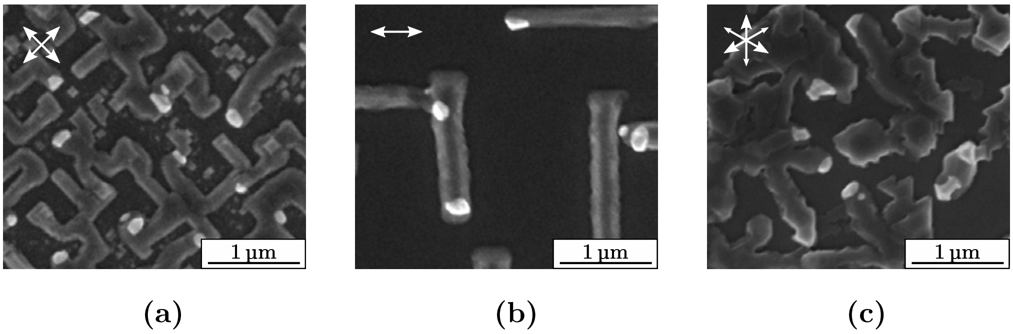

(a) **(b)** **(c)**

Figure 5.23: Top view SEM micrographs showing growth directions of in-plane NW on (a) Ge(001), (b) Ge(011) and (c) Ge(111). The arrows in upper left corner of each image indicate possible ⟨011⟩ growth directions and represent the symmetry of respective surfaces.

of in-plane growth where the influence of the substrate is expected to be significant, experiments on Ge(001), Ge(011) and Ge(111) have been carried out.

Each of the three substrate orientations provides a certain number of equivalent ⟨011⟩ in-plane directions according to the symmetry of the respective surface. Ge(001) and Ge(011) exhibit a fourfold and a twofold rotational symmetry, respectively. The situation is different on Ge(111) which provides six ⟨011⟩ directions but only a threefold rotational symmetry which means that only every second of those directions is equivalent.

Indeed, the results presented in figure 5.23 show preferential growth along ⟨011⟩ similar to conventional nanowires on Ge(001) and Ge(011). Also, the (111) faceting which is already known from vertically grown wires (section 5.3.1) is very distinctive and thus leads to different shapes of resulting in-plane structures according to the orientation of formed {111} faces. The situation is different on Ge(111). According to the threefold rotational symmetry, less straight in-plane growth is observed on Ge(111) but rather sequences of triangular shaped islands roughly along ⟨112⟩ directions that are determined by the tips of triangles. Thus it seems difficult to form straight wires with high aspect ratio on the basis of triangular shaped islands.

However, the most surprising issue of those investigations is distinctive ⟨001⟩ growth on Ge(011) as can be seen in figure 5.23(b) where perpendicular oriented nanowires grew along this direction. These nanowires also grow straight in a somewhat guided fashion similar to those which grow along ⟨011⟩. Therefore, the following investigations and explanations are restricted to this kind of in-plane nanowires. To investigate the morphology of those structures more in detail, they have been measured by AFM in order to image their cross section as well as any top facets. The {111} faceting turns out to be dominant for both of the observed growth directions as a triangular (roof-like) shape has been found for ⟨011⟩ grown nanowires while a nearly rectangular cross section is observed for ⟨001⟩ grown ones. The measured geometry of those structures is depicted in figure 5.24. Roof-shaped in-plane nanowires (fig. 5.24(a)) mainly consist of two flat facets which comprise an angle of about 105° measured by AFM which merely slightly deviates from the theoretical value of 109.5° (comparable to v-shaped tip of conventional nanowires in section 5.3.1). In contrast, ⟨001⟩ grown in-plane nanowires exhibit corrugated top and side facets which is demonstrated by the top facet profile in figure 5.24(b). Analyzing the angles comprised by these nanofacets yields {111} faceting as well. This finding, once again, affirms the strong and distinct {111} faceting which is observed on germanium structures that form upon VLS process by means of MBE. In this sense, in-plane nanowires growing within ⟨001⟩ direction seem to consist of a series of consecutive roof-shaped islands. Obviously, the VLS growth causes top and side faces to form alternating nanofacets in order to minimize the total surface energy of droplet but also the interface energy between droplet and wire. In this sense, the surface tension of the gold droplet can be understood as driving force for guided growth along ⟨001⟩ directions on Ge(011).

Additionally, detailed SEM and TEM studies of in-plane nanowires have been carried out in the working group Si/Ge nanostructures at IKZ which are presented in [111].

5.4.2 Effects of surface passivation on the in-plane growth

As explained in section 3.2.2 four different types of passivation have been applied during wet-chemical substrate preparation prior to MBE growth. In general, in-plane growth only occurs on extremely flat surfaces with no hinderance caused by imperfections of the substrate. It may be noted, that the tendency of in-plane growth has already been observed in section 5.2.1 where droplets begin to crawl along the substrate during their formation on previously passivated substrates. An experimental series on Ge(011) substrates has been conducted to investigate the influence of different types of passivation on in-plane growth. The substrate orientation has been chosen because it exhibits merely two oppositely oriented ⟨011⟩ crystallographic directions which are preferred by in-plane nanowires.

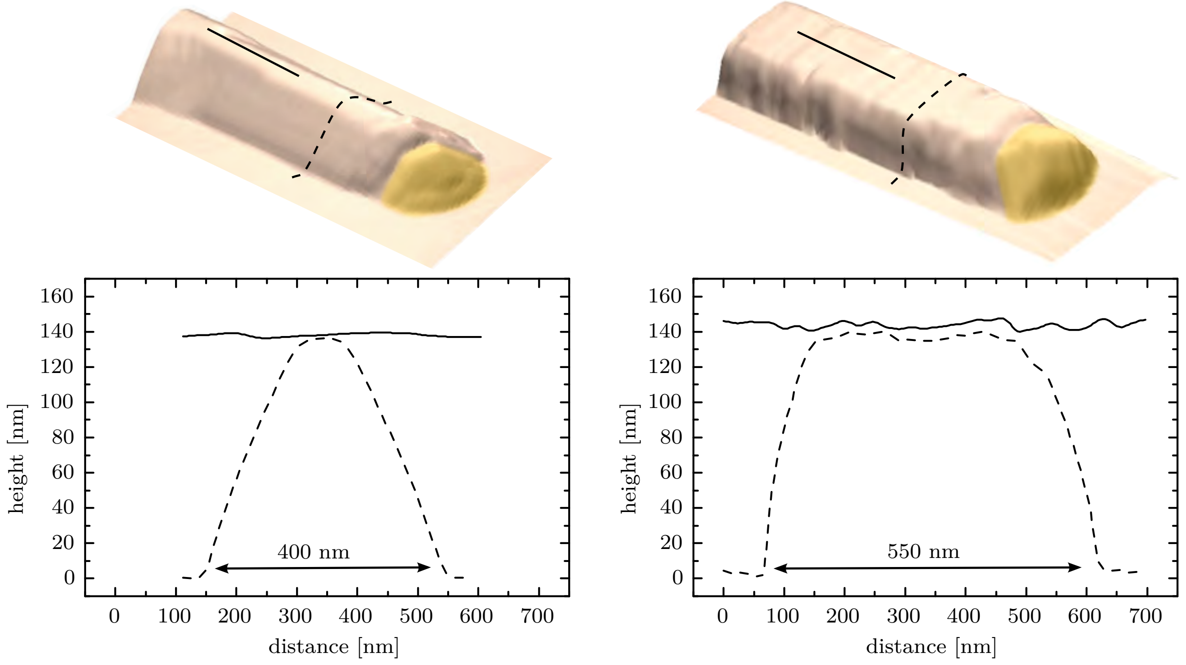

(a) **(b)**

Figure 5.24: Shape and faceting of in-plane nanowires. (a) grown allong ⟨011⟩ and (b) grown along ⟨001⟩. The profiles are measured along the respective lines indicated in the 3D images where solid lines indicate profiles along the growth direction and dashed lines correspond to cross-sectional profiles.

The results are presented in figure 5.25 showing SEM images of samples grown under the same conditions but with different surface termination prior to growth. Rectangular and line-shaped structures are visible with varying rations of ⟨011⟩ and ⟨001⟩ growth. There is a significant fraction of ⟨001⟩ grown nanowires on hydride and chloride passivated samples whereas samples which are bromide and sulfide passivated exhibit considerably less ⟨001⟩ growth. In fact, no such structures have been observed for sulfide passivation. Instead, the whole surface was covered with in-plane nanowires grown along ⟨011⟩ direction.

These results were unexpected and required additional analysis for deeper understanding. Therefore, the number of nanowires grown along ⟨001⟩ compared to the total number of in-plane nanowires has been evaluated by analyzing SEM images. The results are summarized in table 5.9. Having the stability of different applied passivations in mind (see sec. 3.2.2) it is apparent that the fraction of in-plane nanowires growing perpendicular to preferred ⟨011⟩ directions becomes less as the stability of the passivation increases. Thus, ⟨001⟩ growth may indicate regions where passivation started to degenerate and reoxidation already occurred.

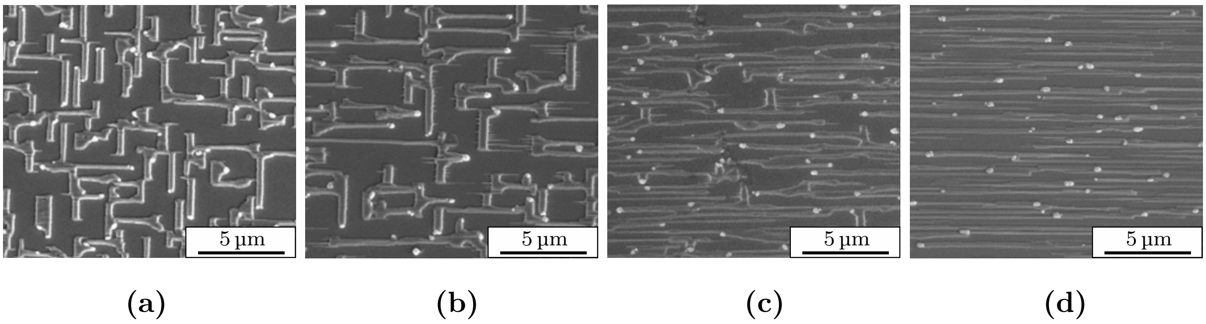

Figure 5.25: SEM micrographs showing the effect of different surface passivations on in-plane NW growth: (a) hydride, (b) chloride, (c) bromide, (d) sulfide. Growth took place on Ge(011) substrate. ⟨011⟩ directions are aligned horizontally and ⟨001⟩ are aligned vertically.

passivation	⟨001⟩-grown NW
hydride	59%
chloride	48%
bromide	15%
sulfide	0%

Table 5.9: Fraction of ⟨001⟩-grown NW compared to the total number of in-plane NW.

In order to check this hypothesis, bromide and sulfide passivated substrates have been oxidized by keeping them in ambient air under clean room atmosphere for 48 h before further processing in the MBE. As a result, ⟨001⟩ growth was observed much more often than on freshly passivated substrates which becomes clear by comparing figure 5.25 and 5.26. Apparently, reoxidation plays an important role and causes altered germanium surfaces compared to the non-oxidized case. The true nature of the alteration could not be clarified in the scope of this work as the impact in the growth was utilized to get an insight on the effect of passivation and oxidation.

Further investigations need to be done to clarify the true nature of any alteration e.g. by intentional oxidizing and desorption inside the MBE chamber in order to detect any measurable corrugation of the surface upon this treatment directly by analyzing RHEED intensity or by AFM measurements.

These results show that germanium can be grown in various morphologies, not only layer or conventional nanowires are observed but also in-plane nanowires. This kind of nanowires have also been reported for silicon or gallium nitride [112, 113]. Reportedly, random growth directions are found in the case of silicon where experiments have been carried out on amorphous layers. This is reasonable given the fact that a transition from amorphous to crystalline silicon takes place where no preferred crystallographic direction

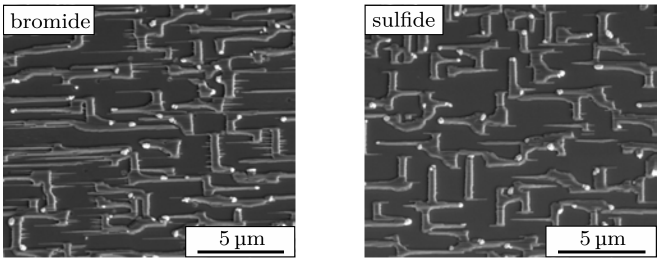

(a) **(b)**

Figure 5.26: SEM micrographs showing the effect of reoxidation on in-plane NW growth on previously (a) bromide and (b) sulfide passivated substrates.

is present as it is demonstrated by Heimburger et al. [114]. In the case of gallium nitride growth was carried out on crystalline but prestructured sapphire substrates which results in a guided growth.

In contrary, germanium in-plane nanowires grow also in a guided way but without any prestructuring. Instead, available growth directions are given by the underlying substrate symmetry. Thereby, also a change in the growth direction from ⟨011⟩ to ⟨001⟩ has been observed which is unique according to the current knowledge.

The phenomenon of in-plane nanowire growth might be known for quite a long time but has attracted more and more attention in recent years due to the fact that it may provide a possibility to simplify the manufacturing of electronic or optoelectronic structures, e.g. a transistor channels, by guided growth rather than by costly lithography methods.

5.5 Catalyst removal

Nanowires, not only made from germanium, are promising structures for manyfold applications. However, most of the application areas may require a removal of gold from the sample surface which is still the most common catalyst material. Therefore, a selective method is needed to remove gold exclusively without damaging nanowires too much.

Commonly, wet-chemical methods can provide good selectivity by applying etching processes, but etching gold as a noble metal requires a strong etchant which possibly attacks also the nanowires. A common etching solution for gold is so-called aqua regia, an aqueous solution of HNO_3 and HCl. However, this etchant reacts with germanium which leads to a strong damage of nanowires and finally leads to total dissolution of them [115]. An alternative agent that is able to dissolve gold is the triiodide etch which is aqueous solution of I_2 and KI. According to Ratchford et al. it effectively etches

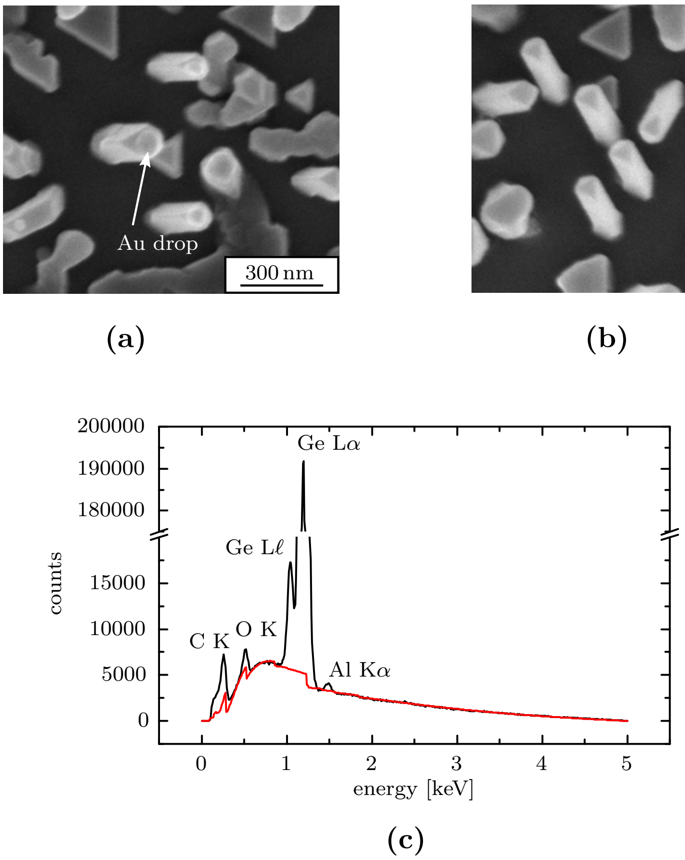

Figure 5.27: SEM analysis of gold removal. SEM micrographs show Ge NW before (a) and after (b) gold etching in aqueous I_2/KI/HCl. Au drops can be clearly seen in (a) while they are absent in (b). EDX spectrum (c) of the sample in (b) indicates no Au emission. Black curve corresponds to spectrum as recorded while the red curve shows the background of the measurement. Al Kα emission originates from the Al holder which is excited by secondary processes and stray radiation.

gold but also damages germanium nanowires remarkably. However, the etching rate of germanium seems to be slow such that no complete dissolution of nanowires has been observed. They found that adding HCl to triiodide etch slows down the germanium etch rate while the mechanism is not fully understood. Presumably, chlorine passivates the germanium surface such that the latter is protected against the etching process.

These finding have been successfully adopted in order to establish a process for catalyst removal from germanium nanowires. The results are presented in figure 5.27 were SEM micrographs are shown which were taken before and after the removal process. No droplets were observed after gold etching while germanium nanowires were still intact and no damage of them has been found. EDX spectra have been recorded to confirm the absence of gold which is shown in figure 5.27(c). No gold emission has been detected which typically arise at 9.71 keV (Au Lα) and 2.12 keV (Au Mα). Nevertheless, traces of gold may still remain on the samples given the fact that EDX provides a detection limit of about 0.1 wt.%.

5.6 Embedding nanowires

Embedding nanowires in an insulating matrix has been done by spin coating samples with HSQ after MBE growth (for details on HSQ see sec. 3.4). After spin coating HSQ has to be cured in order to transform the cage-like structure into a net-like one. Since this is usually done by electron beam lithography, experimental parameters for curing have to be determined, e.g. relation between rotational speed while coating and layer thickness or relation between curing temperature and degree of transformation. Furthermore, appropriate methods have to be found to characterize the structural transformation and to measure the layer thickness.

5.6.1 HSQ layers on bare substrates

HSQ is known as a high contrast resist for electron beam lithography [78]. Thus, it is not well established for embedding purposes which makes some basic characterization necessary to get an insight into properties such as layer thickness as a function of rotational speed or structural transformation upon curing. First experiments have been carried out on bare silicon substrates. HSQ layers are spun on at various rotational speeds and are cured subsequently including soft bake on a hot plate at 250 °C followed by hard bake under nitrogen atmosphere at temperatures up to 700 °C.

As described in section 3.4, the structural transformation comes along with specific changes in FTIR spectra of the layer. Therefore, layers without any baking have been compared with layers that were cured at 700 °C for 1 h. The corresponding FTIR transmission spectra are presented in figure 5.28.

A comparison with table 3.5 reveals coexisting cage and net structures in the non-cured sample since all listed absorption bands are found in the spectrum.

The spectrum of the cured sample shows no absorption bands which correspond to any H−Si bonding. Those bonds obviously dissociate due to baking and gaseous hydrogen forms during the process. A comparison of remaining absorption bands in the spectra which correspond to ν(Si−O−Si) stretching modes shows a change of the structural composition of the layer. While absorption at 1030 cm^{-1} which is typical for the cage

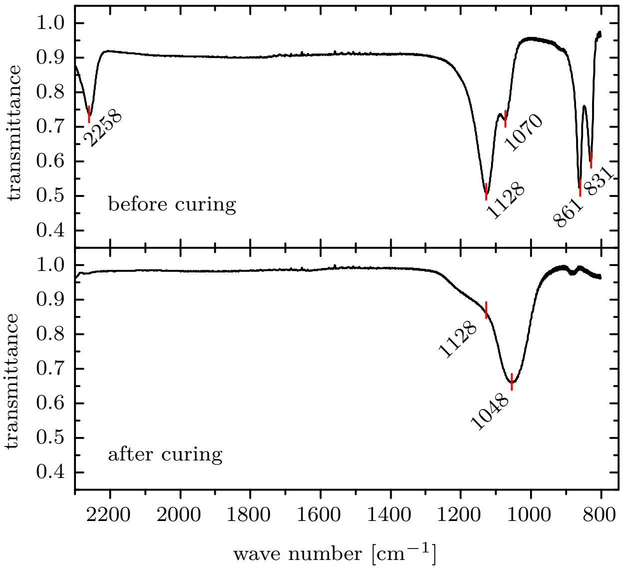

Figure 5.28: FTIR spectra of HSQ layers before annealing (top) and after 1 h annealing at 700 °C under nitrogen atmosphere. Spectra are normalized and the substrate signal has been subtracted. Centers of absorption lines are marked by red strokes.

structure decreases upon curing, the opposite is the case for absorption bands around $1070\,\mathrm{cm}^{-1}$ which are typical for net structure. According to Siew et al. the dissociation of H−Si bonds leads to formation of $SiO_{4/2}$ units which is accompanied by a change from cage to net structures [116]. The results correlated well the expectations and the structural changes could be successfully monitored by FTIR measurements.

However, due to device limitations of the FRIT spectrometer the transmitted spectra are recorded without measuring reflection at the sample surface or at the interface between layer and substrate. Therefore, a quantitative analysis of the spectra is not advisable and may lead to wrong results. In other words, the degree of transformation can not be estimated by the given spectra. To get further insight into the transformation and their influence on physical properties of the layer such as thickness or optical parameters, ellipsometry provides the necessary capabilities for further characterization. The evaluation of ellipsometric measurements is carried out on the basis of a model for the layered structure of the sample. Typically, layer thickness is required to gain the optical constants or vise versa in order to fit the model with measurement. For the present samples, the model consists of the underlying substrate covered with the HSQ layer approximated by SiO_2 with a 5 nm layer ontop containing voids which simulates the roughness of the spun on HSQ.

The model has been validated by reference measurements of the layer thickness by means of XRR. Therefore, a germanium substrate has been applied in order to ensure

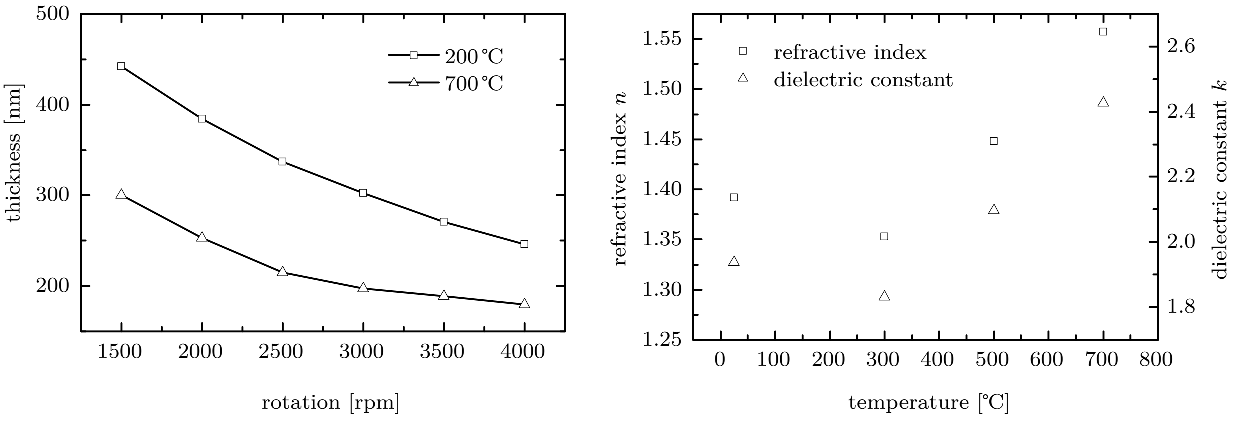

(a) **(b)**

Figure 5.29: Properties of HSQ layers. (a) Thickness of a function of rotational speed before and after hard bake. (b) refractive index measured after curing at different temperatures.

well pronounced oscillations in the XRR scan. It turns out that XRR (230 nm) and ellipsometry (226 nm) measurements agree sufficiently to determine HSQ thickness by means of ellipsometry in the following.

The resulting layer thickness is basically a function of the rotational speed at given viscosity of the liquid and wetting behavior on the respective substrate. HSQ thickness before (soft bake only) and after curing (including hard bake) was determined for various samples which have been prepared at rotational speeds in the range from 1500 rpm to 4000 rpm. The measured thickness decreases at higher rotational speeds as the centrifugal forces more and more spread the fluid over the substrate. It ranges from 450 nm to 250 nm. The measurements were repeated after curing. The values turn out to be 60-70% lower according to the collapse of the cage structure during the transformation process. The results are presented in figure 5.29(a).

Another sample series was prepared to investigate the change of optical parameters of HSQ depending on the curing temperature. Baking was carried out at 300 °C, 500 °C and 700 °C for 1 h. The results are depicted in figure 5.29(b). The values of refractive index and dielectric constant exhibit the same trend which is obvious since n is approximately $\sqrt{k}$ for transparent media at optical frequencies. Interestingly, the values decrease until a minimum at around 300 °C is reached and increase rapidly at higher temperatures. This behavior seems to be characteristic for the structural transformation. According to Siew et al. the change in the optical parameters correlates with expansion of the layer below 400 °C upon H$-$Si dissociation followed by contraction above this temperature due to collapse of the net structure [116]. This behavior correlates well with relations that are known for glasses whose refractive index increases with density [117]. The refractive index increases up to 1.55 at 700 °C curing temperature which corresponds to typical values for silicon oxide. As a conclusion, the transformation can be considered as being complete after 1 h at 700 °C and results in a stable silicon oxide matrix.

5.6.2 Embedded Nanowires

After HSQ layers have been characterized germanium nanowires were embedded by spin coating. HSQ, also known as flowable oxide provides low viscosity and hence good gap-filling properties to ensure a complete embedding without creating voids inside the layer. Germanium nanowires grown onto Ge(111) substrates were coated at a rotational speed of 1500 rpm. The samples were analyzed by means of breaking edge SEM images showing the layer thickness and embedded structures which is presented in figure 5.30. The layer thickness after curing ranges from nearly 400 nm in the center region of the sample down to zero near the sample edges. Radial spreading of HSQ solution is hindered on structured surfaces which may cause the inhomogeneous thickness distribution. This effect can be reduced by higher rotational speeds during the spin coating process which in turn lowers the total thickness. Available higher viscous flowable oxides than FOx-14 would counterbalance the decrease of total thickness.

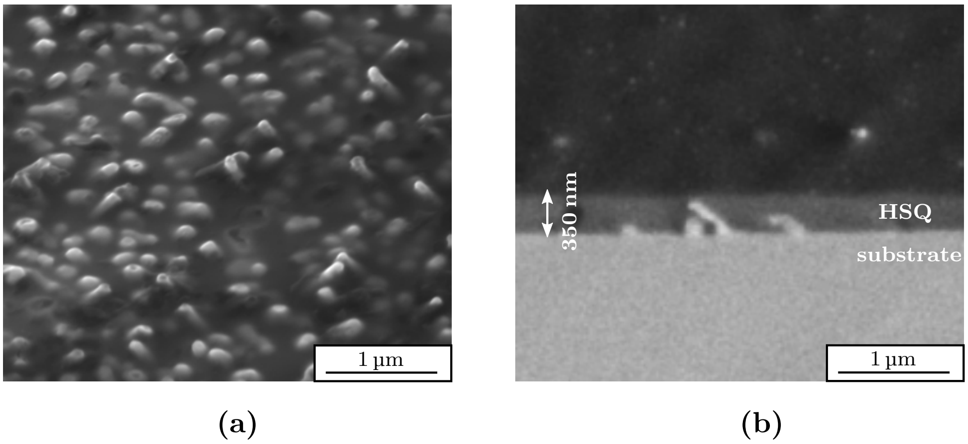

(a) **(b)**

Figure 5.30: Ge nanowires embedded in HSQ layer. (a) Region with thin HSQ layer near the sample edges. NW protrude the embedding matrix. (b) Cross sectional SEM image showing embedded NW on Ge(111) substrate.

In order to make coated structures available for electric measurements, e.g. by means of AFM, the top layer needs to be stripped off to get access to the nanowires. Detailed investigations have been done in the working group Si/Ge nanostructures at IKZ in which various techniques, i.e. wet-chemical, dry etching or polishing, have been tested to lay the nanowires open again.

6 Summary and Outlook

Many aspects of the growth of germanium nanowires by MBE have been elucidated. Thereby, all steps of the assembly process have been investigated beginning with substrate preparation, continuing with nanowire growth and finishing with catalyst removal and embedding of nanowires.

Nanowires have been grown successfully on (001), (011) and (111) oriented germanium substrates using gold droplets as metallic solvent (catalyst). The $\langle 011 \rangle$ growth directions turned out to be preferred irrespectively of the underlying substrate orientation which results in different inclinations of the nanowires according to the angles between $\langle 011 \rangle$ and the surface normal. As an example, germanium nanowires show a tilt of 35.3° between their axis and the substrate normal which is in contrast to silicon nanowires which typically grow perpendicular on Si(111) under similar growth conditions. Accordingly, different sidewall faceting was observed for germanium wires which exhibit basically four $\{111\}$ facets and two more or less distinct $\{001\}$ facets. Furthermore, the nanowire tip does not consist of a flat (011) facet but has a v-shape formed by another two $\{111\}$ facets. This has been confirmed by SEM images indicating the v-shaped geometry and TEM studies showing the tip angle between the two top facets.

The origin of inclined growth which is subject to current research has been investigated and discussed with respect to formation of structural defects at the nanowire base as well as the influence of thermodynamic quantities, namely supersaturation and surface energy. By means of TEM studies, the formation of crystal defects at the nanowire base could be ruled out to be responsible of the inclined growth. Moreover, as a first hypothesis high supersaturation should prevent the nanowire to change its growth direction even if other nanofacets may nucleate at the triple phase boundary of the droplet which is obviously needed to form a tip shape as it is observed for germanium nanowires. The second hypothesis regarding surface and edge energy of the nanowires states that a passivating effect of any surfactant, e.g. hydrogen, may influence to total surface energy of the wire such that different growth directions become probable.

The first hypothesis has been tested by increasing the deposition rate to enhance supersaturation inside the gold droplet. However, no effect has been observed. The second hypothesis can be verified by further experiments in which hydrogen is injected into the growth chamber. In general, surfactant mediated growth is known for several years in the field of planar growth but has not been discussed extensively with respect to nanowire growth. This could give further insight into thermodynamics during growth and moreover, it could provide a key to gain more homogenous and straight nanowire growth on the one hand and it could even lead to different, unexpected growth directions such as $\langle 001 \rangle$ which is of technological importance.

Processes which govern the growth of germanium nanowires have been elucidated. Thereby, surface diffusion plays an important role given the fact, that the observed nanowire length was up to eight times larger than the nominal thickness of deposited germanium. Obviously, material transport towards the droplets dominates the resulting growth rate.

It could be confirmed that the growth by MBE is rather limited by material transport than by the Gibbs-Thomson effect which would have an effect on the growth itself by changing the growth potential inside the droplet. Accordingly, surveying a large number of nanowires yielded a length-radius plot which shows an increase of the average nanowire length at decreasing radius which indicates a diffusion dominated growth regime.

As surface diffusivity is a function of temperature, the nanowire growth rate was investigated in the temperature range between 370 °C and 510 °C. As a result, the nanowire length is a function of substrate temperature and exhibits a maximum around 430 °C. This temperature dependency could be explained and modeled by considering various aspects of diffusive material transport. The fit also yielded the germanium surface diffusion length which amounts to 126 nm at 430 °C. Decreasing nanowire length at higher temperatures than 430 °C have been attributed to the increasing influence of desorption which lowers the resulting effective diffusion length.

Furthermore, germanium nanowires have been grown successfully on silicon substrates which is generally of technological significance. However, almost no nanowire growth was observed by adopting the growth process on silicon substrates directly. An additional oxidation step had to be applied after droplet formation in order to inhibit the surrounding substrate surface. Epitaxy in regions between the droplets could thus be effectively reduced.

There are indications that substrate preparation plays a crucial role on the growth results. Therefore, germanium substrates were investigated carefully in order to monitor any relation between preparation steps and the final growth result. It turned out that wet-chemical preparation leads to modifications of the surface morphology which was observed by means of AFM. While RMS roughness does not indicate any characteristic changes, the kurtosis value is lowered after preparation, indicating less peaks and valleys to be present but larger areas which are atomically flat. In other words, less atomic steps per unit area are observed at passivated substrates.

The surface modifications have impact on kinetics of impinging atoms that arrive at the surface during the deposition process. Such an effect can be observed after droplet formation already. Diffusivity is considered to be higher on pretreated surface due to larger regions which are atomically flat and thus exhibit no hinderance for diffusing atoms. Therefore, droplets on wet-chemically prepared substrates tend to be larger while a lower areal density has been observed.

Furthermore, the droplets itself show a certain mobility on pre-treated substrates which is indicated by small, tail-like trenches that were observed behind them by AFM. Obviously, those trenches result from material which is dissolved as the droplet grows further. In contrast, such structures are not observed on non-passivated substrates where droplets are likely to be pinned because more atomic steps per unit area are present. Different mobilities of gold droplets depending on the substrate preparation give a first hint to the origin of in-plane growing nanowires.

Wet-chemical substrate preparation has not only an impact on droplet formation but also on the final growth morphology. It was found that vertical nanowire growth can be effectively suppressed on carefully pretreated and passivated substrates. Instead, the gold droplets start crawling along the surface while a so-called in-plane nanowire forms behind them.

Similar to free-standing germanium nanowires, it was found that the preferential orientation of in-plane nanowires is $\langle 011 \rangle$ with distinct (111) faceting. This has been confirmed on (001), (011) and (111) oriented substrates. Moreover, differently oriented substrates exhibit a different number of equivalent $\langle 011 \rangle$ in-plane directions. As a special case, the Ge(011) surface has only two preferred, oppositional directions. Therefore, deviations from the preferred $\langle 011 \rangle$ direction namely along $\langle 001 \rangle$ can easily be observed. It was shown, that the fraction of in-plane nanowires which grow along $\langle 011 \rangle$ is highly dependent on the quality of wet-chemical passivation prior to growth. Thereby, hydride, chloride, bromide and sulfide passivation have been applied. The more stable the passivation layer is the higher the fraction of $\langle 011 \rangle$ growth becomes until the latter occurs exclusively on sulfide passivated substrates.

The presented studies demonstrate different growth directions dependent on the underlying surface. This is a first approach for guided growth along the substrate. Moreover, intentional kinking induced by artificial surface modifications could provide a cheap and effective way for structuring a surface or even to create cost effective devices on the base of such grown wires.

In addition to the growth and characterization of germanium nanowires, two technological issues have been targeted in the frame of this thesis. First, the presence of gold on the sample surface may cause problems for future applications like thermoelectrics or as anode material for lithium ion batteries. Therefore, a method was applied to remove gold selectively from the sample without damaging the grown structures. An aqueous solution of I_2, KI and HCl turned out to be an appropriate etchant to fulfill all requirements and finally, gold has been removed successfully.

The second issue mainly affects the possibility of contacting nanowires from the top for optoelectronic applications for instance. Therefore, the structures have to be embedded in an insulating matrix which should also be transparent for relevant wavelength depending to the respective, e.g. infrared (1.55 µm) for optical communications. This was achieved by spin-coating the sample with so-called flowable oxide (HSQ) which transforms into amorphous silicon oxide upon curing at temperatures up to 700 °C. Thereby, HSQ provides good gap-filling properties. By laying open the embedded structures with a CMP process, this could provide an effective method to contact nanowires from the top, e.g. also by means of an conducting AFM tip for research purposes.

Bibliography

1. R. P. Feynman, “There’s Plenty of Room at the Bottom”, *Engineering and Science* **23,** 22–36 (1960).
2. W. Goddard, *Handbook Of Nanoscience, Engineering, And Technology,* 2nd ed. (CRC Press, 2007).
3. H. Ibach and H. Lüth, *Solid-State Physics: An Introduction to Principles of Materials Science,* 4th ed. (Springer, 2009).
4. R. G. Treuting and S. M. Arnold, “Orientation habits of metal whiskers”, *Acta Metallurgica* **5,** 598 (1957).
5. R. S. Wagner and W. C. Ellis, “Vapor-Liquid-Solid mechanism of single crystal growth”, *Appl. Phys. Lett.* **4,** 89–90 (1964).
6. H. Sakaki, “Scattering Suppression and High-Mobility Effect of Size-Quantized Electrons in Ultrafine Semiconductor Wire Structures”, *Japanese Journal of Applied Physics* **19,** L735–L738 (1980).
7. L Samuelson *et al.,* “Semiconductor nanowires for 0D and 1D physics and applications”, English, *Physica E* **25,** 313–318 (2004).
8. Ioffe, *Semiconductors,* webpage `http://www.ioffe.rssi.ru/SVA/NSM/Semicond`, last visited: 19.12.2012.
9. IntelPR, *Intel Reinvents Transistors Using New 3-D Structure,* webpage `http://newsroom.intel.com/community/intel_newsroom/blog/2011/05/04/intel-reinvents-transistors-using-new-3-d-structure`, last visited: 18.12.2012.
10. C. Yan *et al.,* “Network-Enhanced Photoresponse Time of Ge Nanowire Photodetectors”, *ACS Applied Materials & Interfaces* **2,** 1794–1797 (2010).
11. A. Bulusu and D. G. Walker, “Quantum modeling of thermoelectric performance of strained Si/Ge/Si superlattices using the nonequilibrium Green’s function method”, *J. Appl. Phys.* **102,** 073713 (2007).
12. A. I. Boukai *et al.,* “Silicon nanowires as efficient thermoelectric materials”, *Nature* **451,** 168–171 (Jan. 2008).
13. C. K. Chan *et al.,* “High-performance lithium battery anodes using silicon nanowires”, *Nat. Nanotechnol.* **3,** 31–35 (Jan. 2008).
14. C. K. Chan, X. F. Zhang, and Y. Cui, “High Capacity Li Ion Battery Anodes Using Ge Nanowires”, *Nano Lett.* **8,** PMID: 18095738, 307–309 (2008).

15. A. M. Chockla *et al.,* "Solution-Grown Germanium Nanowire Anodes for Lithium-Ion Batteries", *ACS Appl. Mater. Interfaces* **4,** 4658–4664 (2012).
16. L. Schubert *et al.,* "Silicon nanowhiskers grown on ⟨111⟩Si substrates by molecular-beam epitaxy", *Appl. Phys. Lett.* **84,** 4968–4970 (2004).
17. Y. Huang *et al.,* "Gallium Nitride Nanowire Nanodevices", *Nano Lett.* **2,** 101–104 (2002).
18. M. Aagesen *et al.,* "Molecular beam epitaxy growth of free-standing plane-parallel InAs nanoplates", *Nat. Nanotechnol.* **2,** 761–764 (Dec. 2007).
19. Y. Wang *et al.,* "Epitaxial growth of silicon nanowires using an aluminium catalyst", *Nat Nano* **1,** 186–189 (Dec. 2006).
20. C.-Y. Wen *et al.,* "Formation of Compositionally Abrupt Axial Heterojunctions in Silicon-Germanium Nanowires", *Science* **326,** 1247–1250 (2009).
21. C.-Y. Wen *et al.,* "Structure, Growth Kinetics, and Ledge Flow during Vapor-Solid-Solid Growth of Copper-Catalyzed Silicon Nanowires", *Nano Lett.* **10,** 514–519 (2010).
22. J. V. Wittemann *et al.,* "Silver catalyzed ultrathin silicon nanowires grown by low-temperature chemical-vapor-deposition", *J. Appl. Phys.* **107,** 096105 (2010).
23. F. M. Ross, "Controlling nanowire structures through real time growth studies", *Rep. Prog. Phys.* **73** (2010).
24. N. Li, T. Y. Tan, and U. Gösele, "Transition region width of nanowire hetero- and pn-junctions grown using vapor-liquid-solid processes", *Applied Physics A: Materials Science & Processing* **90,** 591–596 (4 2008).
25. C. Colombo *et al.,* "Ga-assisted catalyst-free growth mechanism of GaAs nanowires by molecular beam epitaxy", *Phys. Rev. B* **77,** 155326 (2008).
26. B. Mandl *et al.,* "Growth Mechanism of Self-Catalyzed Group III-V Nanowires", *Nano Lett.* **10,** 4443–4449 (2010).
27. L. Gao *et al.,* "Self-Catalyzed Epitaxial Growth of Vertical Indium Phosphide Nanowires on Silicon", *Nano Lett.* **9,** 2223–2228 (2009).
28. E. Dimakis *et al.,* "Self-Assisted Nucleation and Vapor-Solid Growth of InAs Nanowires on Bare Si(111)", *Crystal Growth & Design* **11,** 4001–4008 (2011).
29. D. Rudolph *et al.,* "Direct Observation of a Noncatalytic Growth Regime for GaAs Nanowires", *Nano Lett.* **11,** 3848–3854 (2011).
30. P. Atkins and J. De Paula, *Physical Chemistry,* 8th ed. (W.H. Freeman, 2006).
31. B. Lewis and J. Anderson, *Nucleation and growth of thin films* (Academic Press, 1978).
32. E. A. Moelwyn-Hughes, *Physical Chemistry,* 2nd ed. (Pergamon Press, 1964), 1334.

33. Y. Eichhammer, M. Heyns, and N. Moelans, “Calculation of phase equilibria for an alloy nanoparticle in contact with a solid nanowire”, *Calphad* **35,** 173 –182 (2011).
34. Q. Jiang *et al.,* “Thermal stability of crystalline thin films”, *Thin Solid Films* **312,** 357 –361 (1998).
35. G. Kaptay, “The Gibbs Equation versus the Kelvin and the Gibbs-Thomson Equations to Describe Nucleation and Equilibrium of Nano-Materials”, *J. Nanosci. Nanotechnol.* **12,** 2625–2633 (2012).
36. A. P. Chernyshev, “Melting of solid nanoscale films with free surfaces”, *Phys. Scr.* **85,** 045601 (2012).
37. J. W. Gibbs, “On the Equilibrium of Heterogeneous Substances”, *Trans. Conn. Acad. Arts Sci.* **3,** 108–248 (1875).
38. Q. Jiang and H. Lu, “Size dependent interface energy and its applications”, *Surf. Sci. Rep.* **63,** 427 –464 (2008).
39. D. Kashchiev, *Nucleation: Basic Theory With Applications* (Butterworth Heinemann, 2000).
40. I. Markov, *Crystal Growth for Beginners: Fundamentals of Nucleation, Crystal Growth and Epitaxy* (World Scientific, 2003).
41. W. Ostwald, “Über die vermeintliche Isomerie des roten und gelben Quecksilberoxyds und die Oberflächenspannung fester Körper”, *Z. Phys. Chem.* **34,** 495 –503 (1900).
42. I. M. Lifshitz and V. Slyozov, “The kinetics of precipitation from supersaturated solid solutions”, *J. Phys. Chem. Solids* **19,** 35–50 (1961).
43. K. Oura *et al., Surface Science,* 1st ed. (Springer, 2003).
44. J. Matthews and A. Blakeslee, “Defects in epitaxial multilayers: I. Misfit dislocations”, *J. Cryst. Growth* **27,** 118 –125 (1974).
45. M. Hanke *et al.,* “SiGe/Si(001) Stranski-Krastanow islands by liquid-phase epitaxy: Diffuse x-ray scattering versus growth observations”, *Phys. Rev. B* **69,** 075317 (7 2004).
46. G. Ehrlich and F. G. Hudda, “Atomic View of Surface Self-Diffusion: Tungsten on Tungsten”, *The Journal of Chemical Physics* **44,** 1039–1049 (1966).
47. R. L. Schwoebel and E. J. Shipsey, “Step Motion on Crystal Surfaces”, *J. Appl. Phys.* **37,** 3682–3686 (1966).
48. R. L. Schwoebel, “A Diffusion Model for Filamentary Crystal Growth”, *J. Appl. Phys.* **38,** 1759–1765 (1967).
49. E. Givargizov, “Fundamental aspects of VLS growth”, *J. Cryst. Growth* **31,** 20 –30 (1975).

50. S. A. Dayeh and S. T. Picraux, “Direct Observation of Nanoscale Size Effects in Ge Semiconductor Nanowire Growth”, *Nano Lett.* **10,** 4032–4039 (2010).
51. J. Johansson *et al.,* “Mass Transport Model for Semiconductor Nanowire Growth”, *J. Phys. Chem. B* **109,** 13567–13571 (July 2005).
52. N. Zakharov *et al.,* “Growth of Si whiskers by MBE: Mechanism and peculiarities”, *Physica E: Low-dimensional Systems and Nanostructures* **37,** Proceedings of the E-MRS 2006 Symposium E: Science and Technology of Nanotubes and Nanowires, 148 –152 (2007).
53. V. Schmidt *et al.,* “Silicon Nanowires: A Review on Aspects of their Growth and their Electrical Properties”, *Advanced Materials* **21,** 2681–2702 (2009).
54. A. Kramer, *Growth and characterization of silicon and germanium nanowhiskers,* PhD thesis (HU Berlin, 2009).
55. C. Soci *et al.,* “A Systematic Study on the Growth of GaAs Nanowires by Metal-Organic Chemical Vapor Deposition”, *Nano Lett.* **8,** PMID: 18956910, 4275–4282 (2008).
56. V. Dubrovskii and N. Sibirev, “General form of the dependences of nanowire growth rate on the nanowire radius”, *J. Cryst. Growth* **304,** 504 –513 (2007).
57. H. Ibach, *Physics of Surfaces And Interfaces* (Springer, 2006).
58. V. G. Dubrovskii *et al.,* “Gibbs-Thomson and diffusion-induced contributions to the growth rate of Si, InP, and GaAs nanowires”, *Phys. Rev. B: Condens. Matter Mater. Phys.* **79,** 205316 (2009).
59. D. Mattox, *Handbook of Physical Vapor Deposition (PVD) Processing: Film Formation, Adhesion, Surface Preparation and Contamination Control* (Noyes Publications, 1998).
60. (ed D. R. Lide) *Handbook of Chemistry and Physics,* 90th ed. (CRC Press, 2009).
61. G. Sauerbrey, “Verwendung von Schwingquarzen zur Wägung dünner Schichten und zur Mikrowägung”, *Zeitschrift für Physik A Hadrons and Nuclei* **155,** 10.1007/BF01337937, 206–222 (2 1959).
62. C.-S. Lu and O. Lewis, “Investigation of film-thickness determination by oscillating quartz resonators with large mass load”, *J. Appl. Phys.* **43,** 4385–4390 (1972).
63. A. Ichimiya and P. Cohen, *Reflection High-Energy Electron Diffraction* (Cambridge University Press, 2004).
64. C. Cheze *et al.,* “In situ investigation of self-induced GaN nanowire nucleation on Si”, *Appl. Phys. Lett.* **97,** 043101 (2010).
65. M Tchernycheva *et al.,* “Temperature conditions for GaAs nanowire formation by Au-assisted molecular beam epitaxy”, *Nanotechnology* **17,** 4025 (2006).
66. J. Czochralski, “Ein neues Verfahren zur Messung der Kristallisationsgeschwindigheit der Metalle”, *Z. Phys. Chem.* **92,** 219–221 (1918).

67. G. Petzow, *Metallographisches, keramographisches und plastographisches Ätzen,* 6th ed. (Gebrüder Borntraeger, 1994).
68. W. Kern, *Handbook of Silicon Wafer Cleaning Technology* (eds K. A. Reinhardt and W. Kern) 2nd ed. (William Andrew, 2008), 24–26.
69. D. Knapp, *Chemistry and electronics of the Ge(111) surface,* PhD thesis (California Institute of Technology, 2011).
70. M. Fouchier, M. T. McEllistrem, and J. J. Boland, "Novel adatom-terminated step structure on the Ge(111)-(1×1):Br surface", *Surf. Sci.* **385,** l905 –l910 (1997).
71. J. Kim, *Germanium Surface Preparation Methods* (VDM Verlag, 2008), 104 Seiten.
72. S. Sun *et al.,* "Surface termination and roughness of Ge(100) cleaned by HF and HCl solutions", *Appl. Phys. Lett.* **88,** 021903 (2006).
73. T. Akane *et al.,* "Preparation of high-quality Ge substrate for MBE", *Appl. Surf. Sci.* **108,** 303 –305 (1997).
74. H. Okumura, T. Akane, and S. Matsumoto, "Carbon contamination free Ge(100) surface cleaning for MBE", *Appl. Surf. Sci.* **125,** 125 –128 (1998).
75. J. Y. Kim *et al.,* "Passivation Studies of Germanium Surfaces", *Solid State Phenomena* **134,** 33–36 (2008).
76. R. Kaltofen and J. Ziemann, *Tabellenbuch Chemie,* 13th ed. (Harri Deutsch, 1998).
77. G. W. Anderson *et al.,* "The S-passivation of Ge(100)-(1 x 1)", *Appl. Phys. Lett.* **66,** 1123–1125 (1995).
78. A. Grigorescu *et al.,* "10 nm lines and spaces written in HSQ, using electron beam lithography", *Microelectron. Eng.* **84,** Proceedings of the 32nd International Conference on Micro- and Nano-Engineering, 822 –824 (2007).
79. J. Penaud, F. Fruleux, and E. Dubois, "Transformation of hydrogen silsesquioxane properties with RIE plasma treatment for advanced multiple-gate MOSFETs", *Appl. Surf. Sci.* **253,** 395 –399 (2006).
80. M. Born, E. Wolf, and A. Bhatia, *Principles of Optics: Electromagnetic Theory of Propagation, Interference and Diffraction of Light* (Cambridge University Press, 1999).
81. L. Reimer, *Scanning Electron Microscopy: Physics of Image Formation and Microanalysis* (ed P. W. Hawkes) 2nd ed. (Springer, 1998).
82. T. E. Everhart and R. F. M. Thornley, "Wide-band detector for micro-microampere low-energy electron currents", *Journal of Scientific Instruments* **37,** 246 (1960).
83. E. Abbe, "Beiträge zur Theorie des Mikroskops und der mikroskopischen Wahrnehmung", *Archiv für mikroskopische Anatomie* **9,** 413–468 (1873).
84. L. Reimer and H. Kohl, *Transmission Electron Microscopy* (ed W. T. Rhodes) 5th ed. (Springer, 2008).

85. G. Binnig, C. F. Quate, and C. Gerber, "Atomic Force Microscope", *Phys. Rev. Lett.* **56,** 930–933 (1986).
86. P. Eaton and P. West, *Atomic Force Microscopy* (Oxford University Press, 2010).
87. M. Raposo, Q. Ferreira, and P. Ribeiro, "A Guide for Atomic Force Microscopy Analysis of SoftCondensed Matter", in: *Modern Research and Educational Topics in Microscopy* (eds A. Méndez-Vilas and J. Díaz) (Formatex Research Center, 2007).
88. H. Fujiwara, *Spectroscopic Ellipsometry: Principles and Applications* (John Wiley & Sons, 2007).
89. D. Attwood, *Soft X-Rays And Extreme Ultraviolet Radiation: Principles And Applications* (Cambridge University Press, 2007).
90. A. C. Thompson *et al., X-ray Data Booklet* (ed A. C. Thompson) 3rd ed. (Lawrence Berkeley National Laboratory, University of California, 2009).
91. J.-M. Zhang *et al.,* "Anisotropy analysis of the surface energy of diamond cubic crystals", *Surf. Interface Anal.* **35,** 805–809 (2003).
92. R. J. Jaccodine, "Surface Energy of Germanium and Silicon", *J. Electrochem. Soc.* **110,** 524–527 (1963).
93. P. Artoni *et al.,* "Kinetics of Si and Ge nanowires growth through electron beam evaporation", *Nanoscale Research Letters* **6,** 162 (2011).
94. M. Kolíbal *et al.,* "Controlled faceting in ⟨110⟩ germanium nanowire growth by switching between vapor-liquid-solid and vapor-solid-solid growth", *Appl. Phys. Lett.* **100,** 203102 (2012).
95. K. W. Schwarz and J. Tersoff, "Elementary Processes in Nanowire Growth", *Nano Lett.* **11,** 316–320 (2011).
96. F. M. Ross, J. Tersoff, and M. C. Reuter, "Sawtooth Faceting in Silicon Nanowires", *Phys. Rev. Lett.* **95,** 146104 (2005).
97. T. Hanrath and B. A. Korgel, "Crystallography and Surface Faceting of Germanium Nanowires", *Small* **1,** 717–721 (2005).
98. P. Madras, E. Dailey, and J. Drucker, "Kinetically Induced Kinking of Vapor-Liquid-Solid Grown Epitaxial Si Nanowires", *Nano Lett.* **9,** 3826–3830 (2009).
99. B. Tian *et al.,* "Single-crystalline kinked semiconductor nanowire superstructures", *Nat. Nanotechnol.* **4,** 824–829 (Dec. 2009).
100. Y. Cui *et al.,* "Diameter-controlled synthesis of single-crystal silicon nanowires", *Appl. Phys. Lett.* **78,** 2214–2216 (2001).
101. V. Schmidt, S. Senz, and U. Gösele, "Diameter-Dependent Growth Direction of Epitaxial Silicon Nanowires", *Nano Lett.* **5,** 931–935 (2005).
102. A. Kramer *et al.,* "Self-assembled and ordered growth of silicon and germanium nanowires", *Superlattices Microstruct.* **46,** <ce:title>NanoSEA2008</ce:title>, 277 –285 (2009).

103. A. D. Gamalski, C. Ducati, and S. Hofmann, "Cyclic Supersaturation and Triple Phase Boundary Dynamics in Germanium Nanowire Growth", *The Journal of Physical Chemistry C* **115,** 4413–4417 (2011).

104. M. I. d. Hertog *et al.,* "Gold Catalyzed Silicon Nanowires: Defects in the Wires and Gold on the Wires", in: *Microscopy of Semiconducting Materials 2007* (eds A. G. Cullis and P. A. Midgley) **120** (Springer Netherlands, 2008), 217–220.

105. S. Kodambaka *et al.,* "Germanium Nanowire Growth Below the Eutectic Temperature", *Science* **316,** 729–732 (2007).

106. P. Nguyen, H. Ng, and M. Meyyappan, "Growth of Individual Vertical Germanium Nanowires", *Advanced Materials* **17,** 549–553 (2005).

107. E. F. Pecora *et al.,* "Heteroepitaxial Growth and Faceting of Ge Nanowires on Si(111) by Electron-Beam Evaporation", *Electrochem. Solid-State Lett.* **13,** K53–K55 (2010).

108. H. J. Kim *et al.,* "A technique for the measurement of surface diffusion coefficient and activation energy of Ge adatom on Si(001)", *J. Appl. Phys.* **95,** 6065–6071 (2004).

109. D. Leonhardt and S. M. Han, "Energetics of Ge nucleation on SiO2 and implications for selective epitaxial growth", *Surf. Sci.* **603,** 2624 –2629 (2009).

110. A. F. i Morral *et al.,* "Nucleation mechanism of gallium-assisted molecular beam epitaxy growth of gallium arsenide nanowires", *Appl. Phys. Lett.* **92,** 063112 (2008).

111. R. Bansen, *Growth and Characterization of Germanium Nanowires,* MA thesis (Humboldt University of Berlin, 2011).

112. L. Yu and P. Roca i Cabarrocas, "Initial nucleation and growth of in-plane solid-liquid-solid silicon nanowires catalyzed by indium", *Phys. Rev. B* **80,** 085313 (8 2009).

113. D. Tsivion *et al.,* "Guided Growth of Millimeter-Long Horizontal Nanowires with Controlled Orientations", *Science* **333,** 1003–1007 (2011).

114. R. Heimburger *et al.,* "Polycrystalline silicon films on glass grown by amorphous-liquid-crystalline transition at temperatures below 330°C", *Thin Solid Films* **520,** 1784 –1788 (2012).

115. J. B. Ratchford *et al.,* "Gold Removal from Germanium Nanowires", *Langmuir* **25,** 9473–9479 (Aug. 2009).

116. Y. K. Siew *et al.,* "Thermal Curing of Hydrogen Silsesquioxane", *J. Electrochem. Soc.* **147,** 335–339 (2000).

117. T. Seward and T. Vascott, *High temperature glass melt property database for process modeling* (American Ceramic Society, 2005).

List of Figures

List of Tables

List of Abbreviations

AFM	atomic force microscopy
BSE	backscattered electrons
CMP	chemical-mechanical polishing
DIW	deionized water
EBE	electron beam evaporation
EBSD	electron backscattered diffraction
EDX	energy-dispersive X-ray spectroscopy
FFT	fast Fourier transform
FIB	focused ion beam
FTIR	Fourier transform infrared spectroscopy
HRTEM	high-resolution transmission electron microscopy
HSQ	hydrogen silsesquioxane
MBE	molecular beam epitaxy
MOVPE	metal organic vapor phase epitaxy
NW	nanowire
QCM	quartz crystal microballance
RCA SC-1	RCA standard clean 1
RGA	residual gas analyzer
RHEED	reflection high energy electron diffraction
SE	secondary electrons
SEM	scanning electron microscopy

SLD	superluminescent diode
STEM	scanning transmission electron microscopy
STM	scanning tunneling microscope
TEM	transmission electron microscopy
UHV	ultra-high vacuum
VLS	vapor-liquid-solid
VSS	vapor-solid-solid
w.l.o.g.	without loss of generality
WDS	wavelength dispersive X-ray spectroscopy
XRR	X-ray reflectometry

List of symbols

c	speed of light	$2.998 \times 10^{8}\,\mathrm{m\,s^{-1}}$
e	elementary charge	$1.602 \times 10^{-19}\,\mathrm{C}$
η	kinematic viscosity	$1\,\mathrm{cSt} = 1 \times 10^{-6}\,\mathrm{m^{2}\,s^{-1}}$
h	Planck constant	$6.626 \times 10^{-34}\,\mathrm{J\,s}$
H_i	i-th order modified Bessel function of the first kind	
J_{sw}	adatom flux from substrate to nanowire	
K_i	i-th order modified Bessel function of the second kind	
λ_e	de Broglie wavelength of electrons	
λ_s	diffusion length of atoms on a substrate	
λ_w	diffusion length of atoms on nanowire sidewalls	
m_0	mass of an electron	$9.109 \times 10^{-31}\,\mathrm{kg}$
N_A	Avogardo constant	$6.022 \times 10^{23}\,\mathrm{mol^{-1}}$
ϱ_{Ge}	mass density of germanium	$5323\,\mathrm{kg\,m^{-3}}$
σ	specific surface energy	$1\,\mathrm{J\,m^{-2}}$
$\mathcal{V}_{Ge}$	molar volume of germanium	$13.63 \times 10^{-6}\,\mathrm{m^{3}\,mol^{-1}}$

Acknowledgements

The preparation and completion of this work would not have been possible without the guidance and support from a number of people to whom I would to express my gratitude.

First, I would like to thank Professor Roberto Fornari for giving me the opportunity to work in the fascinating and challenging field of nanostructures and nanocrystals.

I am very grateful to my colleagues from the working group Si/Ge Nanocrystals for their practical and theoretical advise but also for contributing to a pleasant and amicable working atmosphere. I would like to express my deep appreciation and gratitude to my advisor, Dr. Torsten Boeck, who believed in me all the way from the decision to begin to work in IKZ to the completion of this thesis. His communicative and at the same time encouraging and motivating nature has been a big help to cope all challenges with the needed verve and engagement while giving me the opportunity to work freely and to pursue own approaches. I am truly indebted and thankful to Peter Schramm who patiently introduced me to all the vacuum and deposition equipment and who was always willing to share his inexhaustible know-how. I am also very grateful to Dr. Thomas Teubner and Dr. Robert Heimburger for proof reading this thesis as well as for many fruitful discussions and lots of thought-provoking suggestions. A special thanks goes to my colleague and friend Roman Bansen for great teamwork and experimental assistance but also for his open minded nature which always enriched not only scientific discussions and conversations and gave lots of food for thought. My further gratitude goes to Franziska Schütte for experimental assistance especially in conducting spin coating experiments and their evaluation.

I am much obliged to many colleagues at IKZ who supported me especially in the characterization of many samples. First, I would like to thank Dr. Martin Albrecht for kindly introducing me to SEM, together with Toni Markurt und Tilo Remmele for TEM investigations. My further gratitude goes to Martin Naumann for his assistance in TEM sample preparation by means of focussed ion beams. My further gratitude goes to Dr. Martin Schmidbauer for X-ray reflectivity measurements which was essential for deposition rate calibration.

I also want to express my sincere thankfulness to Dr. Nikolai Abrosimov who has grown the germanium crystals and to Dr. Uta Juda her colleagues from the crystal machining group who have cut the crystals and polished the substrates. It was invaluable help to gain substrates directly from them.

Finally, I would be remiss if I didn't acknowledge the thoughtful and affectionate support from my girlfriend and partner, Franziska, who often shouldered more than the fair share of the parenting and household burdens while I pursued this final degree.

Publications

Articles

1. J. Schmidtbauer, R. Bansen, R. Heimburger, T. Teubner, T. Boeck, R. Fornari: *Germanium nanowire growth controlled by surface diffusion effects*, Applied Physics Letters 101, 043105, 2012

2. V. Aroutiounian, K. Gambaryan, V. Harutyunyan, P. Soukiassian, T. Boeck, J. Schmidtbauer, R. Bansen: *The Ostwald ripening at nanoengineering of InAsSbP spherical and ellipsoidal quantum dots on InAs(100) surface*, Journal of Contemporary Physics 48, 37-42, 2013

3. R. Heimburger, R. Bansen, T. Markurt, J. Schmidtbauer, T. Teubner, T. Boeck: *Solvent-induced growth of crystalline silicon on glass*, Photovoltaic Specialists Conference (PVSC), 2012 38th IEEE, 000333 - 000337, 2012

4. J. Schmidtbauer, R. Bansen, T. Teubner, T. Boeck: *Growth of germanium nanowires along* ⟨110⟩, 6th Nanowire Growth Workshop, St Petersburg, June 4–6, 2012

5. R. Bansen, J. Schmidtbauer, R. Gurke, T. Teubner, R. Heimburger, T. Boeck: *Ge in-plane nanowires grown by MBE: influence of surface treatment*, submitted to CrystEngCom

Patents

6. R. Fornari, T. Boeck, P. Schramm, R. Heimburger, J. Schmidtbauer, G. Schadow, T. Teubner: *Kristallisationsverfahren zur Erzeugung kristalliner Halbleiterschichten.* Application filed in, file number: DE 10 2012 044 014.0